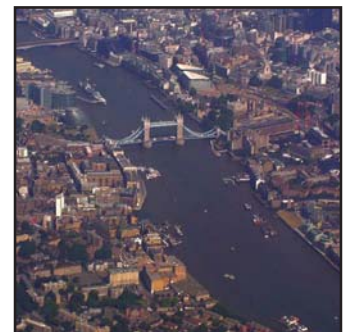# Building Inventory Compilation for Disaster Management: Application of Remote Sensing and Statistical Modeling

by

Pooya Sarabandi, Anne S. Kiremidjian, Ronald T. Eguchi and Beverley J. Adams

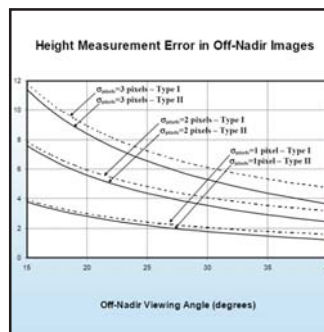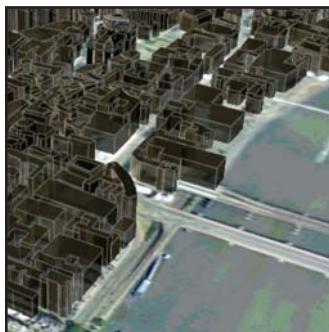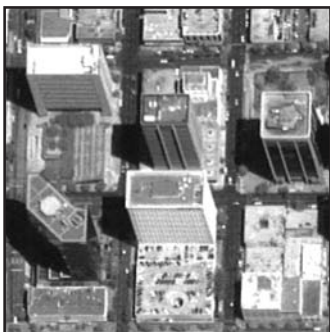Technical Report MCEER-08-0025

November 20, 2008

NOTICE

Building Inventory Compilation for Disaster Management: Application of Remote Sensing and Statistical Modeling

by

Pooya Sarabandi,[1] Anne S. Kiremidjian,[2] Ronald T. Eguchi[3] and Beverley J. Adams[4]

Publication Date: November 20, 2008
Submittal Date: August 26, 2008

Technical Report MCEER-08-0025

Task Number 10.3.1

NSF Master Contract Number EEC 9701471

1   Consulting Assistant Professor, Department of Civil and Environmental Engineering, Stanford University
2   Professor, Department of Civil and Environmental Engineering, Stanford University
3   President/CEO, ImageCat, Inc.
4   Managing Director, ImageCat, Ltd.

Preface

The Multidisciplinary Center for Earthquake Engineering Research (MCEER) is a national center of excellence in advanced technology applications that is dedicated to the reduction of earthquake losses nationwide. Headquartered at the University at Buffalo, State University of New York, the Center was originally established by the National Science Foundation in 1986, as the National Center for Earthquake Engineering Research (NCEER).

Comprising a consortium of researchers from numerous disciplines and institutions throughout the United States, the Center's mission is to reduce earthquake losses through research and the application of advanced technologies that improve engineering, pre-earthquake planning and post-earthquake recovery strategies. Toward this end, the Center coordinates a nationwide program of multidisciplinary team research, education and outreach activities.

MCEER's research is conducted under the sponsorship of two major federal agencies: the National Science Foundation (NSF) and the Federal Highway Administration (FHWA), and the State of New York. Significant support is derived from the Federal Emergency Management Agency (FEMA), other state governments, academic institutions, foreign governments and private industry.

MCEER's NSF-sponsored research objectives are twofold: to increase resilience by developing seismic evaluation and rehabilitation strategies for the post-disaster facilities and systems (hospitals, electrical and water lifelines, and bridges and highways) that society expects to be operational following an earthquake; and to further enhance resilience by developing improved emergency management capabilities to ensure an effective response and recovery following the earthquake (see the figure below).
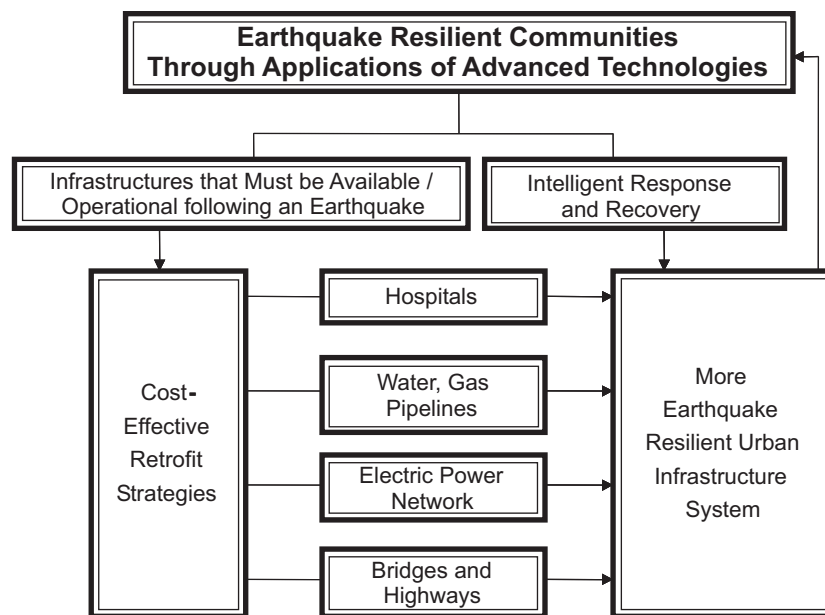
A cross-program activity focuses on the establishment of an effective experimental and analytical network to facilitate the exchange of information between researchers located in various institutions across the country. These are complemented by, and integrated with, other MCEER activities in education, outreach, technology transfer, and industry partnerships.

This report introduces a methodology to extract spatial, geometric and engineering attributes of buildings using single high-resolution satellite images. Rational Polynomial Coefficients (RPC) are used to generate three dimensional models of buildings showing height, footprint, and shape information. Geometric information defining the sensor's orientation is used in conjunction with the RPC projection model to generate digital elevation models. The report describes how the location and height of a structure are extracted by measuring the image coordinates for the corner of a building at ground level and its corresponding roof-point coordinates, and using the relationship between image-space and object-space together with the sensor's orientation. The implementation of the algorithm and its application to the City of London are described. In addition, a methodology based on a multinomial logistic model is developed to infer the marginal probability distributions of the structural type and occupancy of a building. The input parameters for the statistical model are derived from the three dimensional models reconstructed from the satellite imagery. Datasets collected for southern California are used to train the models and establish inference rules to predict the engineering parameters of the buildings in the region. The predictive capability of the model is shown through the computation of the marginal probability distribution for a sample building.

ABSTRACT

This report introduces a methodology for rapidly developing information on the physical properties of a building using single high-resolution satellite images. Using rational polynomial coefficients (RPCs) as a replacement for the sensor's camera model, we are able to create 3-D models of a building showing height, foot print and shape information for most structures. Geometric information defining the sensor's orientation is used in conjunction with the RPC projection model to generate an accurate digital elevation model (DEM). The report describes how the location (longitude and latitude) and height of individual structures are extracted by measuring the image coordinates for the corner of a building at ground level and its corresponding roof-point coordinates, and using the relationship between image-space and object-space together with the sensor's orientation. The report describes the implementation of this algorithm in a software package called MIHEA (Mono-Image Height Extraction Algorithm) and presents an example for the City of London.

In addition, the report also presents a methodology for inferring several key engineering attributes of a building, i.e., structural type and occupancy. A multinomial logistic model is utilized in this study in order to compute the marginal probability distribution of different class memberships. The model incorporates and supports categorical as well as quantitative data. The explanatory variables used as the input parameters to the statistical model, are selected such that they can directly be derived from the 3-D models reconstructed from the satellite imagery. Two datasets collected for southern California, are used to train the models and establish inference rules in order to predict the regional engineering parameters of buildings in the region. The classification error and prediction power of the model are then presented in the report and an example of the marginal probability distribution computed for a sample building is shown.

ACKNOWLEDGMENTS

TABLE OF CONTENTS

LIST OF ILLUSTRATIONS

LIST OF TABLES

SECTION 1
INTRODUCTION

This report represents work completed under MCEER's task on quantifying human threats on the urban environment. The focus is on developing building inventory models using remotely-sensed data. More specifically, the research discussed here is directed at the creation of three-dimensional (3-D) models of individual buildings, and ultimately of major urban areas. By developing information on the physical characteristics of buildings, analysts are able to 1) quantify the size of structures, both from a height standpoint, as well as from a footprint perspective; 2) associate particular structural or construction systems with building heights; and 3) roughly estimate the vulnerability of the structure to a variety of hazards, including human threats. In large part, this research is based on work completed by Dr. Pooya Sarabandi of Stanford University, who was supported in part by a task funded by ImageCat under this subcontract. This report is an abstraction of work originally presented by Dr. Sarabandi in his Ph.D dissertation which is entitled *"Development of Algorithms for Building Inventory Compilation through Remote Sensing and Statistical Inferencing."*

There has been a considerable body of literature that has been published regarding the generation of 3-D building and city models using remotely-sensed data. Interest has been fuelled by the capability of airborne and satellite imagery to yield low-cost information concerning the built environment, for diverse applications (see Madhavan *et al.*, 2002) including: 3-D visualization; planning; architectural design; monitoring urban growth; environmental impact assessment; and telecommunications positioning. In addition to these well established uses, the construction of building inventories from high-resolution imagery is also of interest for disaster management. In particular, building inventories are especially important for post-disaster loss estimation studies. Surprisingly, however, this latter application area has received comparatively little attention, with isolated references e.g., Miura and Midorikawa (2003).

The extraction of building information is essentially a two-stage process. A fundamental distinction is made by Suveg and Vosselman (2000, 2001) and Rotensteiner and Briese (2002) between:

1

1) The initial detection and characterization of buildings on remote sensing coverage; and

2) The reconstruction of buildings as a 3-D model.

Distinguishing between these two phases reflects an increase in detail from a comparatively crude identification of building 'hypotheses' during the former, to the realistic representation of buildings (in terms of both geometry and appearance) during the latter. For loss estimation purposes, the emphasis is on achieving an acceptable geometric representation of the building stock, in terms of building height and footprint area, so that building values (in terms of building size and construction materials), and structural vulnerabilities can be assessed. As such, procedures involved in the former methodological phase are of greater interest than superfluous details concerning architectural design, roof construction and possibly façades (Lee *et al.*, 2002).

Previous studies have employed a wide range of data sources for building detection and characterization (Brenner, 1999). Information has been successfully derived from high-resolution optical, Light Detection and Ranging (LIDAR) and Synthetic Aperture Radar (SAR) remote sensing devices, together with ground plans and 'other' unspecified sources. In order to put the work presented here into some perspective, the next chapter discusses some of these sensors and how they are employed in either detecting and extracting buildings from a larger footprint (e.g., a city) and how they are used to generate important physical data on individual buildings. In Chapter 3, the fundamentals of 3-D modeling are presented. The notion of single satellite or mono-image processing is presented as a key factor in distinguishing the approach presented here with those that are documented in Chapter 2. In Chapter 4, the concept of stereo and single-image 3-D building reconstruction is presented. However, examples of 3-D reconstruction are provided only for single images. Finally, Chapter 5 discusses how physical information on building height, size and shape can be used to infer different structural types and vulnerabilities.

SECTION 2
METHODOLOGICAL REVIEW

From a comprehensive review of the photogrammetric, remote sensing and machine vision literature, a range of data sources have been employed for building extraction. The use of optical monocular and stereoscopic imagery is most widely documented. Details of the various methodological procedures are given in Section 2.1. The emergence of laser altimetry or LIDAR data in the late 1990s presented an alternative source of high-resolution height data. Section 2.2 describes the various processing sequences for building extraction. The potential of synthetic aperture radar (SAR) technology has only recently been recognized in the literature. Section 2.3 presents a limited number of exploratory studies investigating the capability of intensity and IfSAR (interferometric SAR) data to quantify building height and footprint.

In many instances, the above datasets are utilized in conjunction with other independent sources. Sections 2.1 through 2.3, therefore, include a brief summary of ways in which other data sources are integrated to derive heights and footprints. Section 2.4 evaluates the spatial scales at which 3-D building delineation is undertaken, while Section 2.5 summarizes the merits and limitations of each dataset. These discussions provide background material for the approach that is introduced in this report for creating 3-D models of buildings using single, off-nadir satellite images.

2.1   Optical Imagery

According to Bruun *et al*. (1998) and Gamba and Houshmand (2000), optical imagery remains the most widely-documented data source for urban modeling. Frames of aerial photography or high-resolution satellite imagery are used individually, and in combination, to generate useful information on urban environments, i.e., buildings and other infrastructure.

To map buildings from a single 'monocular' image (Huertas *et al*., 1993; Quint, 1997), an orthophotograph is usually employed, in which planimetric distortion has been removed (Stassopoulou and Caelli, 2000). The use of oblique imagery is less widely documented, since off-nadir viewing presents additional analytical difficulties (see Lin and Nevatia, 1995). 'Cues' or 'primitives' defining building geometry, such as lines, polygons, corners and shadows, are then identified using techniques, including manual inspection (Stassopoulou and Caelli, 2000),

Fourier transformation (Sohn and Dowman, 2001), feature extraction (Kim and Choi, 1995; Lin and Nevatia, 1998; Noronha and Nevatia, 1998, 2001; Xu and Li, 1998; Miura and Midorikawa, 2003), and segmentation (Jaynes *et al*., 1997; Stassopoulou and Caelli, 2000). Shadow analysis is employed by Noronha and Nevatia (2001), Lin and Nevatia (1998) and Miura and Midorikawa (2003) to generate roof heights (see also Huertas *et al*., 1993). Building outlines are reconstructed from the perceptual organization of boundary information (see Huertas *et al*., 1993; Jaynes *et al*., 1997; also Lin and Nevatia, 1998). The accuracy of information derived from monocular imagery may be further enhanced through the use of multiple images (Nevatia *et al*., 1997; Lin and Nevatia, 1998; Noronha and Nevatia, 1998, 2001).

Representing the scene from a range of observation angles does not necessarily afford stereoscopic viewing, for which imagery must overlap by a minimum of 60%. Stereoscopic airborne and, more recently, satellite (Baltsavias *et al*., 2001) data have been widely employed for building extraction. Correlation- and pyramid-based matching (see Kim and Choi, 1995; also Haala, 1999) of scenes that provides a realistic 3-D reconstruction of the scene below, from which height data can be extracted in point format. Elevation may be computed from points corresponding with roof vertices (Forstner, 1999; Suveg and Vosselman, 2000; Baltsavias *et al*., 2001; Nevatia and Price, 2002), through the use of planar and apex roof models (Kim and Choi, 1995), or using multi-line triangulation with back projection to the ground level as defined by a terrain model (Collins *et al*., 1995; Riseman *et al*., 1995; Jaynes *et al*., 1997; Heuel and Kolbe, 2001; Suveg and Vosselman, 2001; Rottensteiner and Jansa, 2002). Elevation readings are also interpolated to form a continuous digital model (Collins *et al*., 1995; Haala and Brenner, 1999c; Nevatia and Price, 2002) from which buildings may be crudely located (Kim *et al*., 2001), using standard image processing software (Weidner and Forstner, 1995; Jaynes *et al*., 1997). Detailed building delineation requires a very high resolution DEM, such as that obtained by Vestri and Devernay (2000) using multiple views.

Building outlines can be derived by manual digitization (Baltsavias *et al*., 2001), a knowledge-base approach (Ameri, 2000; Heuel and Kolbe, 2001; Suveg and Vosselman, 2001), and from cues obtained through segmentation or feature extraction (Collins *et al*., 1995; Weidner and Forstner, 1995; Forstner, 1999; Fradkin *et al*., 1999; Eidenbenz *et al*., 2000; Heuel and Kolbe, 2001; Kim *et al*., 2001) that may be localized using contour concatenation (Suveg and

4

Vosselman, 2000). This is followed by reconstruction based on perceptual grouping (Riseman *et al*, 1995; Guindon, 1997; Heuel and Kolbe, 2001), which is refined by Nevatia and Price (2002) with Bayesian decision-making techniques.

As shown in Figure 2-1, a number of previous studies integrate optical coverage with alternative remote sensing datasets. In some instances, the optical data provides information concerning height, and in others, footprint. Suveg and Vosselman (2000, 2001) combine stereo-derived height information with footprints defined on ground plans. In contrast, Haala (1999), Haala and Brenner (1999) demonstrate the integration of optical photography with a LIDAR range data (see also Rottensteiner and Jansa, 2002) for the hierarchical classification of landuse, separating building hypotheses from vegetated and shadowed areas. McIntosh *et al*. (1999) extract building outlines from stereo images, which are combined with LIDAR-generated heights. Xu and Li (1998, 2001) and Lemmens (2002) document a similar operation, based on outlines derived from monocular imagery.

2.2   LIDAR Data

Laser range or 'LIDAR' data offers an unprecedented level of topographic detail for urban environments. However, the widespread implementation of this active sensing device has been somewhat constrained by the limited spatial coverage and resultantly, large number of overflights required for urban mapping. LIDAR is an active remote sensing device, with ground surface elevation readings computed in terms of distance, derived from readings of the run-time between signal emission and return. These point samples are interpolated into a regular spaced grid that can be displayed in grayscale raster format as a digital surface model (DSM). For building extraction, initial data processing involves separating surface objects from the bare underlying terrain. The resulting 'normalized DSM' (Haala, 1999) is obtained by subtracting elevation readings in a bare earth digital terrain model (DTM). More commonly, it is derived from the original DSM through statistical manipulation (see Weidner and Forstner, 1995; Haala, 1999; Haala and Brenner, 1999b; Rottensteiner and Breise, 2002; Rottensteiner and Jansa, 2002). Huyck et al. (2002) provide an approach for extracting building height from the bare-earth that is based on a series of filters that are designed for highly urban areas.

Detailed reconstruction of individual buildings

Brenner and Haala (1998)
Forstner (1999)
Gamba and Houshmand (1999, 2000)
Haala and Brenner (1999c)
Heuel and Kolbe (2001)
Kim et al. (2001)
Nevatia et al. (1997)
Noronha and Nevatia (1998, 2001)
Sohn and Dowman (2001)
Stilla and Jurkiewicz (1999)
Suveg and Vosselman (2000, 2001)

Extracting a small ensemble of buildings

Baltsavias et al. (2001)
Bolter and Leberl (2000b,c,d,e)
Bruun (2000)
Collin et al. (1995)
Haala (1999)
Haala and Walter (1999)
Huertas et al. (2000)
Jaynes et al. (1997)
Kim and Choi (1995)
Leberl and Bolter (2002)
Lin and Nevatia (1998)
Maas (1999a)
Madhavan et al. (2002)
McIntosh et al. (1999)
Nevatia et al. (1997)
Nevatia and Price (2002)
Noronha and Nevatia (1998, 2001)
Weidner and Forstner (1995)

Extracting multiple buildings at city block scale

Brenner (1999)
Chilton et al. (1999)
Forstner (1999)
Gamba and Houshmand (2000)
Haala and Brenner (1999b,c)
Rottensteiner and Briese (2002)
Rottensteiner and Jansa (2002)

Figure 2-1 Schematic Representation of Studies Addressing Building Extraction at Detailed, Ensemble and City-Wide Spatial Scales

Although buildings are generally higher than surrounding terrain, further processing is needed to distinguish between man made features of interest and spurious objects of a similar height, such as trees. Maas (1999b) and Gamba and Houshmand (2000) provide an overview of the classificatory approach employed for this segmentation process. Rottensteiner and Jansa (2002) employ shape cues coupled with a simple height threshold (see also Forstner, 1999; Xu and Li, 2001; and Madhavan *et al*., 2002. Haala (1999) documents the use of sequential returns recorded by advanced laser imaging devices. A range of height texture measures are also employed, including: the slope (Maas, 1999a,b); second derivative (Axelsson, 1999; Rottensteiner and Jansa, 2002 and Madhavan *et al*., 2002); and local variance of normal vectors (Rottensteiner and Briese, 2002).

To identify building footprints, Gamba and Houshmand (2000) and Rottensteiner and Briese (2002) define planar patches using region growing techniques. For a representative building height within these patches, or regions of interest, Rottensteiner and Jansa (2002) employ the mean, and Chilton *et al*. (1999) the upper 5-15% of values.

As shown in Figure 2-1, previous studies integrate LIDAR coverage with a number of alternative remote sensing datasets. During landuse classification, designed to distinguish buildings from other terrain features, Haala (1999), Haala and Brenner (1999) employ monocular imagery. Optical scenes are also used by Xu and Li (1998, 2001), McIntosh *et al* (1999) and Lemmens (2002) to define building outlines, a task for which Brenner and Haala (1998), Chilton *et al*. (1999), Haala and Brenner (1999b,c) and Stilla and Jurkiewicz (1999) rely on predefined ground plans.

2.3   SAR Data

Synthetic aperture radar (SAR) systems are active remote sensing devices, which operate by transmitting and recording microwave signals through a sideways looking sensor or antenna. While conventional SAR imaging requires a single sensor, an Interferometric SAR (IfSAR) product may also be derived from duel signals separated by a baseline distance. From the literature, both data sources have been employed for building extraction (see also Figure 2-1).

SAR sensors record earth surface characteristics as a series of echoes from the emitted signal. The signal comprises two measurements: (1) phase or signal round-trip time; and (2) signal strength, from which intensity magnitude is derived. While the appearance of objects recorded by optical devices strongly resembles the human visual system, radar return represents backscatter from the surface below. This varies with respect to a number of factors, including: the size and orientation of surface features; surface material and roughness; sensors observation or 'look' angle; and moisture content within the target area. Buildings look particularly 'bright' on SAR imagery, as the incoming radar beam bounces back. Features such as this, are therefore referred to as 'corner reflectors'. Due to the off-nadir or sideways method of sensing, shadowing, layover and foreshortening are common phenomenological effects. Of particular interest for the present study is the shadow that occurs where a terrain feature blocks the line of sight between the sensor and areas beyond (see Bolter, 2000; Bolter and Leberl, 2000b). This

shadowing effect is instrumental in the extraction of buildings by Kirscht and Rinke (1997). The SAR imagery is initially segmented using statistical techniques to distinguish building hypotheses. Assuming a priori knowledge of ground height from an external DTM, building elevation is then calculated from the estimated radial shadow length and system parameters.

IfSAR techniques employ duel radar returns (for a useful introduction to SAR interferometry, see Allen, 1995) to generate elevation data. These returns may be recorded by a pair of antennas mounted on a single airborne or satellite platform (termed single-pass interferometry). Alternatively, the pairing may comprise a temporal sequence of images, acquired in succession by just one antenna (repeat-pass interferometry). The change in phase between these returns is indicative of height differences. Using the technique of phase unwrapping (source), relative height readings are computed on a per pixel basis.

Gamba and Houshmand (2000) present IfSAR data as a comparatively new tool for building extraction. A comprehensive methodological sequence is documented, employing segmentation, seeding and successive region growing techniques to define planar patches corresponding with buildings. An assumption is then made that the building footprint relates to the area occupied at mean roof level. Height is taken as the mean value of the highest plane within this delineated region, adjusted using an IfSAR correlation map to exclude unreliable values affected by shadowing and layover.

Building reconstruction is undertaken by Bolter and Leberl (2000b,c) using *multiple* IfSAR scenes, acquired from the four cardinal azimuth directions. From a combined height map, where the pixel value is posted as the maximum azimuthal return (Bolter and Leberl, 2000a,c,d,e; Leberl and Bolter, 2002), the distinction between elevated objects and the bare earth is made using filtering, differencing and thresholding techniques (Bolter, 2000; Bolter and Leberl, 2000c,d,e; Leberl and Bolter, 2002). Buildings are then separated from natural features, such as trees, through textural analysis of coherence and height (Bolter and Leberl, 2000c,d,e). Finally, a shadow segmentation technique produces outlines for refining the crude elevation-based building hypotheses (for details, see Bolter and Leberl, 2000b). A maximum height value is assigned to this region of interest. For IfSAR derived building elevations, Bolter and Leberl (2000c) report

(an or a!) RMS error of +/-1.6m, Bolter and Leberl (2000e) RMS error of +/- 0.7m, and Bolter and Leberl (2000b) a range of –2m< RMS< 1.1m.

Gamba and Houshmand (1999) employ a combination of optical and IfSAR data to determine whether data integration can replicate the superior level of detail and accuracy commensurate with LIDAR coverage, while benefiting from the low cost synoptic coverage afforded by SAR airborne sensors. Here, the optical scenes serve as a landuse classification tool. To obtain IfSAR elevations, segmentation provides a basis for extracting planar surfaces corresponding with buildings. The resulting elevation data is corrected to a normalized form, using an IfSAR bare earth DTM, derived from the original elevation grid through low pass filtering. Building elevation is defined by the distribution of height values within the optically classified footprint. From a comparative evaluation of IfSAR and LIDAR scenes for building extraction, Gamba and Houshmand (1999, 2000) conclude that while the pixel accuracy achieved using IfSAR is less than the one for LIDAR coverage, dimensions of dominant structures, such as tall buildings, are well represented. Furthermore, integration of optical coverage significantly enhances the analytical process.

Huertas *et al*. (2000) also focus on the integration of IfSAR data with external sources. However, in this case, the SAR data merely serves to enhance results obtained using optical imagery. First, a series of building cues are derived from the SAR coverage. This involves a weighted combination of filtered magnitude and elevation data. Accompanying correlation data isolates objects above the ground surface, by filtering out pixels with low decorrelation values. These IfSAR building hypotheses provide a basis for refining building outlines defined on optical coverage through feature extraction techniques (see Section 2.1).

2.4   Spatial Scales of Analysis

The extraction of buildings from remote sensing imagery has been undertaken at a range of spatial scales. As summarized in Figure 2-1, a broad distinction can be made between studies focusing on:

- Detailed extraction of individual structures
- Extraction of a small group or 'ensemble' of structures
- Extended city-wide building extraction, undertaken at census tract or higher

The detailed reconstruction of individual structures is widely documented in the literature. Here, the focus is on achieving a faithful representation of building geometry, emphasizing factors including roof type and pitch (see, for example, Brenner and Haala, 1998; Chilton et al. 1999; Ameri, 2000; Suveg and Vosselman, 2000), in addition to footprint area and height. Studies transcend the full range of geometric complexity exhibited by the subset of rectilinear structures. Alternative classes of building models are defined by Weidner and Forstner (1995) and Brenner (2000), but receive comparatively little attention. Suveg and Vosselman (2000, 2001) concentrate on generic low-rise flat or simple peaked roof structures. More complex multi-wing and L-shaped arrangements are featured by a number of authors (Huertas et al., 1993; Nevatia et al., 1997; Noronha and Nevatia, 1998; Axelsson, 1999; Stilla and Jurkiewicz, 1999; Brenner, 2000; Gamba and Houshmand, 1999, 2000; Stassopoulou and Caelli, 2000; and Kim *et al,* 2001). Jaynes *et al*. (1997) and Heuel and Kolbe (2001) reconstruct a wider range of more complex structures using a top down approach, where building primitives are matched to a family of prototypes.

Nevatia et al. (1997) Brenner and Haala (1998), Lin and Nevatia (1998) Noronha and Nevatia (1998, 2001) and Forstner (1999) progress from the detailed reconstruction of single buildings to a larger ensemble of structures. For loss estimation, their detailed reconstruction of roof types and façades can be key to estimating damage from windstorms. The simple representation afforded by Bolter and Leberl (2000b,c,d) is limited to key information concerning height and footprint. Examples of building extraction across a wider urban extent are cited by Brenner (1999) for Heidelberg, Haala and Brenner for Stuttgart, Gamba and Houshmand (2000) for Los Angeles, Nevatia and Price (2002) for Washington D.C., and Rottensteiner and Briese (2002) and Rottensteiner and Jansa (2002) for Vienna.

Most studies undertaken at ensemble and city-wide scales focus on urban environments. However, few make the linkage between prevailing landuse and geometric idiosyncrasies of the building stock. Different types of buildings typify the principal classes of residential, industrial and commercial landuse. For example, low-rise apartments and single-family dwellings dominate residential districts. High-rise offices are often indicative of commercial, and factories of industrial development. While no formal specification is provided, from visual inspection of figures accompanying the text, it appears that Collins et al. (1995) Lin and Nevatia (1995)

Nevatia et al. (1997) and Jaynes et al. (1997) perform building extraction in a predominantly industrial landscape. Haala (1999), Maas (1999a) Rottensteiner and Briese (2002), and Rottensteiner and Jansa (2002) focus on residential, and Forstner (1999), Gamba and Houshmand (2000) and Nevatia and Price (2002) high-rise commercial environments. Other ambiguous scenes include: mixed residential and commercial in Brenner and Haala (1998), Brenner (1999) and Haala and Brenner (1999b); a university campus (Baltsavias et al., 2001); an MOUT (Military Operations on Urbanized Terrain) test site (Bolter and Leberl, 2000b-d; Huertas et al., 2000; and Leberl and Bolter, 2002); and a downtown scene including historical buildings (Haala and Brenner, 1999c). In the only example of its kind identified to date, Chilton et al. (1999) explicitly distinguish between residential and industrial areas prior to building extraction.

2.5   Advantages and Limitations

Table 2-1 summarizes the principal advantages and limitations associated with each remote sensing device. The accompanying discussion presented in this section, highlights the principal considerations at each stage of the building extraction process, from image acquisition, through data manipulation, to height and footprint estimation.

As well established sources of planimetric and height information, monocular and stereoscopic aerial photography are widely available in countries throughout the world. Offering localized coverage and a detailed representation of the scene below, optical airborne imagery is an excellent source of data for detailed studies on a per building or ensemble basis. Although many scenes would be required for the synoptic overview demanded by loss estimation purposes, newly available data from high-resolution satellite sensors such as IKONOS and QuickBird, promises wide coverage within a single image. Covering a fairly wide tract with reasonable planimetric detail, airborne SAR is an appropriate source of city-wide building data. The next generation of high-resolution satellite SAR sensors will provide global coverage, offering an opportunity to extend the use of this technology beyond the few countries with airborne devices. In contrast to SAR, the narrow LIDAR swath width necessitates a large number of overflights. The timing of data acquisition is unrestricted for SAR and LIDAR sensors. As active devices which penetrate cloud cover, these offer 24/7, all weather viewing capabilities. Optical coverage is limited to clear conditions and daylight hours.

In theory, each of the principal sensors provides sufficient information for computing building height and footprint. Single source data extraction techniques are well established for monocular and stereo imagery, while recent studies outline procedures for IfSAR. The use of LIDAR intensity data as a potential classificatory tool is poorly established. Although integration of multiple data sources enhances the results obtained, the data processing effort increases significantly.

Spatial resolution is another source of variance in sensor performance. LIDAR offers height data at a superior level of detail, particularly in urban areas. The pixel posting for SAR imagery is wider, and aerial photography is subject to interpolation between point samples. Surrogate measures such as shadow length are used to generate height data from monocular images. Although spatial resolution is less of an issue in this case, given the detailed representation offered by aerial photography, obtaining 3-D measures from 2-D data is inherently ambiguous and subject to considerable error. In terms of building footprint, outlines are difficult to derive from optical imagery. Image processing techniques produce noisy results. LIDAR records roof margins with reasonable accuracy, based on change in elevation. Building outlines are poorly delineated on SAR coverage, due to system noise and the wide range of surface effects influencing the return signal. Studies typically employ an alternative source of outline data.

Sources of error introduced during imaging profoundly affect the results obtained. Occlusion or shadowing is a limitation of all sensors, although it is particularly acute for off-nadir viewing stereo and SAR devices. SAR imagery is also subject to layover and foreshortening. In the former case, returns from multiple ground surface features are received simultaneously. In the latter, the emitted wave reaches the base of a long gradual feature prior to the top, effectively shortening its dimensions. Similarity between the characteristics of buildings and other ground surface features, such as trees, is another source of error. Heights are often comparable in IfSAR stereo and LIDAR elevation models. Overhanging trees also compromise the performance of feature extraction algorithms designed to isolate continuous rectilinear building outlines in urban areas.

Table 2-1 Advantages and Disadvantages of Different Data Sources for Detecting Buildings and Determining their Height and Footprint

GEOSPATIAL DATA SOURCE	ADVANTAGES	DISADVANTAGES
(1) Monocular optical imagery	• Monocular aerial photography is widely available. High resolution global coverage will soon be available from IKONOS. • Height and footprint information can be derived from a single source of remote sensing data. • Data requirements are lenient. Procedures can deal with both vertical and off-nadir images. • Data is comparatively cheap to acquire and process	• Data acquisition is limited to daylight hours and cloud-free conditions • Viewing geometry (camera model) of the imagining system usually has to be known. • Many scenes are required to achieve city-wide coverage • Building boundaries are difficult to distinguish from other rectilinear background features such as roads, sidewalks and parking lots • Obtaining 3D measurements from 2D data is inherently ambiguous, and consequently subject to error. Orthophotographs are particularly problematic. Methods rely purely on inference. • Cues are often occluded by other features, highly fragmented, and difficult to distinguish from shadows, texture and noise. • Models are generally limited to simple rectilinear structures, and have difficulty detecting and reconstructing complex building shapes
(2) Stereo optical imagery	• High-resolution global coverage will soon be available from IKONOS. • Height and footprint information can be derived from a single source of remote sensing data • Automated stereo image matching programs are available to reconstruct a 3D visualization as the basis for height measurement • Building outlines are clearly depicted, avoiding blurred margins	• Data acquisition is limited to daylight hours and cloud-free conditions • Many scenes are required to achieve city-wide coverage • 3D photogrammetric reconstruction from stereo imagery is a long, slow process • Misalignment during image matching and occlusions inherent in the data affect the accuracy of stereo analysis. • Buildings are comparatively difficult to locate through image processing techniques • Depth discontinuities at building boundaries cause degradation in height accuracy. This is registered as blurring around building margins. • Buildings and natural topographic features, such as trees, produce a similar response on derived elevation models • Studies are generally limited to individual buildings and groups of structures • Production of height and footprint information is comparatively costly

Table 2-1 (cont) Advantages and Disadvantages of Different Data Sources for Detecting Buildings and Determining their Height and Footprint

GEOSPATIAL DATA SOURCE	ADVANTAGES	DISADVANTAGES
(3) LIDAR imagery	• 24/7 viewing capability • Point samples are readily converted to continuous raster format • Source of DSM and DTM models at comparable spatial scales • High-density elevation data offers a realistic impression of building footprints without the use of outlines • LIDAR provides height readings with high vertical and reasonable planimetric accuracy. DSMs are particularly realistic in dense urban environments • Building hypotheses are easily located by simple thresholding techniques	• Due to the narrow swath width of LIDAR imagery, numerous time-consuming overflights are required to achieve full coverage. • No satellite-based LIDAR sensors are currently in operation • In dense urban environments, occluded areas occur where there is zero LIDAR return • Buildings and natural topographic features, such as trees, produce a similar response on LIDAR elevation models • Building margins are imprecisely defined • Data acquisition and processing are relatively high-cost
(4) SAR/IfSAR imagery	• Airborne devices have a wide swath, providing synoptic coverage and high-resolution sampling • SAR data acquisition is rapid • All weather, 24/7 viewing capability • Height and footprint information can be derived from a single source of remote sensing data • Provides reasonably high density elevation readings that are readily converted to continuous raster format • Source of interferometric DSM and DTM models at comparable spatial scales • IfSAR derived building elevations are typically accurate, because the radar backscatter signal from such geometrical structures is strong • Building hypotheses are easily located by simple thresholding techniques • Associated intensity, coherence and correlation images can be used to distinguish between buildings and trees • Data acquisition and processing is comparatively low cost	• At present, SAR systems mounted on satellite platforms offer comparatively low resolution data • SAR data is corrupted by blur and speckle/noise • Co-registration of SAR images with other remote sensing data is often problematic in the absence of 1:1 pixel correspondence. • The stability of IfSAR building models is questionable. Results may vary with look angle, orientation and flight path. • IfSAR is based on a pair of closely aligned SAR images, requiring additional computational effort • SAR range data is comparatively difficult to interpret, due to the wide range of surface effects influencing the return signal. • Shadowing creates a 'no data' area beyond elevated terrain features. A 'front porch effect' is created by layover, where the near-range side of a building is characterized by elevation readings intermediate between ground and rooftop values. • The accuracy of heights for low-rise structures is compromised by system noise • Phenomenological effects of shadowing, foreshortening and layover distort the appearance of surface features • Buildings and natural topographic features, such as trees, produce a similar response on IfSAR elevation models

2.6   Remainder of Report

The remainder of this report concentrates on one of the techniques to generate 3-D models of buildings from single-view optical satellite imagery, i.e., monocular optical imagery.   As explained in the first chapter of this report, this work was initially performed by Dr. Sarabandi under several tasks that were developed to support MCEER's human threat work.   Although Dr. Sarabandi's research covered more than 3-D building modeling, only work that focuses on this topic is presented here.   The reader is encouraged to obtain a copy of Dr. Sarabandi's dissertation to examine in more depth issues related to building inventory development for loss modeling or estimation.

SECTION 3
FUNDAMENTALS OF 3-D SCENE MODELING

3.1 Overview

Recent advances in high-resolution satellite imaging extended the application of commercial satellite images - such as those acquired by IKONOS, Quickbird or OrbView - to accurate 3-D building modeling and geospatial information extraction. Furthermore, remote sensing technology is rapidly gaining popularity among urban planning, disaster management, emergency response and insurance communities because of its capability in acquiring considerable amount of geospatial information, with high repeatability in a relatively short amount of time.

In this chapter, the basic concepts, terminologies and fundamentals of 3-D terrain modeling from optical satellite images are introduced. First, different sensor orientation models are introduced. Detailed discussions about the rigorous (physical) and generic optical satellite sensor models as well as modeling different sources of optical noise such as lens distortions are then presented. In the later sections of this chapter, a method for estimating parameters of the generic satellite orientation models is introduced. The fundamentals introduced in this chapter are then used as bases for 3-D reconstruction algorithms developed in Chapter 4.

3.2 Sensor Orientation Models

Sensor models in imaging systems are divided into two main categories; *rigorous* or *physical* sensor models and *generic* or *replacement* sensor models. Both of these models describe a relationship between three-dimensional object space on the ground and its two-dimensional projection on the imaging plane. A rigorous sensor model is a physical model that accurately maps object coordinates to image coordinates using interior and exterior sensor orientations. Rigorous sensor models are sensor dependent, i.e. different types of sensors have different models (Tao and Hu, 2001a). Generalized sensor models on the other hand are sensor independent such that one can perform photogrammetric processing without the knowledge of the orientation parameters, sensor type or the physics of the imaging process. The following sections describe in more detail the orientation parameters as well as the different sensor models.

3.2.1 Intrinsic Sensor Parameters

Intrinsic sensor parameters or the interior orientations of an imaging system include parameters describing the physical relationships among the different components of the camera such as optics and mechanical alignments. Intrinsic parameters, among many, include focal length, projection center, principal point, field of view, coordinates of the central point in the imaging plane and radial symmetric lens distortions. The elements of interior orientation can be determined with great precision using well-controlled test-range imagery. Therefore, it is not necessary or desirable to adjust the interior orientation during standard imaging operations.

3.2.2 Extrinsic Sensor Parameters

Extrinsic sensor parameters or exterior orientations constitute parameters defining a sensor's position in space, i.e. the satellite *ephemeris*, and the viewing angle, i.e. the satellite *attitude*. On-board GPS receivers determine the satellite's ephemeris, i.e. camera's orbital position as a function of time. Ephemeris errors are called in-track, cross-track and radial errors. Star trackers and gyros determine the attitude as a function of time. Attitude angles are *roll* (rotation about in-track direction), *pitch* (rotation about cross-track rotation) and *yaw* (rotation about the radius from the center of the Earth).

3.3 Rigorous Sensor Models

A rigorous sensor model is a physical model which maps the object-coordinates in a three-dimensional space to the image-coordinates in a two-dimensional space using intrinsic and extrinsic sensor parameters. Rigorous sensor models are sensor dependent, meaning that different types of sensors have different models (Tao and Hu, 2001a). In these types of models, parameters are statistically uncorrelated and each parameter has a certain physical significance (Tao and Hu, 2001a). The most commonly-used projection model for central perspective cameras is the well-known *collinearity model*. *Collinearity condition* states that a point in the object-space, its corresponding projection on the imaging plane and the camera's projection center lie on a straight line, as shown in Figure 3-1. In this figure, *XYZ* is the reference frame in the object-space and *UV* is the reference coordinates in the image-plane. The perspective projection model using collinearity condition can be modeled as follows:
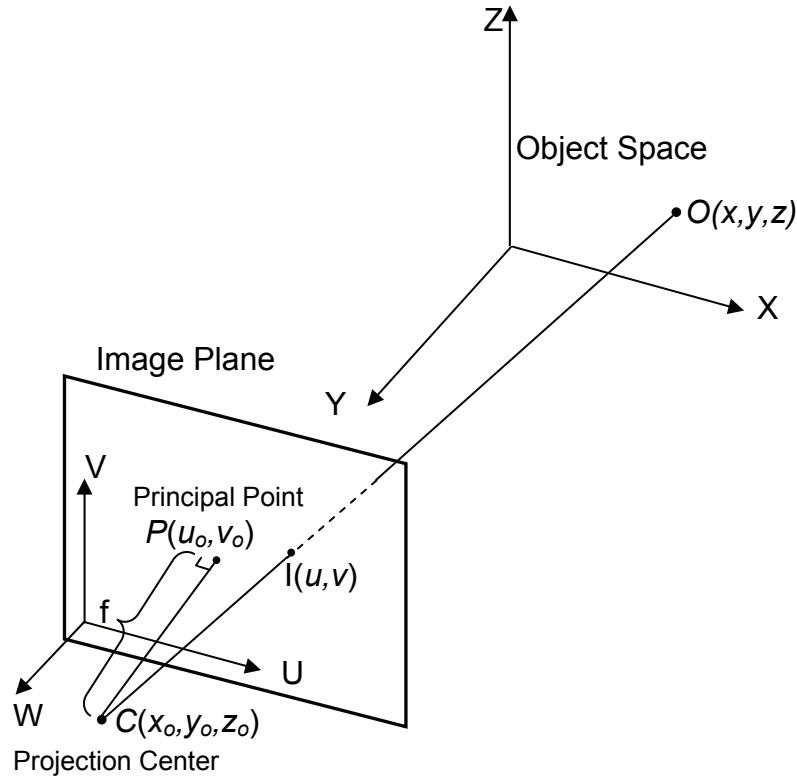
Figure 3-1 Perspective Camera Model and Collinearity Condition

Vector **CO** in the object-space coordinate system can be expressed as $(x-x_o,\ y-y_o,\ z-z_o)$. Adding the W axis to the image coordinate system such that it is perpendicular to the imaging plane makes the image-space a three-dimensional coordinate system with a W-coordinate of zero for all the points in that plane. The projection of point C onto the imaging plane is called the principal point and is denoted by $P(u_o,v_o)$ in Figure 3-1. Vector **CP** is perpendicular to the image-plane and is parallel to W-axis. The distance from the projection center to the plane is known as the principal distance or the *focal length* and is identified by f in Figure 3-1. Consequently, the projection center C in UVW coordinate system has coordinates of $(u_o,\ v_o, f)$. Vector **CI** in UVW frame can be expressed as $(u-u_o,\ v-v_o\ ,-f\ )$. The collinearity condition states that points O, I and C are on a straight line hence, vectors **CI** and **CO** are parallel to each other. Equation 3-1 shows the relationship between vectors **CI** and **CO**.

$$\vec{CI} = \alpha \cdot \vec{CO} \qquad \text{where } \alpha \text{ is a scaling scalar} \tag{3-1}$$

Vector **CO** - in the object-space coordinate system *XY Z* - can be equivalently expressed in the image-coordinate system *UVW* using the transformation matrix *R* as shown in Equation 3-2.

$$\vec{CO}_{XYZ} = R(\omega, \phi, \kappa) \cdot \vec{CO}_{UVW} = \begin{bmatrix} r_{11} & r_{12} & r_{13} \\ r_{21} & r_{221} & r_{23} \\ r_{31} & r_{32} & r_{33} \end{bmatrix} \cdot \vec{CO}_{UVW} \tag{3-2}$$

where $R(\omega, \phi, \kappa)$ is the orthogonal rotation matrix between the image and the object-space coordinate systems composed of three rotation angles ω, ϕ and κ also known as the attitude angles as expressed in Equations 3-3a and 3-3b.

$$\begin{cases} r_{11} = \cos(\omega)\cos(\kappa) \\ r_{12} = \cos(\omega)\sin(\kappa) \\ r_{13} = -\sin(\omega) \\ r_{21} = \sin(\phi)\sin(\omega)\cos(\kappa) - \cos(\phi)\sin(\kappa) \end{cases} \tag{3-3a}$$

$$\begin{cases} r_{22} = \sin(\phi)\sin(\omega)\sin(\kappa) + \cos(\phi)\cos(\kappa) \\ r_{23} = \cos(\omega)\sin(\phi) \\ r_{31} = \cos(\phi)\sin(\omega)\cos(\kappa) + \sin(\phi)\sin(\kappa) \\ r_{32} = \cos(\phi)\sin(\omega)\sin(\kappa) - \sin(\phi)\cos(\kappa) \\ r_{33} = \cos(\omega)\cos(\phi) \end{cases} \tag{3-3b}$$

Therefore:

$$\begin{Bmatrix} u - u_o \\ v - v_o \\ -f \end{Bmatrix} = \alpha \cdot \begin{bmatrix} r_{11} & r_{12} & r_{13} \\ r_{21} & r_{221} & r_{23} \\ r_{31} & r_{32} & r_{33} \end{bmatrix} \cdot \begin{Bmatrix} x - x_o \\ y - y_o \\ z - z_o \end{Bmatrix} \tag{3-4}$$

or

$$\begin{cases} u - u_o = \alpha \cdot [r_{11}(x - x_o) + r_{12}(y - y_o) + r_{13}(z - z_o)] \\ v - v_o = \alpha \cdot [r_{21}(x - x_o) + r_{22}(y - y_o) + r_{23}(z - z_o)] \\ -f = \alpha \cdot [r_{31}(x - x_o) + r_{32}(y - y_o) + r_{33}(z - z_o)] \end{cases} \tag{3-5}$$

so:

$$\alpha = -\frac{f}{[r_{31}(x - x_o) + r_{32}(y - y_o) + r_{33}(z - z_o)]} \tag{3-6}$$

and therefore:

$$u - u_o = -f \frac{r_{11}(x - x_o) + r_{12}(y - y_o) + r_{13}(z - z_o)}{r_{31}(x - x_o) + r_{32}(y - y_o) + r_{33}(z - z_o)}$$

$$v - v_o = -f \frac{r_{21}(x - x_o) + r_{22}(y - y_o) + r_{23}(z - z_o)}{r_{31}(x - x_o) + r_{32}(y - y_o) + r_{33}(z - z_o)}$$

(3-7)

Equation 3-7 is known as the standard form of the collinearity equations in which *(x, y, z)* are the physical coordinates of a point in the object space and *(u, v)* are the image coordinates of the same point on the image plane. Furthermore, (x_o, y_o, z_o) are coordinates of the sensor's projection point and (u_o, v_o) is the image coordinate of the principal point. Parameters f, ω, ϕ and κ are the focal length, row, pitch and yaw of the camera, correspondingly. In this model f, u_o and v_o are the intrinsic parameters and x_o, y_o, z_o, ω, ϕ and κ are considered to be the extrinsic sensor parameters.

Unit length for all the measurements made on digital imaging systems using charged-coupled device (*CCD*) sensors are referred to as pixels, while collinearity equations presented in Equation 3-6 refer to the metric image coordinate system such as millimeter, centimeter or inch. Therefore, Equation 3-7 should be modified to accommodate a conversion between the real-life length unit and the image quantization unit, i.e. pixel. Equation 3-7 shows the collinearity equations incorporating conversion factors S_x and S_y to translate metric length to pixels.

$$u - u_o = -\frac{f}{S_x} \frac{r_{11}(x - x_o) + r_{12}(y - y_o) + r_{13}(z - z_o)}{r_{31}(x - x_o) + r_{32}(y - y_o) + r_{33}(z - z_o)}$$

$$v - v_o = -\frac{f}{S_y} \frac{r_{21}(x - x_o) + r_{22}(y - y_o) + r_{23}(z - z_o)}{r_{31}(x - x_o) + r_{32}(y - y_o) + r_{33}(z - z_o)}$$

(3-8)

Equation 3-8 can be refined more by incorporating systematic errors such as symmetrical (radial) lens distortion and decentering (tangential) lens distortion. Radial and de-centering distortions are illustrated in Figure 3-2. The model can be further expanded by including uncertainty in pixel spacing (i.e. affinity error) and the shear in the image plane (i.e. non-orthogonality error), but these terms are rarely if ever significant in modern digital-optical systems (Remondino and Fraser, 2006). Parameters describing the above systematic errors are referred to as additional parameters (*AP*) in the rigorous sensor model. Equations 3-9 and 3-10 show the extended collinearity equations considering lens distortion *AP*'s.

21

$$u - \Delta u = -\frac{f}{S_x} \frac{r_{11}(\mathrm{x}-\mathrm{x_o}) + r_{12}(\mathrm{y}-\mathrm{y_o}) + r_{13}(\mathrm{z}-\mathrm{z_o})}{r_{31}(\mathrm{x}-\mathrm{x_o}) + r_{32}(\mathrm{y}-\mathrm{y_o}) + r_{33}(\mathrm{z}-\mathrm{z_o})}$$

(3-9)

$$v - \Delta v = -\frac{f}{S_y} \frac{r_{21}(\mathrm{x}-\mathrm{x_o}) + r_{22}(\mathrm{y}-\mathrm{y_o}) + r_{23}(\mathrm{z}-\mathrm{z_o})}{r_{31}(\mathrm{x}-\mathrm{x_o}) + r_{32}(\mathrm{y}-\mathrm{y_o}) + r_{33}(\mathrm{z}-\mathrm{z_o})}$$

where:

$$\Delta u = \bar{u} \cdot (K_1 r^2 + K_2 r^4 + K_3 r^6) + P_1 \cdot (2\bar{u}^2 + r^2) + 2P_2 \bar{u}\bar{v}$$

$$\Delta v = \bar{v} \cdot (K_1 r^2 + K_2 r^4 + K_3 r^6) + 2P_1 \bar{u}\bar{v} + P_2 \cdot (2\bar{v}^2 + r^2)$$

$$\bar{u} = u - u_o$$

(3-10)

$$\bar{v} = v - v_o$$

$$r^2 = \bar{u}^2 + \bar{v}^2$$

In Equation 3-10, $K_i\,(i=1,2,3)$ and $P_i\,(\,i=1,2)$ refer to parameters describing radial lens distortion and decentering distortion, respectively.

Equations 3-9 and 3-10 can be applied to both frame cameras as well as linear CCD array sensors. The difference is that, for a frame camera, one set of extrinsic sensor parameters is needed while in linear array sensors such as Pushbroom scanners used on board of high resolution satellites such as IKONOS, Quickbird and OrbView; each scan line has its own extrinsic parameters. This means that the position of the perspective projection center $C(x_o,\ y_o,\ z_o)$ and attitude angles $\omega,\ \phi$ and κ are time variant and should be modeled correspondingly. A quadratic function can be used to assess scan line variations in time (Fraser et. al., 2006) as shown in Equation 3-11.

$$\begin{cases} x_o = (p_o)_x + (p_1)_x t + (p_2)_x t^2 \\ y_o = (p_o)_y + (p_1)_y t + (p_2)_y t^2 \\ z_o = (p_o)_z + (p_1)zt + (p_2)_z t^2 \\ \omega = (p_o)_\omega + (p_1)_\omega t + (p_2)_\omega t^2 \\ \phi = (p_o)_\phi + (p_1)_\phi t + (p_2)_\phi t^2 \\ \kappa = (p_o)_\kappa + (p_1)_\kappa t + (p_2)_\kappa t^2 \end{cases}$$

(3-11)

where p_o, p_1 and p_2 are polynomial coefficients and t corresponds to the time at which each line is scanned.
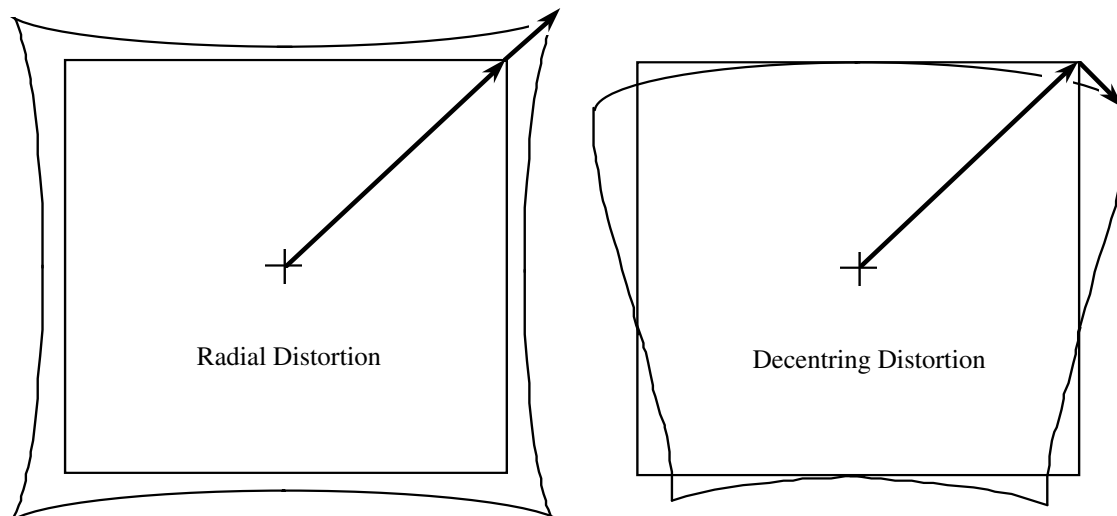
Figure 3-2 Radial and De-centering Lens Distortion

Despite the superior capability of rigorous models to accurately capture the physical characteristics of the sensor and to represent the projection from the object-space to the image-space, it should be noted that these physical models are not always available, especially for images from commercial satellites such as IKONOS, Quickbird and OrbView. It should also be noted that a great knowledge of imaging parameters such as; the orbital parameters of the satellite, sensor ephemeris, earth curvature, lens distortions, atmospheric refraction and etc. is needed in order to develop a rigorous physical model (Tao and Hu, 2001a).

3.4 Generalized Sensor Models

Generalized sensor models provide a simple and generic set of equations to accurately model the image-to-ground relationship and hence, offer an alternative for rigorous sensor models (Dial and Grodecki, 2005). In generalized sensor models, the transformation between the object-space on the ground and the image-space is represented as a general function without modeling the physical imaging process, therefore, these models are referred to as *replacement camera models*. Replacement camera models constitute a re-parameterization of the physical sensor models that usually attained through a curve-fitting process and provide users with a great deal of simplification and flexibility for applications involved real-time calculations. Generalized

models are sensor independent and therefore, eliminate the need for having a-priori knowledge about intrinsic and extrinsic sensor parameters. The three main replacement camera models are: the *Rational Function models (FRMs)*, the *Direct Linear Transform (DLT)* model and the *affine* model. These three models are discussed in more detail in the following sections.

3.4.1 Rational Function Models

A polynomial function is one that has the form of:

$$y = a_n x^n + a_{n-1} x^{n-1} + \cdots + a_2 x^2 + a_1 x + a_o \tag{3-12}$$

with *n* denoting a non-negative integer that defines the *degree* of the polynomial. A polynomial with a degree of 0 is simply a constant, with a degree of 1 is a line, with a degree of 2 is a quadratic, and so on. A *Rational Function* (*RF*) is simply the ratio of two polynomial functions as expressed in Equation 3-13.

$$y = \frac{a_n x^n + a_{n-1} x^{n-1} + \cdots + a_2 x^2 + a_1 x + a_o}{b_n x^n + b_{n-1} x^{n-1} + \cdots + b_2 x^2 + b_1 x + b_o} \tag{3-13}$$

with *n* and *m* denoting non-negative integers defining degrees of the numerator and denominator correspondingly. Coefficients a_i and b_j (*i = 0,1,...,n* and *j = 0,1,...,m)* are known as *Rational Polynomial Coefficients* (*RPCs*). The constant term in the denominator, i.e. b_o, is usually set to one when a *RFM* is to be fitted to an application.

Rational Functions are typically identified by the degrees of the numerator and denominator. For instance, a quadratic for the numerator and a cubic for the denominator is identified as a quadratic/cubic rational function. A *RFM* is generalization of polynomial models, in other words, *RFM's* contain polynomial models as a subset.

As seen from Equation 3-9, rigorous sensor model has a form very similar to rational functions so *RFM* can be thought of as a natural selection for a sensor replacement model. *RFM* uses the ratio of two polynomial functions to define the transformation between three-dimensional object-coordinates (i.e. *latitude*, *longitude* and *height*) and their corresponding two-dimensional projected coordinates on the image plane (*row* and *column*) as depicted in Figure 3-3. A *RFM*

describing ground-to-image projection is known as *forward RFM* and can be formulated as shown by Equation 3-14.

$$S_n = \frac{f_1(\phi_n, \lambda_n, h_n)}{f_2(\phi_n, \lambda_n, h_n)}$$
$$L_n = \frac{f_3(\phi_n, \lambda_n, h_n)}{f_4(\phi_n, \lambda_n, h_n)}$$
(3-14)

where S_n and L_n are the sample (column) and the line (row) indices of the pixels in the image, respectively ; ϕ_n, λ_n and h_n are geodetic latitude, geodetic longitude and height above the ellipsoid, respectively.

Most of the commercial high-resolution sensors (i.e. SPOT, IKONOS, Quickbird and OrbView) have adopted a cubic/cubic *RFM* as a replacement for their physical camera model. In cubic *RFMs*, generally the ratio of the first-order terms compensates for distortions caused by optical projection, the second-order terms can be used to correct for earth curvature, atmospheric refraction and lens distortions while the third-order terms can model other unknown distortions (Tao and Hu, 2001a).

Polynomials f_i *(i=1:4)* in Equation 3-14 have the general form of:

$$f(\phi, \lambda, h) = \sum_{i=0}^{3} \sum_{j=0}^{3} \sum_{k=0}^{3} c_{ijk} \phi^i \lambda^j h^k$$
(3-15)
where $i + j + k \leq 3$

Equation 3-15 can also be expressed as:

$$f = a_1 + a_2\lambda + a_3\phi + a_4h + a_5\lambda\phi + a_6\lambda h + a_7\phi h + a_8\lambda^2 + a_9\phi^2 + a_{10}h^2 + a_{11}\phi\lambda h$$
$$+ a_{12}\lambda^3 + a_{13}\lambda\phi^2 + a_{14}\lambda h^2 + a_{15}\lambda^2\phi + a_{16}\phi^3 + a_{17}\phi h^2 + a_{18}\lambda^2 h + a_{19}\phi^2 h + a_{20}h^3$$
$$= a^T u$$
(3-16)

where

$$a = \begin{bmatrix} a_1 & a_2 & \dots & a_{20} \end{bmatrix}^T$$
$$u = \begin{bmatrix} 1 & \lambda & \varphi & h & \lambda\varphi & \lambda h & \varphi h & \lambda^2 & \varphi^2 & h^2 & \varphi\lambda h & \lambda^3 & \lambda\varphi^2 & \lambda h^2 & \dots \\ \lambda^2\varphi & \varphi^3 & \varphi h^2 & \lambda^2 h & \varphi^2 h & h^3 \end{bmatrix}^T$$
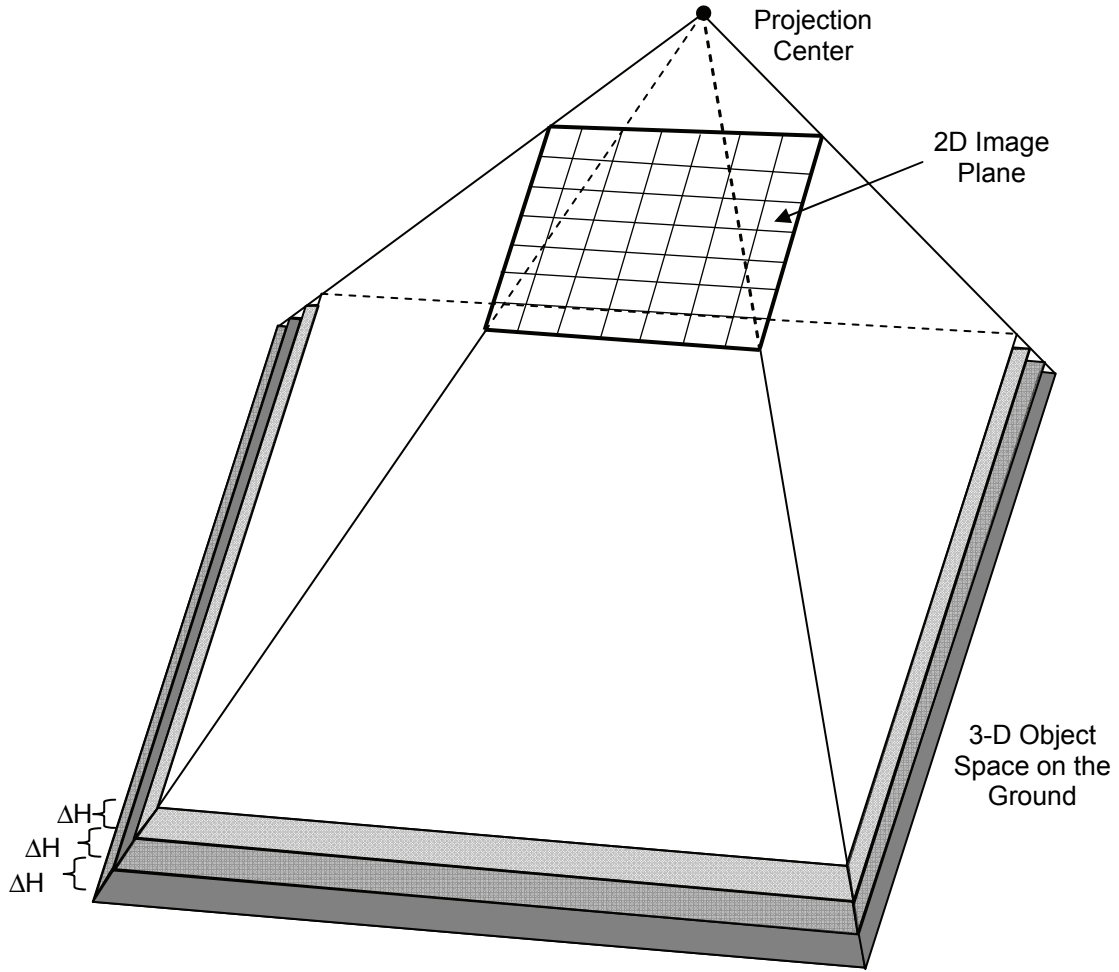
Figure 3-3 Relationship Between 3-D Object Space and Corresponding 2D Image Space in a Central Perspective Imaging System

In order to improve numerical precision, image and object coordinates in Equation 3-14 should be normalized to the range of [-1,1] by applying an offset and a scale factors to each coordinate (Grodecki, et al.,2004) as shown in Equation 3-17.

$$U = \frac{\phi - \phi_0}{\phi_s}, \quad V = \frac{\lambda - \lambda_0}{\lambda_s}, \quad W = \frac{h - h_0}{h_s}, \quad X = \frac{S - S_0}{S_s} \quad and \quad Y = \frac{L - L_0}{L_s} \tag{3-17}$$

where ϕ is the geodetic latitude, λ is the geodetic longitude, and h is the height above the ellipsoid (geoid). S and L are the image sample and line coordinates. ϕ_0, λ_0, h_0, S_0 and L_0 are the latitude, longitude, height, sample and line offsets, respectively. And, ϕ_s, λ_s, h_s, S_s and L_s are the latitude, longitude, height, sample and line scale factors, respectively.

26

Equation 3-14 can be re-written in the normalized form as shown below:

$$X = \frac{N_S(U,V,W)}{D_S(U,V,W)} = \frac{a^T u}{b^T u} \quad and \quad Y = \frac{N_L(U,V,W)}{D_L(U,V,W)} = \frac{c^T u}{d^T u}$$

(3-18)

where:

$$N_S(U,V,W) = a_1 + a_2 V + a_3 U + a_4 W + a_5 VU + a_6 VW + a_7 UW + a_8 V^2 + a_9 U^2$$
$$+ a_{10} W^2 + a_{11} UVW + a_{12} V^3 + a_{13} VU^2 + a_{14} VW^2 + a_{15} V^2 U + a_{16} U^3 + a_{17} UW^2$$
$$+ a_{18} V^2 W + a_{19} U^2 W + a_{20} W^3 = a^T u$$

$$D_S(U,V,W) = 1 + b_2 V + b_3 U + b_4 W + b_5 VU + b_6 VW + b_7 UW + b_8 V^2 + b_9 U^2$$
$$+ b_{10} W^2 + b_{11} UVW + b_{12} V^3 + b_{13} VU^2 + b_{14} VW^2 + b_{15} V^2 U + b_{16} U^3 + b_{17} UW^2$$
$$+ b_{18} V^2 W + b_{19} U^2 W + b_{20} W^3 = b^T u$$

$$N_L(U,V,W) = c_1 + c_2 V + c_3 U + c_4 W + c_5 VU + c_6 VW + c_7 UW + c_8 V^2 + c_9 U^2$$
$$+ c_{10} W^2 + c_{11} UVW + c_{12} V^3 + c_{13} VU^2 + c_{14} VW^2 + c_{15} V^2 U + c_{16} U^3 + c_{17} UW^2$$
$$+ c_{18} V^2 W + c_{19} U^2 W + c_{20} W^3 = c^T u$$

$$D_L(U,V,W) = 1 + d_2 V + d_3 U + d_4 W + d_5 VU + d_6 VW + d_7 UW + d_8 V^2 + d_9 U^2$$
$$+ d_{10} W^2 + d_{11} UVW + d_{12} V^3 + d_{13} VU^2 + d_{14} VW^2 + d_{15} V^2 U + d_{16} U^3 + d_{17} UW^2$$
$$+ d_{18} V^2 W + d_{19} U^2 W + d_{20} W^3 = d^T u$$

with:

$$u = \begin{bmatrix} 1 & V & U & W & VU & VW & UW & V^2 & U^2 & W^2 & VUW & V^3 & VU^2 & VW^2 & \dots \\ & V^2U & U^3 & UW^2 & V^2W & U^2W & W^3 \end{bmatrix}^T$$

$$a = [a_1 \quad a_2 \quad \dots \quad a_{20}]^T, \quad b = [1 \quad b_2 \quad \dots \quad b_{20}]^T$$

$$c = [c_1 \quad c_2 \quad \dots \quad c_{20}]^T, \quad d = [1 \quad d_2 \quad \dots \quad d_{20}]^T$$

This leads to 78 *RPC*'s that are commonly used and adopted by the industry.

3.4.2   Direct Linear Transform (DLT) Models

The Direct Linear transform (*DLT*) model is a subset of *RFM* with only first order terms retained in the numerator and denominator. Disregarding lens distortions and additional parameters explained by Equation 3-10, one can rewrite the rigorous sensor model shown in Equation 3-9 as the following *DLT*:

$$u = \frac{L_1 x + L_2 y + L_3 z + L_4}{L_9 x + L_{10} y + L_{11} z + 1}$$

$$v = \frac{L_5 x + L_6 y + L_7 z + L_8}{L_9 x + L_{10} y + L_{11} z + 1}$$

$$(3\text{-}19)$$

Additional parameters (*AP*) compensating for radial and de-centering lens distortions can be incorporated into Equation 3-19 to create an *Extended DLT* (*EDLT*) model as shown in Equation 3-20.

$$u = \frac{L_1 x + L_2 y + L_3 z + L_4}{L_9 x + L_{10} y + L_{11} z + 1} + \xi(L_{12}r^2 + L_{13}r^4 + L_{14}r^6) + L_{15}(r^2 + 2\xi^2) + L_{16}\xi\eta$$

$$v = \frac{L_5 x + L_6 y + L_7 z + L_8}{L_9 x + L_{10} y + L_{11} z + 1} + \eta(L_{12}r^2 + L_{13}r^4 + L_{14}r^6) + L_{15}\eta\xi + L_{16}(r^2 + 2\eta^2)$$

$$(3\text{-}20)$$

where $[\xi \;,\; \eta] = [u - u_o \;,\; v - v_o]$ and $r^2 = \xi^2 + \eta^2$

In this equation, parameters $L_1 \sim L_{11}$ are standard *DLT* coefficients, $L_{12} \sim L_{14}$ are 3rd, 5th and 7th order radial distortion terms and parameters L_{15} and L_{16} are decentering distortion terms.

There are two methods to compute coefficients L_i *(i=1:11)* in the *DLT* presented in the Equation 3-19; the direct re-parameterization of collinearity equations and the Least Square Estimate (*LSE*) of parameters using control points. Direct re-parameterization of Equation 3-9 is attainable should the interior and exterior orientations of the imaging system are known and can be expressed as below:

$$\begin{cases} L_1 = \dfrac{u_o \cdot r_{31} - f_x \cdot r_{11}}{D} \;,\; L_2 = \dfrac{u_o \cdot r_{32} - f_x \cdot r_{12}}{D} \;,\; L_3 = \dfrac{u_o \cdot r_{33} - f_x \cdot r_{13}}{D} \\[2mm] L_4 = \dfrac{(f_x \cdot r_{11} - u_o \cdot r_{31}) \cdot x_o + (f_x \cdot r_{12} - u_o \cdot r_{32}) \cdot y_o + (f_x \cdot r_{13} - u_o \cdot r_{33}) \cdot z_o}{D} \\[2mm] L_5 = \dfrac{v_o \cdot r_{31} - f_y \cdot r_{21}}{D} \;,\; L_6 = \dfrac{v_o \cdot r_{32} - f_y \cdot r_{22}}{D} \;,\; L_7 = \dfrac{v_o \cdot r_{33} - f_y \cdot r_{23}}{D} \\[2mm] L_8 = \dfrac{(f_y \cdot r_{21} - v_o \cdot r_{31}) \cdot x_o + (f_y \cdot r_{22} - v_o \cdot r_{32}) \cdot y_o + (f_y \cdot r_{23} - v_o \cdot r_{33}) \cdot z_o}{D} \\[2mm] L_9 = \dfrac{r_{31}}{D} \;,\; L_{10} = \dfrac{r_{32}}{D} \;,\; L_{11} = \dfrac{r_{33}}{D} \end{cases}$$

$$(3\text{-}20)$$

where $\begin{bmatrix} f_x & f_y \end{bmatrix} = \begin{bmatrix} \dfrac{f}{S_x} & \dfrac{f}{S_x} \end{bmatrix}$

and $\quad D = -(x_o \cdot r_{31} + y_o \cdot r_{32} + z_o \cdot r_{33})$

Equivalently, model parameters L_i *(i=1:11)* can be estimated using control points and employing a least square method. Control points must not be coplanar and should be chosen from a control volume. To obtain the *DLT* parameters and *AP*'s using a least-square method, a system of over-determined equations should be formed. As expressed in Equation 3-19, each control point corresponds to two equations hence, to estimate a model with 11, 14 or 16 parameters at least 6, 7 or 8 non-coplanar control points are required, more details about the approach can be found in (Hatze H., 1988).

DLT is widely used in close-range photogrammetry and is a suitable model for recovering the physical sensor parameters, i.e., to calculate approximate values of unknown parameters for the collinearity equations. Furthermore, due to the presence of additional parameters in the model, it can be used to model wider field angle scanners.

3.4.3   Affine Sensor Model

When the image area is relatively flat and the *relief displacement* is minimal, a first order polynomial model can be used to model the image-to-ground relationship. Affine models are a subset of *RFM* with a first order numerator and a denominator equal to unity. An affine model could precisely model the image-to-ground projection if the satellite's *field of view (FOV)* remains perfectly constant through the image. These models are simple to design and execute faster in photogrammetric applications but cannot model the high-frequency aspects of either the sensor or the terrain. Affine transformation can be used as a model for calculating the first approximation to more complicated sensor models in photogrammetric applications. A typical affine transformation is shown in Equation 3-21:

$$
\begin{aligned}
u &= a_0 + a_1 x + a_2 y + a_3 z \\
v &= b_0 + b_1 x + b_2 y + b_3 z
\end{aligned}
\tag{3-21}
$$

3.5   Estimation of Rational Function Coefficients

Rational function models used to replace the physical sensor model can be parameterized in two different forms in order to express the perspective projection structure of the camera: *a)* the *forward RFM* and *b)* the *inverse RFM*. Forward or upward *RFM* performs a transformation between the object-space and the image-space, i.e., ground-to-image projection; $(\phi_n, \lambda_n, h_n) \rightarrow (S_n, L_n)$, such that for a given set of ground-coordinates the corresponding image coordinates can be calculated. This has been formulated in previous sections as shown in the Equation 3-14. Inverse or downward *RFM,* on the other hand, expresses the image-to-ground transformation such that for a given pair of image coordinates (S_n, L_n) and height h_n above the ellipsoid, longitude λ_n and latitude ϕ_n of the corresponding ground point can be calculated, i.e. $(S_n, L_n, h_n) \rightarrow (\phi_n, \lambda_n)$. Equation 3-22 shows the canonical form of an inverse *RFM*.

$$\phi_n = \frac{f_5(S_n, L_n, h_n)}{f_6(S_n, L_n, h_n)}$$
$$\lambda_n = \frac{f_7(S_n, L_n, h_n)}{f_8(S_n, L_n, h_n)} \tag{3-22}$$

In order to estimate rational polynomial coefficients (*RPC's*) of an *RFM*, i.e., vectors **a**, **b**, **c**, and **d** in Equation 3-18, a set of corresponding coordinates in the object space and in the image space should be selected. If the rigorous sensor model is available, a *terrain independent solution* can be used. In this method, a virtual space as shown in Figure 3-4 is created by partitioning the object space into several parallel grids uniformly distributed at different elevations. Object grid points corresponding to different image grid points can then be computed on each of the elevation layers using the rigorous sensor model. Repeating this for several points on the image grid and calculating the corresponding object coordinates of each on all of the elevation layers will result in a set of corresponding points to be used in the *RPC* fitting process.

If the rigorous sensor model is not available, a *terrain dependent solution* is to be used. In this approach, a number of Ground Control Points (*GCP's*) using *GPS* measurements are selected and rational polynomial fitting is performed.

To fit a *RFM* to the virtual space or to *GCP's*, Equation 3-18 can be restructured and be expressed as below:

$$X = \frac{au^T}{bu^T} = \frac{\begin{pmatrix} a_1 & a_2 & a_3 & a_4 & \cdots & a_{19} & a_{20} \end{pmatrix}\begin{pmatrix} 1 & V & U & W & \cdots & U^2W & W^3 \end{pmatrix}^T}{\begin{pmatrix} 1 & b_2 & b_3 & b_4 & \cdots & b_{19} & b_{20} \end{pmatrix}\begin{pmatrix} 1 & V & U & W & \cdots & U^2W & W^3 \end{pmatrix}^T}$$

$$Y = \frac{au^T}{bu^T} = \frac{\begin{pmatrix} c_1 & c_2 & c_3 & c_4 & \cdots & c_{19} & c_{20} \end{pmatrix}\begin{pmatrix} 1 & V & U & W & \cdots & U^2W & W^3 \end{pmatrix}^T}{\begin{pmatrix} 1 & d_2 & d_3 & d_4 & \cdots & d_{19} & d_{20} \end{pmatrix}\begin{pmatrix} 1 & V & U & W & \cdots & U^2W & W^3 \end{pmatrix}^T}$$

(3-23)
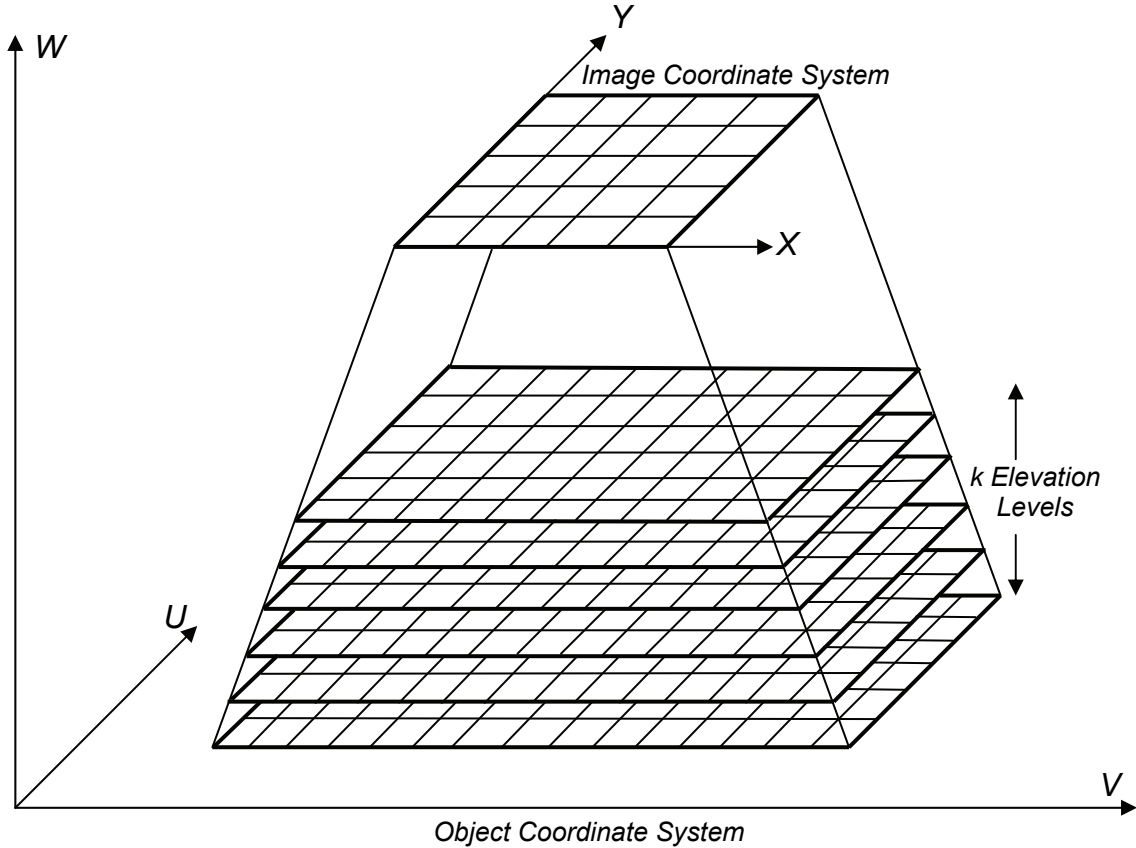
Figure 3-4 Partitioning the Object Space into Parallel Grids in Order to Fit a *RFM*

For each pair of corresponding object/image coordinates, Equation 3-23 can be re-ordered as:

$$\begin{pmatrix} a_1 & a_2 & a_3 & a_4 & \cdots & a_{19} & a_{20} \end{pmatrix}\begin{pmatrix} 1 & V & U & W & \cdots & U^2W & W^3 \end{pmatrix}^T$$
$$- X\begin{pmatrix} 1 & b_2 & b_3 & b_4 & \cdots & b_{19} & b_{20} \end{pmatrix}\begin{pmatrix} 1 & V & U & W & \cdots & U^2W & W^3 \end{pmatrix}^T = 0$$
$$\begin{pmatrix} c_1 & c_2 & c_3 & c_4 & \cdots & c_{19} & c_{20} \end{pmatrix}\begin{pmatrix} 1 & V & U & W & \cdots & U^2W & W^3 \end{pmatrix}^T$$
$$- Y\begin{pmatrix} 1 & d_2 & d_3 & d_4 & \cdots & d_{19} & d_{20} \end{pmatrix}\begin{pmatrix} 1 & V & U & W & \cdots & U^2W & W^3 \end{pmatrix}^T = 0$$

(3-24)

Equation 3-24 is nonlinear in V, U and W; but it can be seen that it is linear in the coefficients of the polynomials, i.e., in a_i's, b_i's, c_i's and d_i's ($i=1{:}20$). At least 39 corresponding object/image points are needed in order to solve for the 78 unknown *RPC's*. However, usually more than 39

points are selected and *RPC's* are estimated using least-square techniques. Equations 3-25 and 3-26 show the error equations for *k* corresponding object/image points:

$$
\begin{bmatrix} \upsilon_{X1} \\ \vdots \\ \upsilon_{Xk} \end{bmatrix} = \begin{bmatrix} 1 & \cdots & W_1^3 & -X_1 V_1 & \cdots & -X_1 W_1^3 \\ \vdots & \ddots & \vdots & \vdots & \ddots & \vdots \\ 1 & \cdots & W_k^3 & -X_k V_k & \cdots & -X_k W_k^3 \end{bmatrix} \begin{bmatrix} a_1 \\ \vdots \\ a_{20} \\ b_2 \\ \vdots \\ b_{20} \end{bmatrix} - \begin{bmatrix} X_1 \\ \vdots \\ X_k \end{bmatrix} \tag{3-25}
$$

where υ_{Xi} $(i=1,\cdots,k \geq 39)$ are error terms

$$
\begin{bmatrix} \upsilon_{Y1} \\ \vdots \\ \upsilon_{Yk} \end{bmatrix} = \begin{bmatrix} 1 & \cdots & W_1^3 & -Y_1 V_1 & \cdots & -Y_1 W_1^3 \\ \vdots & \ddots & \vdots & \vdots & \ddots & \vdots \\ 1 & \cdots & W_k^3 & -Y_k V_k & \cdots & -Y_k W_k^3 \end{bmatrix} \begin{bmatrix} c_1 \\ \vdots \\ c_{20} \\ d_2 \\ \vdots \\ d_{20} \end{bmatrix} - \begin{bmatrix} Y_1 \\ \vdots \\ Y_k \end{bmatrix} \tag{3-26}
$$

where υ_{Yi} $(i=1,\cdots,k \geq 39)$ are error terms

Equations 3-24 and 3-25 can be rewritten as:

$$V = AX - L \tag{3-27}$$

where V is the error vector to be minimized, A is the design matrix and X is the vector of unknown parameters. Coefficient vector X can be estimated by minimizing the second norm of the error vector V using least-square method. The normal Equation using weights to assure more stable results is then:

$$(A^T W A)X - A^T W L = 0 \tag{3-28}$$

Matrix W is a $k \times k$ diagonal weight matrix. If a terrain dependent approach is used, the variance in measuring *GCP*'s and their corresponding image coordinates can be calculated (by repeating the digitization of real life coordinates of control points as well as their corresponding image points) and then total variance of Equations 3-25 and 3-26 can then be calculated, i.e., $\sigma^2(\upsilon_{Xi})$ and $\sigma^2(\upsilon_{Yi})$. It is common in practice to use the reciprocal of these variances as weights associated with matrix W. More detailed discussion regarding the weight matrix for the residuals can be found in (Tao and Hu, 2001b). If control points on the object space are not evenly

distributed, it can be seen that the design matrix A quickly becomes ill conditioned and the matrix A^TWA in the normal Equation 3-28 could become singular. This problem can be solved by applying matrix regularization techniques such as the Tikhonov method. The Tikhonov regularization method is one of the most commonly used techniques for regularizing the discrete ill-posed problems. By choosing a suitable Tikhonov factor ($\alpha > 0$), a unique solution for Equation 3-27 can be obtained minimizing the following Equation:

$$\arg\min(\|V\|^2) = \arg\min(\|AX - L\|^2 + \alpha^2\|X\|^2) \tag{3-29}$$

Therefore the normal Equation 3-28 turns into a regularized form as shown in Equation 3-30.

$$(A^TWA + \alpha^2 I)X - A^TWL = 0$$
$$or \tag{3-30}$$
$$X_\alpha = (A^TWA + \alpha^2 I)^{-1} A^TWL$$

where I is a $k \times k$ identity matrix. For $\alpha = 0$, Equation 3-30 reduces to a regular least-square solution for the over-determined system of linear Equations in 3-25 and 3-26. Since matrix A^TWA is usually symmetric and positive semi-definite, the matrix $[A^TWA + \alpha^2 I]$ has eigenvalues within the interval $[\alpha^2, \alpha^2 + \| A^TWA\|]$. This means the condition number (a measure of inaccuracy of the solution for X_α), is bounded by $1 + \| A^TWA\|/\alpha^2$ which becomes smaller as α^2 increases.

SECTION 4
STEREO AND SINGLE IMAGE RECONSTRUCTION ALGORITHMS

4.1   Overview

In this chapter, an overview of 3-D reconstruction algorithms using single and stereo optical high-resolution satellite images is presented. The adopted sensor orientation model throughout this chapter is the generalized sensor replacement model in the form of *Rational Function Models* (*RFM*'s) as discussed in Chapter 3, Section 3.4.1.   A summary of reconstruction algorithms tuned for stereo and quasi-stereo images accompanied by *RFM* is first presented in this chapter. In the later part of this chapter, a methodology for extracting height and creating 3-D models of structures from a single high-resolution satellite image is presented. The proposed algorithm is a semi-automated supervised method. The associated errors due to the interactive nature of the algorithm are quantified and some solutions for minimizing the human-induced errors are proposed. The formulated height extraction algorithm is validated against independent survey data and results are presented in the corresponding section.

4.2   3-D Reconstruction Using Stereo Images

In this section, an overview of 3-D scene reconstruction using forward and inverse *Rational Function Models* (*RFM*'s) is presented. Algorithms presented in this chapter are used in Chapter 5 to extract spatial coordinates of corresponding pairs of pixels in stereo and quasi-stereo images.

4.2.1   3-D Reconstruction Using Forward RFM

As explained in Chapter 3, forward *RFM* describing ground-to-image projection can be expressed as:

$$S_n = \frac{f_1(\phi_n, \lambda_n, h_n)}{f_2(\phi_n, \lambda_n, h_n)}$$
$$L_n = \frac{f_3(\phi_n, \lambda_n, h_n)}{f_4(\phi_n, \lambda_n, h_n)}$$

(4-1)

where S_n and L_n are sample (column) and line (row) indices of pixels in the image, respectively ; ϕ_n, λ_n and h_n are geodetic latitude, geodetic longitude and height above the ellipsoid, respectively.

Equation 4-1 provides a one-to-one mapping from the object space (ϕ, λ, h), i.e., points on the ground, to the image space (S, L), i.e. pixels on the imaging plane. Using Taylor series expansion of L_n and S_n towards the three ground coordinates ϕ, λ and h, Equation 4-1 can be linearized at any given point (ϕ^*, λ^*, h^*) as follows:

$$S_n = S_n^* + \frac{\partial S_n}{\partial \phi}\Delta\phi + \frac{\partial S_n}{\partial \lambda}\Delta\lambda + \frac{\partial S_n}{\partial h}\Delta h + \varepsilon_{S_n}$$
$$L_n = L_n^* + \frac{\partial L_n}{\partial \phi}\Delta\phi + \frac{\partial L_n}{\partial \lambda}\Delta\lambda + \frac{\partial L_n}{\partial h}\Delta h + \varepsilon_{L_n}$$

(4-2)

where:

$$\frac{\partial S}{\partial Z_i} = \frac{\frac{\partial f_1}{\partial Z_i}f_2 - \frac{\partial f_2}{\partial Z_i}f_1}{f_2^{\,2}} \quad \text{where } Z_i \in \{\phi, \lambda, h\}$$

$$\frac{\partial L}{\partial Z_i} = \frac{\frac{\partial f_3}{\partial Z_i}f_4 - \frac{\partial f_4}{\partial Z_i}f_3}{f_4^{\,2}} \quad \text{where } Z_i \in \{\phi, \lambda, h\}$$

(4-3)

Polynomials f_i ($i=1:4$) in Equation 4-3 can be parameterized as 20-term cubic polynomials as previously presented in Chapter 3 in Equation 3-16. Partial derivatives of polynomials f_i ($i=1:4$) with respect to ϕ, λ and h can then be derived as shown below:

$$\frac{\partial f_i}{\partial \lambda} = (u_2 + u_5\phi + u_6 h + u_{11}\phi h + u_{13}\phi^2 + u_{14}h^2) + 2(u_8 + u_{15}\phi + u_{18}h)\lambda + 3u_{12}\lambda^2$$
$$\frac{\partial f_i}{\partial \phi} = (u_3 + u_5\lambda + u_7 h + u_{11}\lambda h + a_{15}\lambda^2 + u_{17}h^2) + 2(u_9 + u_{13}\lambda + u_{19}h)\phi + 3u_{16}\phi^2$$
$$\frac{\partial f_i}{\partial h} = (u_4 + u_6\lambda + u_7\phi + u_{11}\phi\lambda + u_{18}\lambda^2 + u_{19}\phi^2) + 2(u_{10} + u_{14}\lambda + u_{17}\phi)h + 3u_{20}h^2$$

(4-4)

where dummy variable u is replaced by a, b, c, and d for $i=1:4$.

In order to reconstruct the 3-D object-space on the ground using forward RFM, $n \geq 2$ corresponding image points (S_1, L_1), (S_2, L_2), …, (S_n, L_n) should be selected from n stereo images, as shown in Figure 4-1.
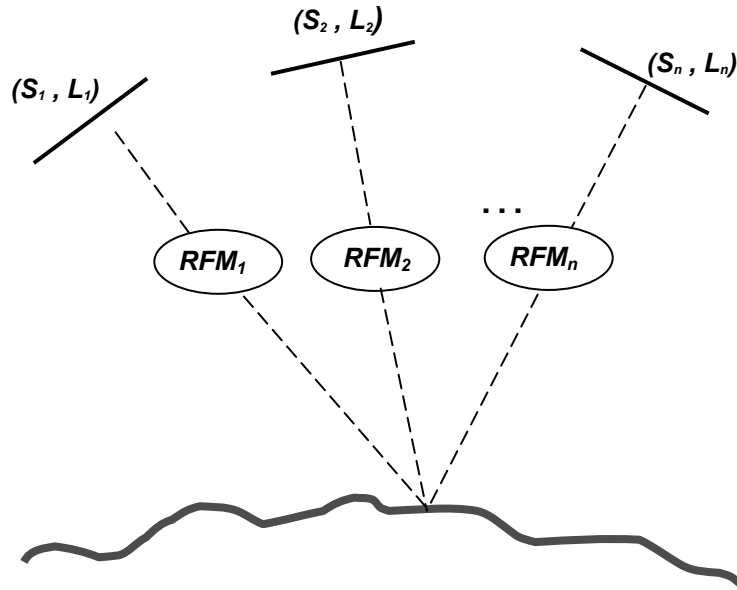
Figure 4-1 3-D Reconstruction Using Forwards *RFM*

Equation 4-1 for *n* corresponding image points can be rewritten as an error equation shown below:

$$
\begin{bmatrix} v_{S_1} \\ v_{L_1} \\ v_{S_2} \\ v_{L_2} \\ \vdots \\ v_{S_n} \\ v_{L_n} \end{bmatrix} = \begin{bmatrix} \dfrac{\partial S_1}{\partial \phi} & \dfrac{\partial S_1}{\partial \lambda} & \dfrac{\partial S_1}{\partial h} \\[2mm] \dfrac{\partial L_1}{\partial \phi} & \dfrac{\partial L_1}{\partial \lambda} & \dfrac{\partial L_1}{\partial h} \\[2mm] \dfrac{\partial S_2}{\partial \phi} & \dfrac{\partial S_2}{\partial \lambda} & \dfrac{\partial S_2}{\partial h} \\[2mm] \dfrac{\partial L_2}{\partial \phi} & \dfrac{\partial L_2}{\partial \lambda} & \dfrac{\partial L_2}{\partial h} \\[2mm] \vdots & \vdots & \vdots \\[2mm] \dfrac{\partial S_n}{\partial \phi} & \dfrac{\partial S_n}{\partial \lambda} & \dfrac{\partial S_n}{\partial h} \\[2mm] \dfrac{\partial L_n}{\partial \phi} & \dfrac{\partial L_n}{\partial \lambda} & \dfrac{\partial L_n}{\partial h} \end{bmatrix} \cdot \begin{bmatrix} \Delta\phi \\ \Delta\lambda \\ \Delta h \end{bmatrix} - \begin{bmatrix} S_1 - S_1(\phi^*,\lambda^*,h^*) \\ L_1 - L_1(\phi^*,\lambda^*,h^*) \\ S_2 - S_2(\phi^*,\lambda^*,h^*) \\ L_2 - L_2(\phi^*,\lambda^*,h^*) \\ \vdots \\ S_n - S_n(\phi^*,\lambda^*,h^*) \\ L_n - L_n(\phi^*,\lambda^*,h^*) \end{bmatrix}
\tag{4-5}
$$

which also can be shown as:

$$
v = A \cdot \Delta x - l
\tag{4-6}
$$

37

In this Equation, A is the design matrix, Δx is the unknown vector of corrections to approximate values of object-space coordinates and l is the vector of misclosures. The unknown object-space coordinates ϕ, λ and h can be calculated iteratively by minimizing the second Euclidian norm of the residual vector v as shown in Equation 4-7:

$$\min(\|v\|^2) \Rightarrow \Delta x = (A^T w A)^{-1} A^T w l \qquad (4\text{-}7)$$

where w is the weight matrix for the image points also known as the *a priori* covariance matrix of the image points. More details about the weight matrix can be found in (Grodecki et al., 2004). At each iteration step, the vector of approximate object coordinates, i.e. x^*, is replaced by $x^* + \Delta x$ and the mathematical model presented in Equation 4-1 is linearized again until convergence is obtained.

The reconstruction algorithm can be then summarized as below:

Step 1.   Given n conjugate image points, i.e. (S_1 , L_1), (S_2 , L_2), …, (S_n , L_n), set an initial value for ϕ^*, λ^* and h^*. The initial value $x^* = (\phi^*, \lambda^*, h^*)$ can be selected to be an average value for the area or can be calculated using the truncated *RFM* using only first order terms as explained in the following Section (4.2.2).

Step 2.   Using Equations 3-16 and 4-4, calculate f_i , $\dfrac{\partial f_i}{\partial \lambda}$, $\dfrac{\partial f_i}{\partial \phi}$ and $\dfrac{\partial f_i}{\partial h}$ for $i=1:4$ at the initial point $x^* = (\phi^*, \lambda^*, h^*)$ and then calculate $\dfrac{\partial S_j}{\partial \lambda}$, $\dfrac{\partial S_j}{\partial \phi}$, $\dfrac{\partial S_j}{\partial h}$, $\dfrac{\partial L_j}{\partial \lambda}$, $\dfrac{\partial L_j}{\partial \phi}$ and $\dfrac{\partial L_j}{\partial h}$ for all the n conjugate points, i.e. $j=1:n$, from Equation 4.3.

Step 3.   Calculate the correction vector Δx from Equation 4-7 and update the initial point x^* by replacing it with $x^* + \Delta x$.

Step 4.   Repeat Steps 1 to 3 and update x^* each time until maximum number of iterations is reached or $|\Delta x|$ becomes smaller than a specified threshold.

4.2.2 Initial Approximate Values in Forward RFM Reconstruction Algorithm

Initial approximate values of the object-space coordinates, i.e. $x^* = (\phi^*, \lambda^*, h^*)$ to be used in solving Equation 4-5 can be calculated using the truncated *RFM* by only considering the first-order terms. Using the normalization parameters introduced in Equation 3-17, the linearized model can be expressed as:

$$X = \frac{S - S_0}{S_s} = \frac{a_1' + a_2'\lambda^* + a_3'\phi^* + a_4'h^*}{b_1' + b_2'\lambda^* + b_3'\phi^* + b_4'h^*} + \varepsilon_X$$

$$Y = \frac{L - L_0}{L_s} = \frac{c_1' + c_2'\lambda^* + c_3'\phi^* + c_4'h^*}{d_1' + d_2'\lambda^* + d_3'\phi^* + d_4'h^*} + \varepsilon_Y$$

$$(4\text{-}8)$$

where:

$$a_1' = a_1\phi_s\lambda_s h_s - a_2\phi_s\lambda^* h_s - a_3\phi^*\lambda_s h_s - a_4\phi_s\lambda_s h^*,$$
$$a_2' = a_2\phi_s h_s, a_3' = a_3\lambda_s h_s, a_4' = a_4\lambda_s\phi_s,$$
$$b_1' = \phi_s\lambda_s h_s - b_2\phi_s\lambda^* h_s - b_3\phi^*\lambda_s h_s - b_4\phi_s\lambda_s h^*,$$
$$b_2' = b_2\phi_s h_s, b_3' = b_3\lambda_s h_s, b_4' = b_4\lambda_s\phi_s$$

and $\phi_s, \lambda_s, h_s, S_s, L_s$ are the latitude, longitude, height, sample and line scale factors, respectively.

Therefore, for *n* corresponding image points, the initial object-space coordinates can be calculated using least-square solution presented below:

$$Ax^* = b \implies x^* = (A^T A)^{-1} A^T b$$

$$(4\text{-}9)$$

where

$$A = \begin{bmatrix} a_3' - X_1 b_3' & a_2' - X_1 b_2' & a_4' - X_1 b_4' \\ c_3' - X_1 d_3' & c_2' - X_1 d_2' & c_4' - X_1 d_4' \\ a_3' - X_2 b_3' & a_2' - X_2 b_2' & a_4' - X_2 b_4' \\ c_3' - X_2 d_3' & c_2' - X_2 d_2' & c_4' - X_2 d_4' \\ \vdots & \vdots & \vdots \\ a_3' - X_n b_3' & a_2' - X_n b_2' & a_4' - X_n b_4' \\ c_3' - X_n d_3' & c_2' - X_n d_2' & c_4' - X_n d_4' \end{bmatrix}, \quad b = -\begin{bmatrix} a_1' - X_1 b_1' \\ c_1' - X_1 d' \\ a_1' - X_2 b_1' \\ c_1' - X_2 d' \\ \vdots \\ a_1' - X_n b_1' \\ c_1' - X_n d' \end{bmatrix}, \quad x^* = \begin{bmatrix} \phi^* \\ \lambda^* \\ h^* \end{bmatrix},$$

$$X_i = \frac{S_i - S_0}{S_s} \quad (i = 1, \cdots, n) \text{ and } Y_i = \frac{L_i - L_0}{L_s} \quad (i = 1, \cdots, n)$$

It is found (Tao and Hu, 2002) that for space-borne cameras carrying a linear array of pushbroom sensors (e.g. SPOT, IKONOS, Quickbird and OrbView), a first-order approximation of *RFM's* by truncating the numerator and denominator usually leads to a reasonably accurate solution. This is because usually first-order terms are larger by many orders of magnitude than the higher order terms. However, this is not the case for frame camera imagery where first-order terms are comparable in magnitude with second and third-order terms. As a result, often times the initial values obtained by neglecting higher order terms in frame camera imagery may result in a significant error.

The accuracy of the truncated *RFM* can be assessed over the entire range of valid longitudes, latitudes and heights, i.e., $\phi_0 \pm \phi_s$, $\lambda_0 \pm \lambda_s$, $h_0 \pm h_s$, by comparing the line and sample coordinates calculated with the truncated *RFM* and comparing it to the line and sample coordinates calculated using the original *RFM*. If it is determined that the truncated *RFM* is not accurate enough, alternative solutions for initial values should be considered. One alternative solution for frame cameras is to use the average value of object-space coordinates, i.e., *(ϕ_0, λ_0, h_0)* as the initial value for all the object-space points. Another alternative solution is to fit a *DLT* model as explained in Chapter 3, Section 3.4.2, to the *RFM* and use that in Equation 4-8 to calculate the initial approximate values for the starting point.

4.2.3 3-D Reconstruction Using Inverse RFM

Given the object coordinate *h*, i.e., the height above the reference ellipsoid, the inverse form of *RFM* presented in Equation 4-1 can be restructured to present image-to-ground transformation as shown in Equation 4-10.

$$
\begin{aligned}
\phi_n &= \frac{f_5(S_n, L_n, h_n)}{f_6(S_n, L_n, h_n)} \\
\lambda_n &= \frac{f_7(S_n, L_n, h_n)}{f_8(S_n, L_n, h_n)}
\end{aligned}
\tag{4-10}
$$

where ϕ_n and λ_n are geodetic latitude and longitude of points in the object space respectively; S_n and L_n are the sample (column) and the line (row) indices of pixels in image respectively ; and h_n is the height above the reference ellipsoid.

Equation 4-10 is called the *Inverse RFM*. This model expresses the relationship between planer object-coordinates of points on the ground with image-coordinates of their corresponding projections at given heights. Polynomials f_i ($i=5:8$) have the same form as Equation 3-15 and are usually of the third order. Coefficients of the inverse *RFM* can be estimated in a way similar to the forward *RFM* as explained in Chapter 3, Section 3.5.

To reconstruct the object coordinates of points on the ground, Equation 4-10 can be linearized towards the input variable h using Taylor's series expansion at (ϕ^*, λ^*, h^*) as the following:

$$\phi_n = \phi_n{}^* + \frac{\partial \phi_n}{\partial h} \Delta h + \varepsilon_\phi$$
$$\lambda_n = \lambda_n{}^* + \frac{\partial \lambda_n}{\partial h} \Delta h + \varepsilon_\lambda$$

(4-11)

where:

$$\frac{\partial \phi}{\partial h} = \frac{\frac{\partial f_5}{\partial h} f_6 - \frac{\partial f_6}{\partial h} f_5}{f_6{}^2}$$

$$\frac{\partial \lambda}{\partial h} = \frac{\frac{\partial f_7}{\partial h} f_8 - \frac{\partial f_8}{\partial h} f_7}{f_8{}^2}$$

(4-12)

The polynomials f_i ($i=5:8$) in the inverse *RFM*, presented in Equation 4-10 can be parameterized as 20-term cubic polynomials similar to their counterparts in the forward *RFM* as below:

$$f = a_1 + a_2 S + a_3 L + a_4 h + a_5 SL + a_6 Sh + a_7 Lh + a_8 S^2 + a_9 L^2 + a_{10} h^2 + a_{11} LSh$$
$$+ a_{12} S^3 + a_{13} SL^2 + a_{14} Sh^2 + a_{15} S^2 L + a_{16} L^3 + a_{17} Lh^2 + a_{18} S^2 h + a_{19} L^2 h + a_{20} h^3$$
$$= a^T u$$

(4-13)

where

$$a = [a_1 \quad a_2 \quad \dots \quad a_{20}]^T$$
$$u = [1 \quad S \quad L \quad h \quad SL \quad Sh \quad Lh \quad S^2 \quad L^2 \quad h^2 \quad LSh \quad S^3 \quad SL^2 \quad Sh^2 \quad \dots$$
$$S^2 L \quad L^3 \quad Lh^2 \quad S^2 h \quad L^2 h \quad h^3]^T$$

Therefore, partial derivatives of polynomials f_i (*i=5:8*) with respect to h can then be calculated as shown below:

$$\frac{\partial f_i}{\partial h} = (a_4 + a_6 S + a_7 L + a_{11} LS + a_{18} S^2 + a_{19} L^2) + 2(a_{10} + a_{14} S + a_{17} L)h + 3a_{20} h^2$$
$$i = 5, \cdots, 8$$

(4-14)

Given *n* conjugate image points, i.e. (S_1, L_1), (S_2, L_2), …, (S_n, L_n), as shown in Figure 4-1, and a given value for h^*, the adjustment in h^* can be calculated form the error equation below:

$$\begin{bmatrix} v_\phi \\ v_\lambda \end{bmatrix} = \begin{bmatrix} \dfrac{\partial \phi_1}{\partial h} - \dfrac{\partial \phi_2}{\partial h} - \cdots - \dfrac{\partial \phi_n}{\partial h} \\ \dfrac{\partial \lambda_1}{\partial h} - \dfrac{\partial \lambda_2}{\partial h} - \cdots - \dfrac{\partial \lambda_n}{\partial h} \end{bmatrix} \cdot [\Delta h] - \begin{bmatrix} \phi_1 - \phi_2 - \cdots - \phi_n \\ \lambda_1 - \lambda_2 - \cdots - \lambda_n \end{bmatrix}$$

(4-15)

Least-squares solution to Δh in Equation 4-15 is:

$$\Delta h = \frac{(\phi_1 - \cdots - \phi_n).W_\phi \cdot \left(\dfrac{\partial \phi_1}{\partial h} - \cdots - \dfrac{\partial \phi_n}{\partial h} \right) + (\lambda_1 - \cdots - \lambda_n).W_\lambda \cdot \left(\dfrac{\partial \lambda_1}{\partial h} - \cdots - \dfrac{\partial \lambda_n}{\partial h} \right)}{W_\phi \cdot \left(\dfrac{\partial \phi_1}{\partial h} - \cdots - \dfrac{\partial \phi_n}{\partial h} \right)^2 + W_\lambda \cdot \left(\dfrac{\partial \lambda_1}{\partial h} - \cdots - \dfrac{\partial \lambda_n}{\partial h} \right)^2}$$

(4-16)

where W_ϕ and W_λ are weights for ϕ and λ. It can be seen that an alternative solution to the correction value Δh can be found by using the reciprocal of partial derivatives of ϕ and λ with respect to h as weights as shown in Equation 4-17:

$$\Delta h = \frac{(\phi_1 - \cdots - \phi_n) + (\lambda_1 - \cdots - \lambda_n)}{\left(\dfrac{\partial \phi_1}{\partial h} - \cdots - \dfrac{\partial \phi_n}{\partial h} \right) + \left(\dfrac{\partial \lambda_1}{\partial h} - \cdots - \dfrac{\partial \lambda_n}{\partial h} \right)}$$

(4-17)

The reconstruction algorithm can be then summarized as below:

Step 1.　Given n conjugate image points, i.e. (S_1, L_1), (S_2, L_2), ..., (S_n, L_n), set an initial value for h^* -which can be an average value for the area- and then calculate (ϕ_1, λ_1), (ϕ_2, λ_2), ..., (ϕ_n, λ_n) using Equation 4-10.

Step 2.　Using Equations 4-13 and 4-14, calculate f_i and $\dfrac{\partial f_i}{\partial h}$ for $i=5{:}8$ and then calculate $\dfrac{\partial \phi}{\partial h}$ and $\dfrac{\partial \lambda}{\partial h}$ from Equation 4-12 for all the n conjugate points.

Step 3.　Calculate the correction Δh from Equation 4-16 or Equation 4-17 and add Δh to h^* and update h^*.

Step 4.　Repeat Steps 1 to 3 and update h^* each time until maximum number of iterations is reached or $|\Delta h|$ becomes smaller than a specified threshold.

Step 5.　Use the final value of h^* from Step 4 with conjunction with image point coordinates (S_1, L_1), (S_2, L_2), ..., (S_n, L_n) and calculate object coordinates (ϕ_1, λ_1), (ϕ_2, λ_2), ..., (ϕ_n, λ_n) using Equation 4-10.

Step 6.　Use the average value of object coordinates as the corresponding coordinates of conjugate pairs as below:

$$\phi = \frac{\left(\phi_1 + \cdots + \phi_n\right)}{n} \text{ and } \lambda = \frac{\left(\lambda_1 + \cdots + \lambda_n\right)}{n}$$

The least-square solution described above may not be able to result in the best solution because it only allows one explicit least-square solution for Δh and therefore, discrepancies may occur in ϕ and/or λ (Tao and Hu, 2002). It is observed by (Tao and Hu, 2002) that a forward *RFM* provides more accurate results as it allows for simultaneous least-square adjustment for all three object-space coordinates. It is recommended that the results of the inverse *RFM* be used as an initial value for the forward *RFM* reconstruction. It also should be noted that most of the commercial high-resolution satellite imagery providers deliver their products with only forward *RFM*. In

order to work use the inverse *RFM* with these images, this model should be created from the forward *RFM* through a fitting process (as explained in Chapter 3).

4.3   3-D Reconstruction Using Single Images

The majority of the images that have been archived by high-resolution, commercial satellite data providers have been single images, i.e., only a small fraction of the high-resolution optical imagery has been adapted for stereo interpretation. Furthermore, from economic point of view, single satellite images are more affordable. These two factors, i.e., availability and cost, make single images more attractive to end users. In this section, the fundamentals of creating 3-D city models using single images supported by the generic satellite projection model is presented.

4.3.1   Approximate Image Acquisition Geometry

Approximate image acquisition geometry and satellite orientation can be described by a sensor's elevation and azimuth angles. A sensor's elevation (altitude) angle is the angle from the horizon up to the satellite. The projection of the sensor's line of sight to the area-of-interest (*AOI*) on the ground onto the horizontal plane measured clockwise from the North defines the sensor's azimuth as shown in Figure 4-2.

An alternative representation of elevation and azimuth angles on a polar coordinate system is shown in Figure 4-3. The elevation angle is shown in the radial direction with a maximum of 90° at the center of the polar coordinate system. The azimuth is given by the polar angle measured in a clockwise direction from the North axis and usually is presented as a value in the range of $[-\pi, \pi)$. Figure 4-3 shows the collection geometry of a satellite at elevation of 30° and azimuth of 37.5^o.

It should be noted that the satellite's elevation and azimuth angles are constant for a given image only when a frame camera is used. In the case of linear *CCD* array sensors (e.g. Pushbroom sensor on board of Quickbird), each scan line has different elevation and azimuth angles. These differences depend on the difference between scan and orbital velocity vectors.
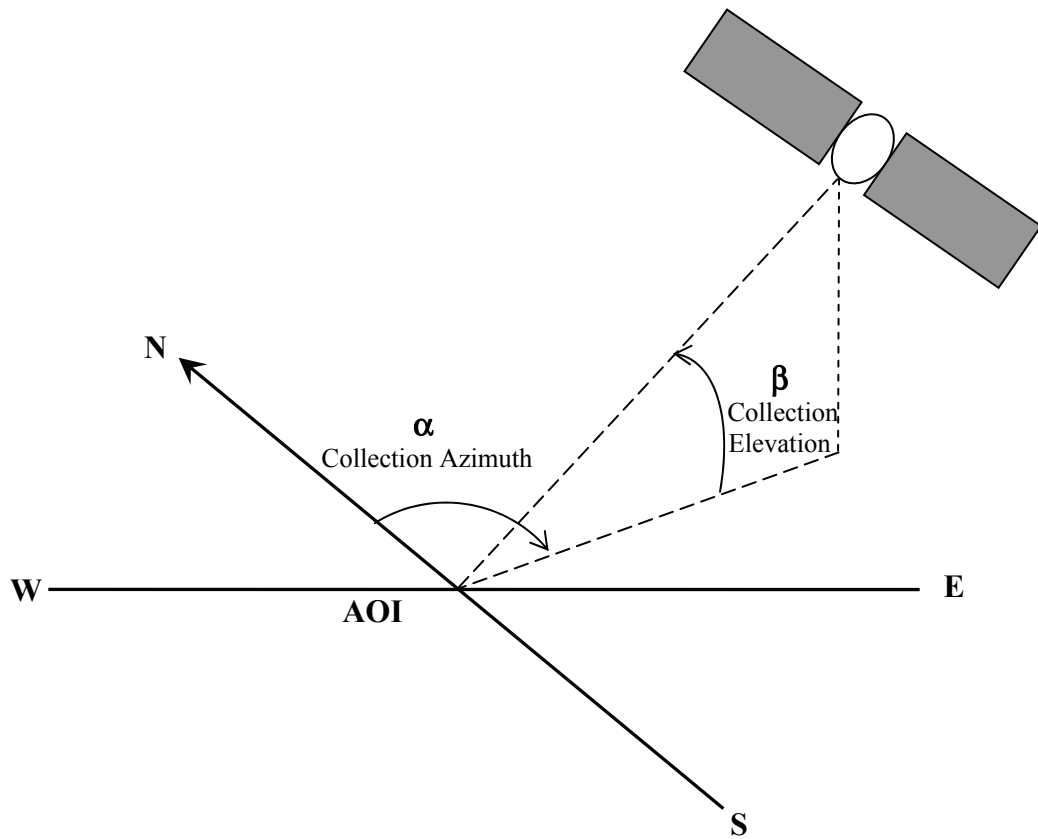
Figure 4-2 Approximate Image Acquisition Geometry, i.e., Sensor's Elevation and Azimuth
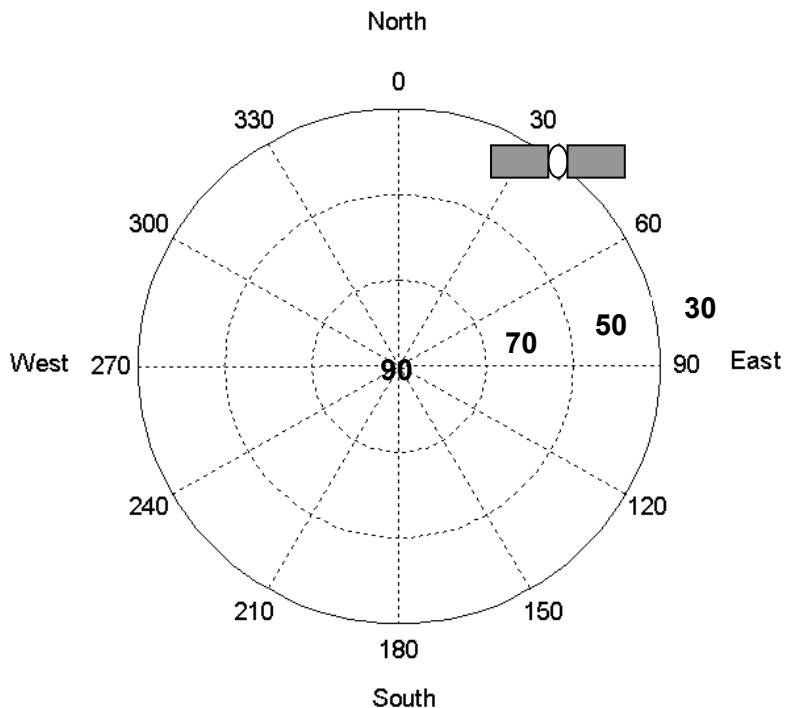
Figure 4-3 Image Acquisition Geometry in Polar Coordinate System
(Azimuth = 37.5^O, Elevation = 30°)

4.3.2   Height Methodology in Off-Nadir Images

Unlike nadir-looking images, in an oblique-angle image, the rooftops of buildings (man-made objects) do not appear at the same location as their bases. In off-nadir images, objects tend to lean outwards away from the imaging sensor. This is also known as "*relief displacement*" in off-nadir images meaning that is if a satellite views a scene from one direction, objects higher than bare-ground level appear to be slanted towards the opposite direction. In this section, two different methods for calculating the height of buildings from single images are introduced. The conventional method of measuring heights in single images is using shadows - wherever they are available - to estimate the height. An alternative method for calculating heights is by using sensor's orientation model as introduced here.

The orientation of the imaging plane on board an imaging platform can be grouped into two categories: *Type I*, which projects the underlying terrain into a plane perpendicular to the line of sight and *Type II* which projects the terrain into a horizontal plane. Figure 4-4 shows the *Type I* and *Type II* configurations. It should be noted that imagery providers may deliver each of their products in a different configuration. For instance, DigitalGlobe, Inc. delivers Quickbird images in three main packages: Basic, Standard and Ortho-rectified (Quickbird Imagery Product Guide, March 16, 2005). The projection plane in Basic imagery is *Type I* while Standard and Ortho-rectified images are *Type II*.

4.3.2.1 Measuring Height Using Sensor Orientation Model

To measure the height of an object using the sensor's orientation model, the collection azimuth (β) or the off-nadir viewing angle (θ), and the image plane configuration, i.e. *Type I* or *Type II* should be known. In a nadir-looking image ($\beta = 90^\circ$, $\theta = 0^\circ$), ground points representing the base of a building and their corresponding rooftop points appear at the same location on the image; however, in an oblique looking image, the rooftops are subjected to relief displacements and hence, appear at a different locations from their base. Orientation parameters in conjunction with image coordinates of base point of an object and its corresponding rooftop point can be utilized to calculate height of objects. Figure 4-5 shows the relief displacement in an oblique angle image of downtown San Diego, California, USA, acquired by OrbView on June 29, 2005.   In this figure, the satellite elevation is 69°, the satellite azimuth is 158.8°, the sun elevation is 70.7°

and the sun azimuth is 114.8°. It can be seen that the circled corners have the same longitude and latitude and the only difference is in their vertical coordinates, i.e. their elevation.
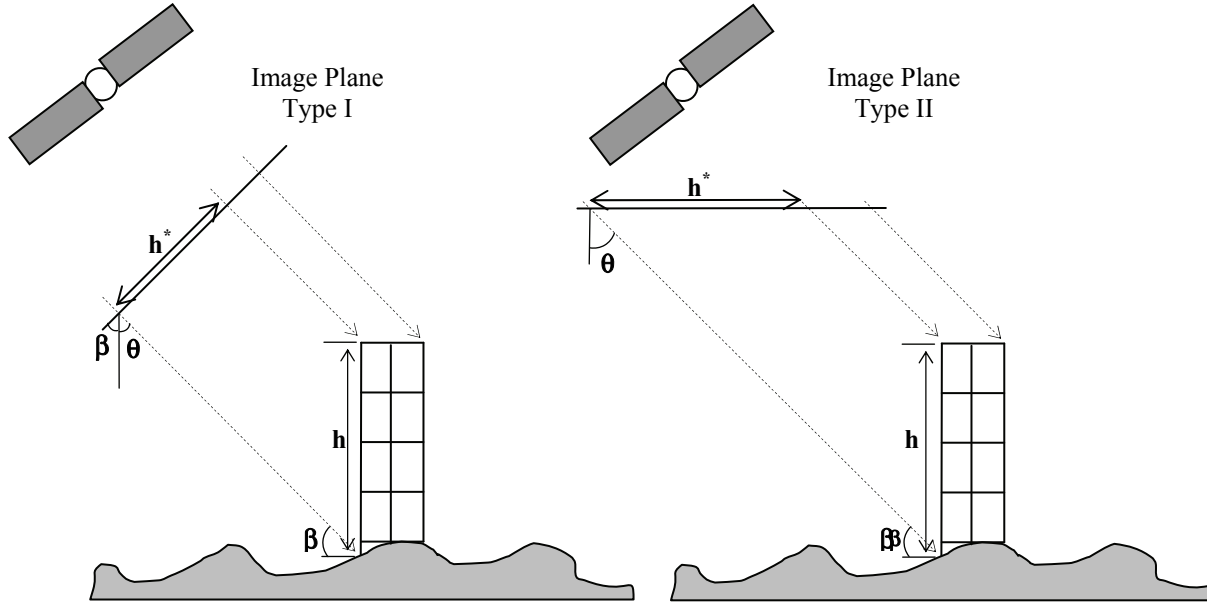
Figure 4-4 Type *I* and Type *II* Image Plane Configurations. Image Plane Type *I* is Perpendicular to the Line of Sight and is Known as Sensor-Projection Configuration. Image Plane Type *II* is Parallel to the Underlying Terrain and is Known as the Map-Projection Geometry.

Denoting the base coordinates, i.e., sample and line coordinates, of an object by (S_{base}, L_{base}) and its corresponding rooftop coordinates by ($S_{rooftop}$, $L_{rooftop}$), the height of an object between these two points can be calculated through the trigonometric relationship described in Equation 4-18.

$$h^* = GSD \times \sqrt{(S_{base} - S_{roof})^2 + (L_{base} - L_{roof})^2}$$

$$\begin{cases} h = \dfrac{h^*}{\cos(\beta)} = \dfrac{h^*}{\sin(\theta)} & \text{Image Plane : Type I} \\[3mm] h = h^* \tan(\beta) = \dfrac{h^*}{\tan(\theta)} & \text{Image Plane : Type II} \end{cases}$$

(4-18)

where *GSD* is the *ground sample distance* at elevation angle β or the viewing angle θ. *GSD* has the unit of feet/pixel (or meter/pixel); *h* is the physical height of the object in feet (or meter); and h^* is the measured height of a building from the image. (S_{base}, L_{base}) and ($S_{roptopf}$, $L_{rooftop}$) represent image coordinates, i.e., sample and line, of base-point and rooftop-point, respectively.
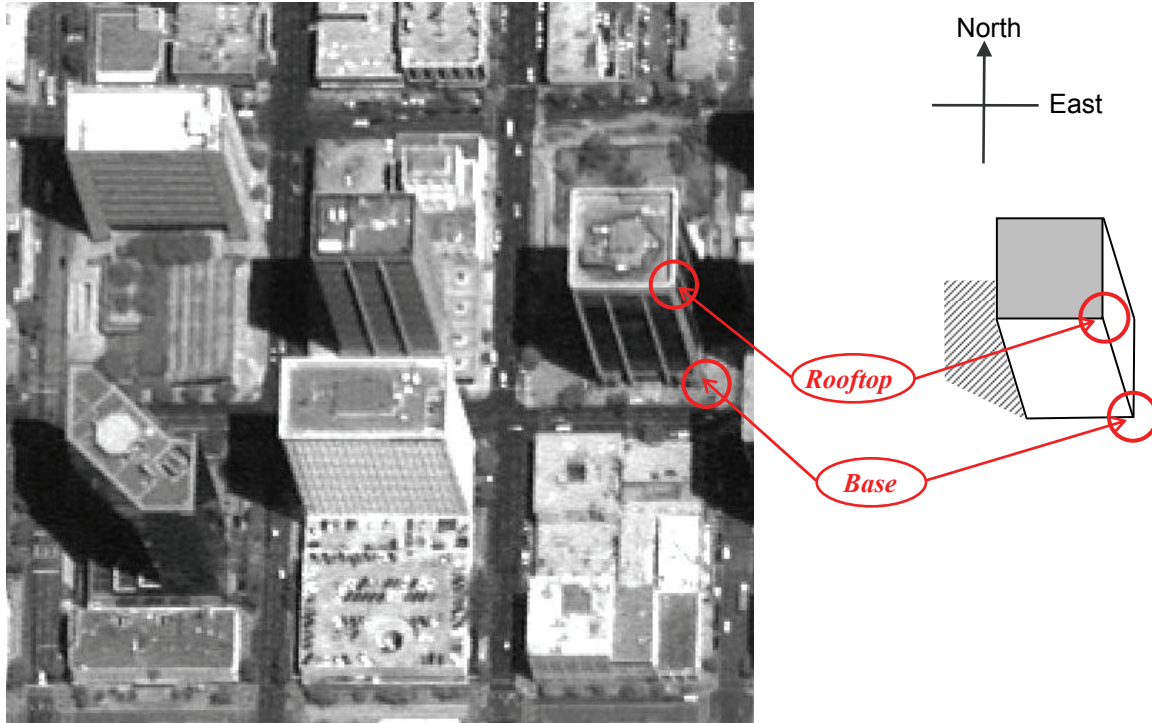
Figure 4-5 Relief Displacement of Rooftops in an OrbView Image of San Diego, CA, USA, Acquired on June 29, 2005. Base and Rooftop of Buildings Appear at Different Locations on this Image.

4.3.2.2 Measuring Heights Using Shadows

Shadows in single optical images can also be used to calculate the relative height of buildings from the terrain beneath them. Knowing the sun's position at the time of the image acquisition, i.e., sun's elevation (altitude) and azimuth, the differential height of objects can be calculated. The sun's elevation and azimuth can be calculated using the date and the time at which an image is acquired. Alternatively, this information can be retrieved from the metadata files supplied to the user by imagery providers. Figure 4-6 depicts the relationship between shadow length on the ground and the height of an object. Equation 4-19 shows the trigonometric relationship between shadow length and object's height.

$$h = l \tan(\beta_{sun}) = l \tan(Alt_{Sun}) \tag{4-19}$$

where h is the object's length, l is the shadow length and $_{sun}$ is the sun elevation (altitude) angle at the time image is acquired

48
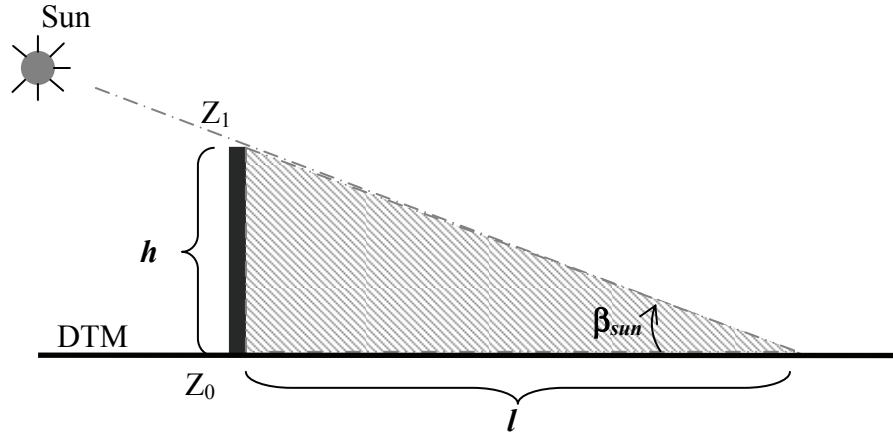
Figure 4-6 Geometric Relationships between Object Height and Shadow Length

Taking the configuration of the imaging plane (as shown in Figure 4-4) into account, the length of the shadow on the ground and its measured length on the image can be calculated as shown in Equation 4-20.

$$l^* = GSD \times \sqrt{\Delta s^2 + \Delta l^2}$$

$$\begin{cases} l = \dfrac{l^*}{\sin(\beta)} = \dfrac{l^*}{\cos(\theta)} & \text{Image Plane : Type I} \\ l = l^* & \text{Image Plane : Type II} \end{cases} \tag{4-20}$$

where Δs and Δl is the length of the shadow along the image's sample and the line direction, respectively, as shown in Figure 3.7. GSD is the *ground sample distance* at elevation angle β or the viewing angle θ. GSD has units of feet/pixel (or meters/pixels). l^* is the measured shadow length on the image (in pixels) and l is the shadow length on the ground (in feet or meters).

Assuming flat terrain condition, the azimuth angle of the sun can be used to calculate the length of the shadow in the horizontal plane as shown in Figure 4-7 and expressed by Equation 4-21.
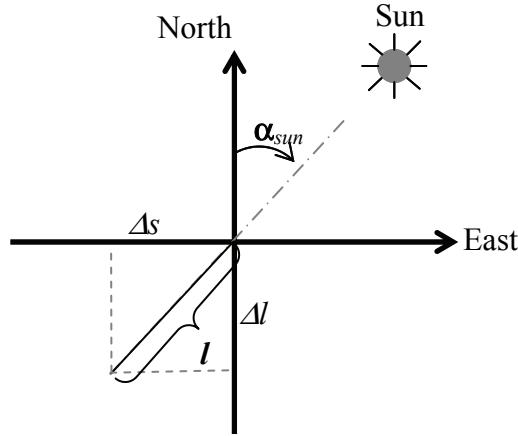
Figure 4-7 Relationship between Shadow Length and Azimuth Angle in Horizontal Plane

$$\Delta s = l\sin(\alpha_{sun}) = h \cdot \frac{\sin(\alpha_{sun})}{\tan(\beta_{sun})} = h \cdot \frac{\sin(Az_{sun})}{\tan(Alt_{sun})}$$

$$\Delta l = l\cos(\alpha_{sun}) = h \cdot \frac{\cos(\alpha_{sun})}{\tan(\beta_{sun})} = h \cdot \frac{\cos(Az_{sun})}{\tan(Alt_{sun})}$$

(4-21)

where ΔS and ΔL is the shadow length in feet (or meters) along the image's sample direction (North-South) and the image's line direction (West-East), respectively, h is object's height in feet (or meter). α_{sun} and β_{sun} are azimuth and elevation (altitude) angles of the sun at the time image is acquired respectively.

Equations 4-19 to 4-21 can be used to calculate the shadow length, corresponding object height as well as the azimuth angle (if not known). The prevalent problem using shadows to measure the height of objects is that in many cases – especially in dense urban areas – the shadows of adjacent buildings dilute the image such that it may be impossible to distinguish individual shadows. In other cases, small buildings are often masked within the shadows of tall buildings.

4.3.3 Height Measurement Error in Off-Nadir Images

The accuracy of height measurements from single (mono) images is significantly affected by two parameters; the off-nadir (θ) viewing angle of the satellite and the precision in selecting the base-point and its corresponding rooftop-point. Figure 4-8 shows the two different orientation

configurations that on-board satellite imagining systems have and the corresponding effect on height measurement errors.
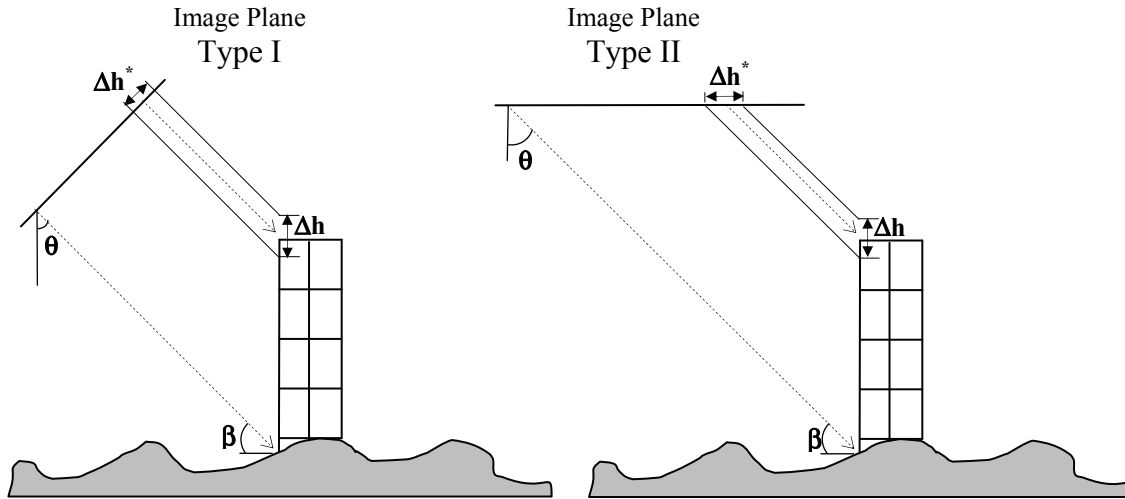
Figure 4-8 Height Measurement Errors in Single Images

Equation 4-22 expresses the relationship between the height measurement error and the corresponding pixel positioning error as well as the off-nadir viewing angle.

$$
\begin{cases}
\Delta h = \dfrac{\Delta h^*}{\sin(\theta)} = \sin^{-1}(\theta)\,\Delta h^* & \text{Image Plane : Type I} \\[3mm]
\Delta h = \dfrac{\Delta h^*}{\tan(\theta)} = \tan^{-1}(\theta)\,\Delta h^* & \text{Image Plane : Type II}
\end{cases}
\tag{4-22}
$$

where $\sin^{-1}(\theta)$ and , $\tan^{-1}(\theta)$ are the algebraic inverses of *sine* and *tangent* functions, respectively. θ is the off-nadir viewing angle, Δh and Δh^* are height measurement errors in the object space and in the image space due to positioning errors, respectively.

The pixel positioning error is an aleatory error which roots in the error involved in selecting base-points and their corresponding rooftop-points (done by using human selection). The effect of pixel positioning error can be minimized by calculating the direction in which the rooftop of a building is displaced in the image. This direction is called the *Principal Direction of Displacement* (*PDD*). Given the image coordinates of a selected point in an image, *PDD* is the locus of points in the image plane representing object points with the same longitude and latitude

but at different elevations. Therefore, the corrected image coordinates of the base-point are those projected on the *PDD* that pass through the rooftop-point as shown in Figure 4-9.
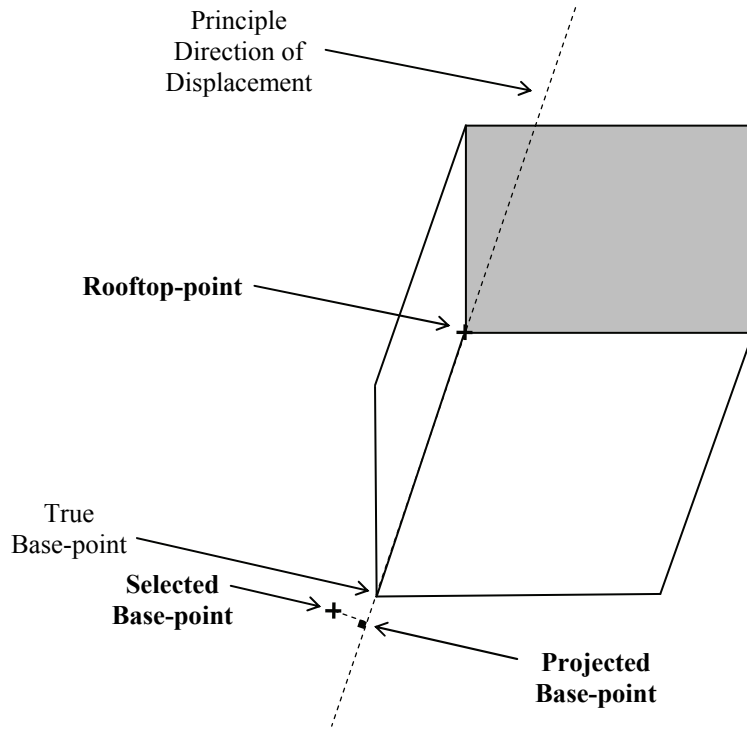
Figure 4-9 Geometric Correction Applied to the Selected Base-Point Coordinates

Applying the geometric correction, the user-induced error due to positioning at each end is reduced to Equation 4-23

$$\begin{cases} \Delta h = \sin^{-1}(\theta) \cdot [\text{GSD} \times \sigma_{\text{pixels}}] & \text{Image Plane : Type I} \\ \Delta h = \tan^{-1}(\theta) \cdot [\text{GSD} \times \sigma_{\text{pixels}}] & \text{Image Plane : Type II} \end{cases} \tag{4-23}$$

where *GSD* is the *ground sample distance* at a viewing angle θ, and σ_{pixels} is the maximum distance error in selecting points in an image in pixels.

Since there are positioning errors at both ends, i.e., roof-point and base-point, the total error in measuring a height can be calculated as shown below:

$$\begin{cases} \sigma_{\Delta h} = \sqrt{2} \cdot \sin^{-1}(\theta) \cdot [\text{GSD} \times \sigma_{\text{pixels}}] & \text{Image Plane : Type I} \\ \sigma_{\Delta h} = \sqrt{2} \cdot \tan^{-1}(\theta) \cdot [\text{GSD} \times \sigma_{\text{pixels}}] & \text{Image Plane : Type II} \end{cases} \tag{4-24}$$

where σ_h is the overall height error in feet (or meters).

Figure 4-10 shows the effect of the viewing angle θ on the overall height measurement accuracy for two orientation configurations, *Type I* and *Type II*. The calculated error in this figure is based on the average Quickbird *GSD* equal to 0.72 meters and is presented for three anticipated levels of positioning inaccuracies, i.e. one, two and three pixels.
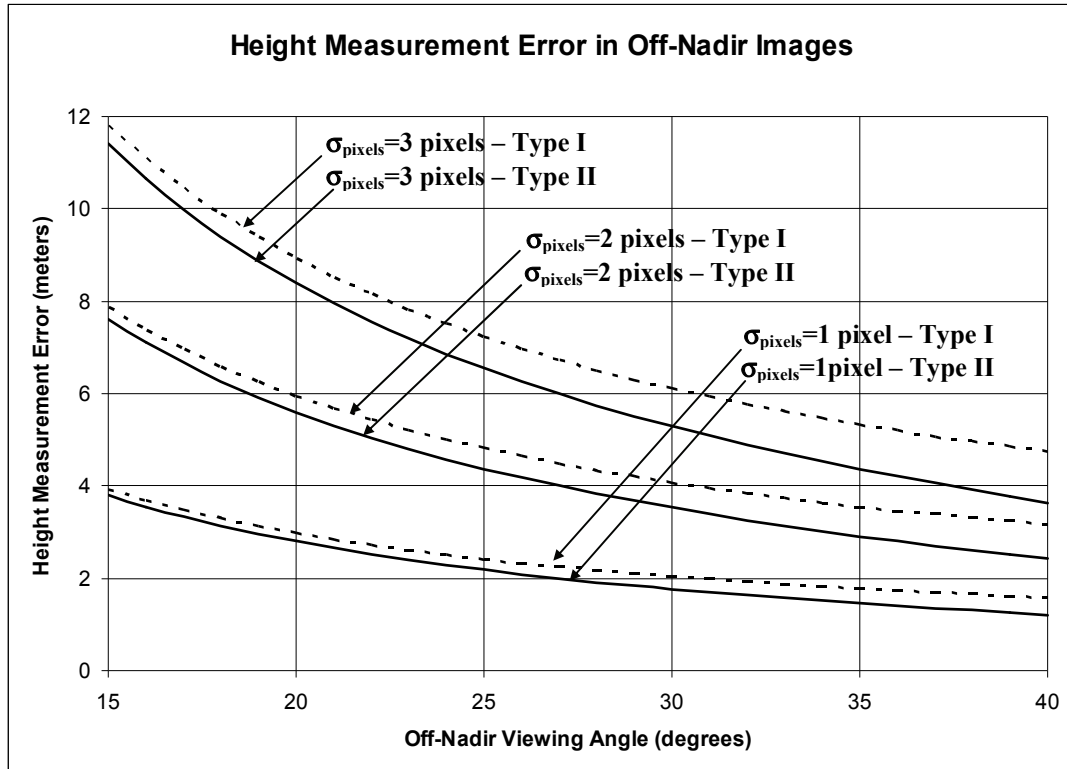
Figure 4-10 Viewing Angle Verses the Height Measurement Error at Different Positioning Inaccuracy Levels. Calculated for Quickbird Images with *GSD* = 0.72 Meters.

4.3.4   Reconstruction Algorithm

Reconstructing a 3-D scene using photogrammetry is a process in which spatial information associated with objects on the ground is extracted from 2D images. In the case of 3-D city modeling, the objects of interest are buildings and/or other structures such as bridges or critical infrastructure. Spatial attributes needed in order to reconstruct a scene include the longitude and latitude of the building, the height of the building above the ground, and the shape of the rooftop. In order to reconstruct a scene from a single off-nadir image, the coordinates of the base-points of a building, i.e. (S_{base}, L_{base}) and the corresponding rooftop-points, i.e., $(S_{rooftop}, L_{rooftop})$ should

first be selected using a semi-automated method, as explained in one of the earlier sections of this chapter. Employing the *RFM* as parameterized in Equation 4-1 to describe the object-to-image projection, each conjugate pair of base/rooftop pixels can be used to derive four nonlinear equations. Each conjugate pair refers to the same longitude and latitude on the ground; hence the total number of unknown parameters is reduced from six – that is, longitude, latitude, and height of the base-point and longitude, latitude, and height of the rooftop-point - to four parameters (a common longitude, a common latitude, height above the datum at the base-point and height above the datum at the rooftop level.) It can be shown that these four unknown parameters can be calculated by solving either of the following two nonlinear systems of equations: 1) A system of nonlinear homogeneous determined equations, or 2) A system of nonlinear homogeneous over-determined equations. The details of each will be presented in the following sections.

4.3.4.1 System of Nonlinear Homogeneous Determined Equations

Equation 4-25 shows a system of four nonlinear, homogeneous and determined equations and four unknowns. In these equations, polynomials f_i (*i=1:4*) are 20-term cubic polynomials as previously presented in Chapter 3 by Equation 3-16. The conjugate pair of pixels representing image coordinates of the base-point and the rooftop-point are shown as (S_{base}, L_{base}) and ($S_{rootopf}$, $L_{rooftop}$), respectively. The unknown parameters in the object-space are the longitude and the latitude (ϕ, λ) and height of the base-point and the rooftop-point above the reference ellipsoid (h_{base} and $h_{rooftop}$).

$$\begin{cases} \dfrac{f_1(\phi,\lambda,h_{base})}{f_2(\phi,\lambda,h_{base})} - S_{base} = 0 \\[2mm] \dfrac{f_3(\phi,\lambda,h_{base})}{f_4(\phi,\lambda,h_{base})} - L_{base} = 0 \\[2mm] \dfrac{f_1(\phi,\lambda,h_{rooftop})}{f_2(\phi,\lambda,h_{rooftop})} - S_{rooftop} = 0 \\[2mm] \dfrac{f_3(\phi,\lambda,h_{rooftop})}{f_4(\phi,\lambda,h_{rooftop})} - L_{rooftop} = 0 \end{cases} \qquad (4\text{-}25)$$

Equation 4-25 can be linearized about an initial point $x^* = (\phi^*, \lambda^*, h_{base}{}^*, h_{rooftop}{}^*)$ as explained by Equation 4-2. Partial derivatives then can be calculated as shown in Equations 4-3 and 4-4 and the result can be rewritten as the error equation presented in Equation 4-26.

$$
\begin{bmatrix} v_{S_{base}} \\ v_{L_{base}} \\ v_{S_{rooftop}} \\ v_{L_{rooftop}} \end{bmatrix} = \begin{bmatrix} \dfrac{\partial S_{base}}{\partial \phi} & \dfrac{\partial S_{base}}{\partial \lambda} & \dfrac{\partial S_{base}}{\partial h} & 0 \\ \dfrac{\partial L_{base}}{\partial \phi} & \dfrac{\partial L_{base}}{\partial \lambda} & \dfrac{\partial L_{base}}{\partial h} & 0 \\ \dfrac{\partial S_{rooftop}}{\partial \phi} & \dfrac{\partial S_{rooftop}}{\partial \lambda} & 0 & \dfrac{\partial S_{rooftop}}{\partial h} \\ \dfrac{\partial L_{rooftop}}{\partial \phi} & \dfrac{\partial L_{rooftop}}{\partial \lambda} & 0 & \dfrac{\partial L_{rooftop}}{\partial h} \end{bmatrix} \cdot \begin{bmatrix} \Delta \phi \\ \Delta \lambda \\ \Delta h_{base} \\ \Delta h_{rooftop} \end{bmatrix}
$$

$$
- \begin{bmatrix} S_{base} - S_{base}(\phi^*, \lambda^*, h_{base}{}^*) \\ L_{base} - L_{base}(\phi^*, \lambda^*, h_{base}{}^*) \\ S_{rooftop} - S_{rooftop}(\phi^*, \lambda^*, h_{rooftop}{}^*) \\ L_{rooftop} - L_{rooftop}(\phi^*, \lambda^*, h_{rooftop}{}^*) \end{bmatrix}
$$

(4-26)

which also can be shown as:

$$ v = A \cdot \Delta x - l \tag{4-27} $$

In this Equation, A is a 4 by 4 nonsingular design matrix, Δx is the unknown vector of corrections to approximate values of object-space coordinates and l is the vector of misclosures. v is the vector or residuals. The unknown object-space coordinates ϕ, λ, h_{base} and $h_{rooftop}$ can be solved iteratively by calculating the correction vector Δx as shown in Equation 4-28:

$$ \Delta x = A^{-1}l \tag{4-28} $$

At each iteration step, the vector of approximate object coordinates, i.e., x^*, is updated by $x^* + \Delta x$ and the mathematical model presented in Equation 3.25 is linearized again until convergence is obtained.

The reconstruction algorithm can be summarized as below:

Step 1.   Given a conjugate pair of base/rooftop points, i.e. (S_{base} , L_{base}) and ($S_{rootopf}$, $L_{rooftop}$), set an initial value for ϕ^*, λ^*, h_{base}^* and $h_{rooftop}^*$ - this can be an average value for the area or can be calculated using the truncated *RFM* considering only first order terms as explained in Section 4.3.4.3.

Step 2.   Using Equations 3-16 and 4-4, calculate f_i , $\dfrac{\partial f_i}{\partial \lambda}$, $\dfrac{\partial f_i}{\partial \phi}$ and $\dfrac{\partial f_i}{\partial h}$ for *i=1:4* at the initial point $x^* = (\phi^*, \lambda^*, h_{base}^*, h_{rooftop}^*)$ and then calculate $\dfrac{\partial S_j}{\partial \lambda}$, $\dfrac{\partial S_j}{\partial \phi}$, $\dfrac{\partial S_j}{\partial h}$, $\dfrac{\partial L_j}{\partial \lambda}$, $\dfrac{\partial L_j}{\partial \phi}$ and $\dfrac{\partial L_j}{\partial h}$ for *j={base, rooftop}*, from Equation 4-3.

Step 3.   Calculate the correction vector Δx from Equation 4-28 and update the initial point x^* by replacing it with $x^* + \Delta x$.

Step 4.   Repeat Steps 1 to 3 and update x^* each time until maximum number of iterations is reached or $|\Delta x|$ becomes smaller than a specified threshold.

4.3.4.2 System of Nonlinear Homogeneous Over-Determined Equations

The measured differential height between the base-point of an object and its corresponding rooftop-point as is calculated by Equation 4-19 can be used to reduce the number of unknowns in Equation 4-25 from four to three. Denoting this differential height by h, height of the roof-point above the reference datum can be calculated as below:

$$h_{rooftop} = h + h_{base} \tag{4-29}$$

Hence the nonlinear, homogeneous and determined system of equations presented in Equation 4-25 can be turned into an over-determined system of equations with one less unknown as is given in Equation 4-30.

$$\begin{cases} \dfrac{f_1(\phi,\lambda,h_{base})}{f_2(\phi,\lambda,h_{base})} - S_{base} = 0 \\[2mm] \dfrac{f_3(\phi,\lambda,h_{base})}{f_4(\phi,\lambda,h_{base})} - L_{base} = 0 \\[2mm] \dfrac{f_1(\phi,\lambda,h+h_{base})}{f_2(\phi,\lambda,h+h_{base})} - S_{rooftop} = 0 \\[2mm] \dfrac{f_3(\phi,\lambda,h+h_{base})}{f_4(\phi,\lambda,h+h_{base})} - L_{rooftop} = 0 \end{cases} \tag{4-30}$$

This equation can be linearized about an initial point $x^* = (\phi^*,\ \lambda^*,\ h_{base}{}^*)$ as explained by Equation 4-2. Partial derivatives then can be calculated as shown in Equations 4-3 and 4-4 and the result can be rewritten as the error equation presented in Equation 4-31.

$$\begin{bmatrix} v_{S_{base}} \\ v_{L_{base}} \\ v_{S_{rooftop}} \\ v_{L_{rooftop}} \end{bmatrix} = \begin{bmatrix} \dfrac{\partial S_{base}}{\partial \phi} & \dfrac{\partial S_{base}}{\partial \lambda} & \dfrac{\partial S_{base}}{\partial h} \\[2mm] \dfrac{\partial L_{base}}{\partial \phi} & \dfrac{\partial L_{base}}{\partial \lambda} & \dfrac{\partial L_{base}}{\partial h} \\[2mm] \dfrac{\partial S_{rooftop}}{\partial \phi} & \dfrac{\partial S_{rooftop}}{\partial \lambda} & \dfrac{\partial S_{rooftop}}{\partial h} \\[2mm] \dfrac{\partial L_{rooftop}}{\partial \phi} & \dfrac{\partial L_{rooftop}}{\partial \lambda} & \dfrac{\partial L_{rooftop}}{\partial h} \end{bmatrix} \cdot \begin{bmatrix} \Delta\phi \\ \Delta\lambda \\ \Delta h_{base} \end{bmatrix}$$

$$- \begin{bmatrix} S_{base} - S_{base}(\phi^*,\lambda^*,h_{base}{}^*) \\ L_{base} - L_{base}(\phi^*,\lambda^*,h_{base}{}^*) \\ S_{rooftop} - S_{rooftop}(\phi^*,\lambda^*,h+h_{base}{}^*) \\ L_{rooftop} - L_{rooftop}(\phi^*,\lambda^*,h+h_{base}{}^*) \end{bmatrix} \tag{4-31}$$

which also can be shown as:

$$v = A \cdot \Delta x - l \tag{4-32}$$

In this Equation, A is a 4 by 3 design matrix, Δx is the unknown vector of corrections to approximate values of object-space coordinates and l is the vector of misclosures. It should be noted that the first two lines in the design matrix A and the misclosures vector l are evaluated at $x^* = (\phi^*,\ \lambda^*,\ h_{base}{}^*)$ and the last two lines in A and l are evaluated at $x^* = (\phi^*,\ \lambda^*,\ h+\ h_{base}{}^*)$. The unknown object-space coordinates, $\phi,\ \lambda,\ h_{base}$ can be calculated iteratively by minimizing the second Euclidian norm of the residual vector v as shown in Equation 4-33:

$$\min(\|v\|^2) \Rightarrow \Delta x = (A^T wA)^{-1} A^T wl \tag{4-33}$$

where w is the weight matrix for the image points also known as the *a priori* covariance matrix of the image points. More details about the weight matrix can be found in Grodecki et al. (2004). At each iteration step, the vector of approximate object coordinates, i.e., x^*, is replaced by $x^* + \Delta x$ and the mathematical model presented in Equation 4-30 is linearized again until convergence is obtained.

The reconstruction algorithm can be summarized as below:

Step 1. Given a conjugate pair of base/rooftop points, i.e. (S_{base} , L_{base}) and ($S_{rootopf}$, $L_{rooftop}$), set an initial value for ϕ^* , λ^* and h_{base}^* - this can be an average value for the area or can be calculated using the truncated *RFM* considering only first order terms as explained in Section 4.3.4.3.

Step 2. Using Equations 2-16 and 4-4, calculate f_i , $\dfrac{\partial f_i}{\partial \lambda}$, $\dfrac{\partial f_i}{\partial \phi}$ and $\dfrac{\partial f_i}{\partial h}$ for $i=1:4$ at the initial point $x^* = (\phi^*, \ \lambda^*, h_j^*)$ and then calculate $\dfrac{\partial S_j}{\partial \lambda}$, $\dfrac{\partial S_j}{\partial \phi}$, $\dfrac{\partial S_j}{\partial h}$, $\dfrac{\partial L_j}{\partial \lambda}$, $\dfrac{\partial L_j}{\partial \phi}$ and $\dfrac{\partial L_j}{\partial h}$ for $j=\{base, rooftop\}$, from Equation 4-3.

Step 3. Calculate the correction vector Δx from Equation 4-28 and update the initial point x^* by replacing it with $x^* + \Delta x$.

Step 4. Repeat Steps 1 to 3 and update x^* each time until maximum number of iterations is reached or $|\Delta x|$ becomes smaller than a specified threshold.

4.3.4.3 Initial Approximate Values for System of Nonlinear Equations

Initial approximate values for $x^* = (\phi^*, \lambda^*, h_{base}^*, h_{rooftop}^*)$ can be calculated using the truncated *RFM* by only considering the first-order terms. Using the normalization parameters introduced in Equation 3-17, the linearized model can be expressed as:

$$X = \frac{S - S_0}{S_s} = \frac{a_1' + a_2'\lambda^* + a_3'\phi^* + a_4'h^*}{b_1' + b_2'\lambda^* + b_3'\phi^* + b_4'h^*} + \varepsilon_X$$

$$Y = \frac{L - L_0}{L_s} = \frac{c_1' + c_2'\lambda^* + c_3'\phi^* + c_4'h^*}{d_1' + d_2'\lambda^* + d_3'\phi^* + d_4'h^*} + \varepsilon_Y$$

(4-34)

where:

$$a_1' = a_1\phi_s\lambda_s h_s - a_2\phi_s\lambda^* h_s - a_3\phi^*\lambda_s h_s - a_4\phi_s\lambda_s h^* ,$$

$$a_2' = a_2\phi_s h_s , a_3' = a_3\lambda_s h_s , a_4' = a_4\lambda_s\phi_s ,$$

$$b_1' = \phi_s\lambda_s h_s - b_2\phi_s\lambda^* h_s - b_3\phi^*\lambda_s h_s - b_4\phi_s\lambda_s h^* ,$$

$$b_2' = b_2\phi_s h_s , b_3' = b_3\lambda_s h_s , b_4' = b_4\lambda_s\phi_s$$

and ϕ_s, λ_s, h_s, S_s, L_s are the latitude, longitude, height, sample and line scale factors, respectively.

Therefore, object-space coordinates of the initial point for a conjugate pair of base/rooftop points can be calculated using least-square solution presented below:

$$Ax^* = b \implies x^* = (A^T A)^{-1} A^T b$$

(4-35)

where

$$A = \begin{bmatrix} a_3' - X_{base}b' & a_2' - X_{base}b' & a_4' - X_{base}b_4' & 0 \\ c_3' - X_{base}d_3' & c_2' - X_{base}d_2' & c_4' - X_{base}d' & 0 \\ a_3' - X_{rooftop}b_3' & a_2' - X_{rooftop}b' & 0 & a_4' - X_{rooftop}b_4' \\ c_3' - X_{rooftop}d' & c_2' - X_{rooftop}d' & 0 & c_4' - X_{rooftop}d_4' \end{bmatrix},$$

$$b = -\begin{bmatrix} a_1' - X_{base}b' \\ c_1' - X_{base}d' \\ a_1' - X_{rooftop}b_1' \\ c_1' - X_{rooftop}d' \end{bmatrix}, x^* = \begin{bmatrix} \phi^* \\ \lambda^* \\ h_{base}^* \\ h_{rooftop}^* \end{bmatrix}, X_{base} = \frac{S_{base} - S_0}{S_s} \text{ and } Y_{rooftop} = \frac{L_{rooftop} - L_0}{L_s}$$

4.3.5 Height Extraction Accuracy Assessment

A Quickbird image of the city of London, UK acquired on July 28, 2002 at a 23.4° off-nadir viewing angle is used in this study to assess height extraction accuracy of the algorithm formulated in previous sections.   The study area extent spans Longitude W-0°4'00'' to

Longitude W-0°6'30'', and Latitude N-51°29''48'' to N-51°30'49''.   Figure 4-11 shows an aerial photo of the city of London. Figure 4-12 shows the 3-D city model created for the city of London using the Quickbird image (Basis level 1B product). The algorithm proposed in Section 3.3.4 was used in the construction of this example.

To assess the height accuracy of the proposed 3-D reconstruction algorithm, twenty-three randomly-selected buildings are considered and their heights are compared to independent survey data. Table 4-1 summarizes the result of the height extraction algorithm developed in this study verses data from the independent survey. The error shown in last column of Table 4-1 is calculated using Equation 4-36.

$$\varepsilon = \frac{\left|H_{Ind} - H_{Calc}\right|}{H_{Ind}} \times 100 \tag{4-36}$$

where H_{Ind} is the independent height from survey data and H_{Clac} is the calculated height from the algorithm.

Figure 4-11 Aerial Photo of City of London
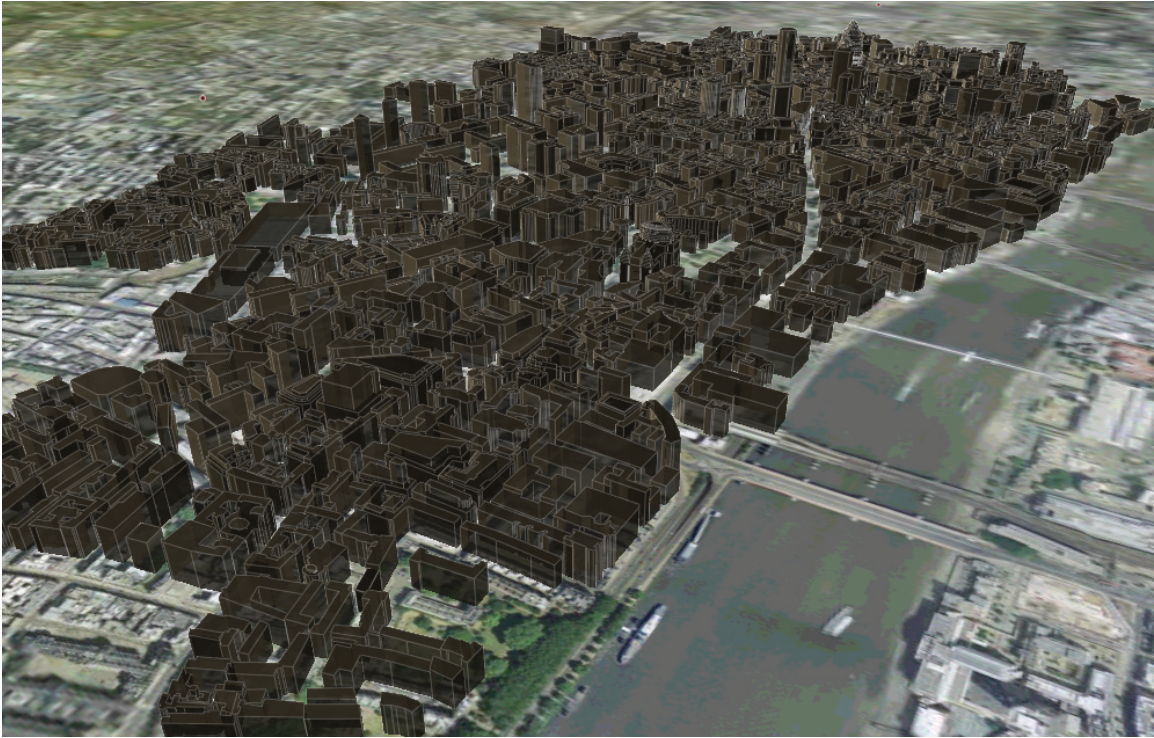
Figure 4-12 3-D City Model of the City of London, UK, Created Using the Algorithm Proposed in Section 4.3.4 and Single Quickbird Image Acquired on July 28, 2002 at 23.4° Off-Nadir Viewing Angle

As it can be seen from Table 4-1, the average calculated height error is less than 1.5%. The *RMS* error in the height calculation can also be computed as 1.7 meters or 5 feet which is equivalent of half a story (using typical story height of 10 feet).

Table 4-1 Summary of Height Accuracy Assessment for Twenty-Three Randomly Selected Buildings in the City of London, UK

Bldg. ID	Building Name	Independent Height (m)	Reconstructed Height (m)	Height Difference (m)	% Error
1	Plantation Place	68	68	0	0.00%
2	2 Minster Court	65	68	-3	4.62%
3	1 Minster Court	74	74	0	0.00%
4	20 Fenchurch St	91	94	-3	3.30%
5	1 America Sq, Cross Wall	67	69	-2	2.99%
6	Aviva Tower, Undershaft	118	119	-1	0.85%
7	Petticoat Tower	68	69	-1	1.47%
8	99 Bishopsgate	104	104	0	0.00%
9	10 Exchange sq	55	54	1	1.82%
10	Bishops gate exchange	60	58	2	3.33%
11	Exchange House, Exchange Sq	65	64	1	1.54%

12	Cromwell tower (Barbican)	123	125	-2	1.63%
13	St. Alphage House, Forest	69	69	0	0.00%
14	Shakespeare tower (Barbican)	123	125	-2	1.63%
15	Lauderdale Tower (Barbican)	123	123	0	0.00%
16	125 London Wall	82	81	1	1.22%
17	Citypoint	127	127	0	0.00%
18	Drapers Gardens	100	96	4	4.00%
19	City Tower Basinghall St.	69	69	0	0.00%
20	1 Angel Court	94	97	-3	3.19%
21	St. Paul's Cathedral	111	111	0	0.00%
22	Tower 42	183	185	-2	1.09%
23	Stock Exchange	100	100	0	0.00%
Average Error					**1.42%**

4.4   Topological Attributes

The building configuration in plan view, i.e., plan irregularities, is one of the contributing factors to the amount of damage a building experiences after a seismic event. Most vulnerability or fragility models require some configuration information; irregular buildings with reentrant corners behave differently from symmetric structures when subjected to strong ground motion excitations. Plan irregularities causing torsion are especially common among corner buildings in which the two adjacent street-side faces of the building are covered with windows and are open, whereas the other two sides are generally very solid. Furthermore, damage at connections significantly reduces the capacity of the vertical load resistant elements contributing to greater possible damages (FEMA154, 2002). Buildings with reentrant corners include but are not limited to those with long wings or wedged-shaped configurations such as **E**, **L**, **T**, **U**, **V** or **+** shaped structures. Figure 4-13 shows some examples of plan irregularities and possible locations of damage in a seismic event.

L-Shaped   U-Shaped   T-Shaped

Large Opening   Weak Link between Wings   V-Shaped
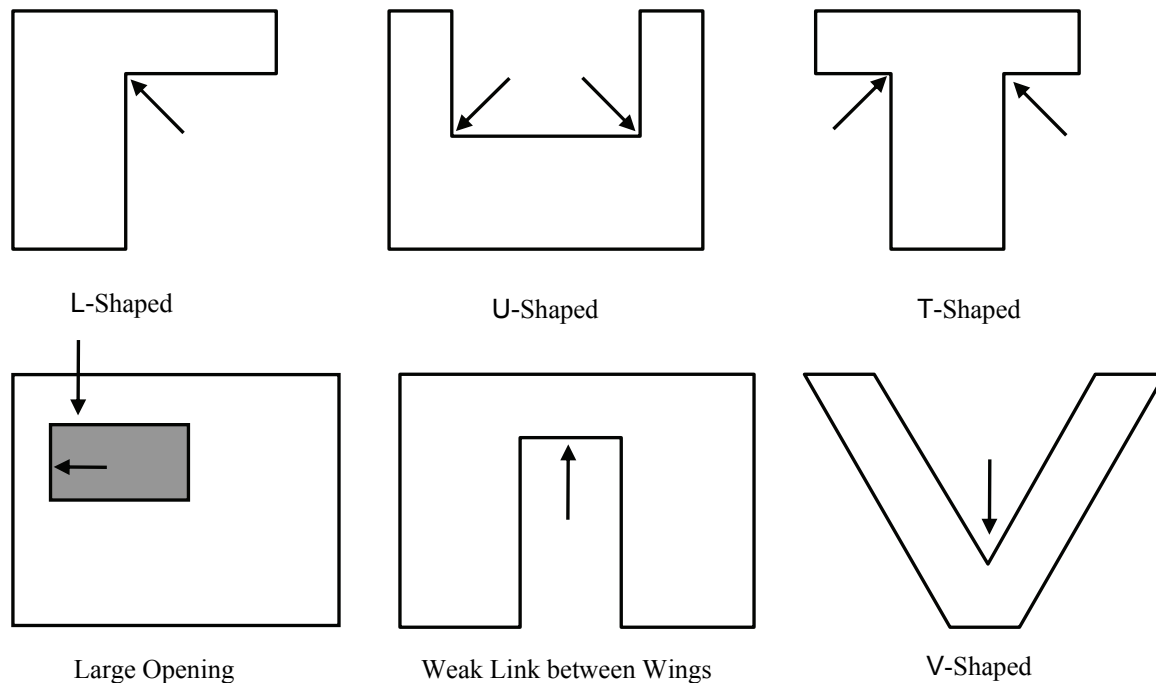
Figure 4-13 Plan Irregularities in Buildings with Reentrant Corners; Arrows Indicate Possible Areas of Damage (Source: FEMA154, 2002)

Topological shape attributes are properties of a geometric shape that remain invariant under elastic deformations, in the other words; they remain unaltered under stretching, translation or rotation of the image plane (Pratt, 2007). Hence, topological descriptors can be used to categorize irregularly shaped objects within a scene. Bounding polygons resulted from the digitization process in which rooftop of structures are delineated, can be used to calculate footprint area (*A*) and perimeter (*P*) of buildings at the rooftop level. Footprint area and perimeter of buildings can then be used to develop various geometric attributes of objects. Topological shape attributes with which configuration of buildings in the plan view can be described are explained in the rest of this section.

4.4.1   Slenderness Index

The most common shape descriptor based on area and perimeter of an object is a measure of thinness called *Thinness Ratio* (Duda et. a1, 2000) or *Circularity* (Pratt, 2007). Equation 4-37 presents the definition of the thinness ratio.

$$TR = 4\pi \frac{A}{P^2} \qquad\qquad (4\text{-}37)$$

where A is the area of an object and P is the perimeter. Hence, TR is dimensionless.

The *thinness ratio* reaches its maximum of 1 if the object is a circle. Similarly, from all possible triangles, the equilateral triangle has maximum TR of $\pi\sqrt{3}/9$ and from all quadrilaterals; the square has maximum TR of $\pi/4$. Loosely speaking, the fatter a shape is, the closer its TR is to one and the more line-like an object is, the closer its thinness ratio is to zero (Sanz, et. al, 2005). Since most buildings have noncircular configurations, it is reasonable to modify the thinness ratio such that it measures the rectangularity of objects, i.e., slenderness, instead of circularity. *Slenderness* is measured by the parameter α defined as a function of the ratio between perimeter P of an object and its area A. Equation 4-38 shows the definition of slenderness derived from evaluating the ratio between the perimeter and the area of an equivalent rectangular with α as the ratio between the two sides as shown in Figure 4-14. The derivation of Equation 4-38 can be found in Appendix A

$$\alpha = \begin{cases} \lambda & \text{for } \lambda \le 1 \\ 2\lambda - 1 + 2\sqrt{\lambda(\lambda-1)} & \text{for } \lambda > 1 \end{cases}$$
$$\text{where } \lambda = \frac{P^2}{16A} \qquad\qquad (4\text{-}38)$$

$\alpha = 1$ is the slenderness of a square shaped object. Values of $\alpha < 1$ refer to convex shapes with a minimum of $\alpha = \pi/4$ (0.78) in the case of a circular shaped object. Values of $\alpha > 1$ refer to rectangular-shaped objects and other elongated shapes. It can be seen that α is a geometric descriptor of the shape representing slenderness of an object as an equivalent rectangle.

l

$\alpha.l$
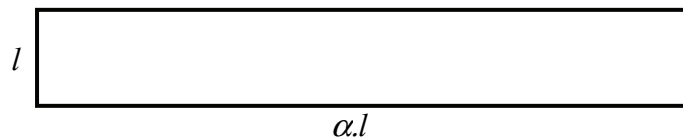
Figure 4-14 Equivalent Rectangle with α as the Ratio Between the Two Sides

4.4.2 Convexity Index

The *convexity index* can be calculated as the ratio between the area within the circumscribed convex polygon of an object and the area of the object itself as shown in Equation 4-39. The convexity index of convex shapes is one. Any other shape such as **L**, **T**, **U** or **V** will have a convexity index larger than one.

$$C_I = \frac{A_C}{A}$$

(4-39)

where A_C is the area of the circumscribed convex polygon and A is the area of the rooftop.

4.4.3 Irregularity Index

The footprint (or plan view) irregularity of buildings can be calculated using the convexity index as measured from Equation 4-39, which is normalized by an equivalent convexity index calculated for an object with similar slenderness to generate a measure of irregularity, invariant from the slenderness. Denoting the irregularity index by *IR*, this index can be calculated as shown in Equation 4-40.

$$IR = \begin{cases} 0 & \text{for } C_{eq} = 1 \\ \dfrac{C_I - 1}{C_{eq} - 1} & \text{for } C_{eq} \neq 1 \end{cases}$$

(4-40)

where C_I is the convexity index of the rooftop calculated from Equation 4-39. C_{eq} is the equivalent convexity index. The equivalent convexity index calculated for an L-shaped building with slenderness α as the ratio between its sides as shown in Figure 4-15 is presented in Equation 4-41. The derivation of Equation 4-41 can be found in Sarabandi (2007) as well as Appendix A.

$$C_{eq} = \frac{\alpha^2 + 6\alpha + 1}{8\alpha}$$

(4-41)
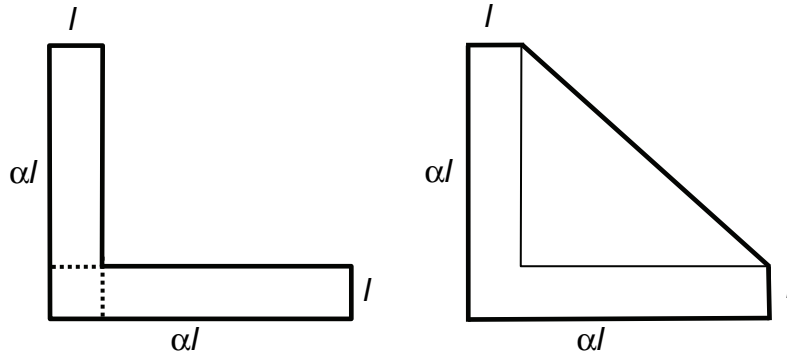
Figure 4-15 Circumscribed Convex Polygon for an L-Shaped Footprint

Similarly, the equivalent convexity index calculated for a U-shaped building with a slenderness value of α (he ratio between its sides as shown in Figure 4-16 is presented in Equation 4-42. The derivation of Equation 4-42 can be found in Sarabandi (2007) as well as Appendix A.
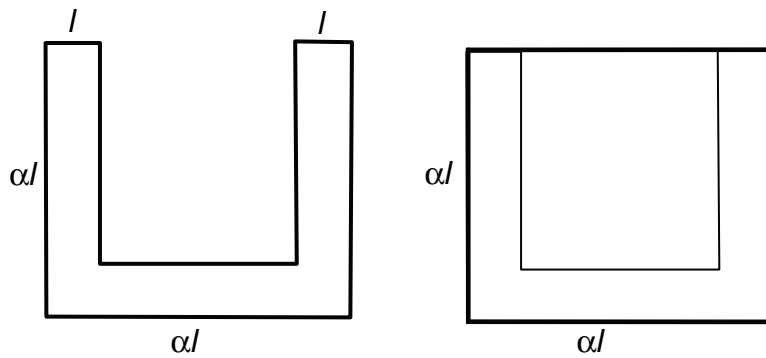
Figure 4-16 Circumscribed Convex Polygon for a U-Shaped Footprint

$$C_{eq} = \frac{\alpha^2 + 2\alpha + 1}{9\alpha} \tag{4-42}$$

SECTION 5
INFERENCING BUILDING INVENTORY ATTRUBUTES USING STATISTICAL MODELS

5.1   Overview

Information extracted from remotely sensed data while creating 3-D models of urban areas is usually limited to spatial, spectral or geometric attributes of buildings. Spatial information includes, but is not limited to, attributes such as location of structures, i.e. longitude and latitude, proximity of structures and topography of the region.   Spectral information contains attributes such as rooftop material, cladding or façade material, and etc.   Geometric attributes provide information about height of structures, footprint area and perimeter of structures, degree of irregularity in plan view and elevation, dominant orientation of buildings in city blocks, roof types (flat, gable, hip and etc.) and other indices which can be derived form the geometry of objects.   There is, however, another set of attributes, important in assessing vulnerability of structures subjected to natural or man-made disasters, which cannot directly be derived from remotely sensed data.   Structural type, occupancy type and age of structures are among those attributes.   Structural type is determined by the load resisting system (vertical and lateral) used in a structure.   Examples of structural type are classes such as wood, steel, concrete and masonry structures.   Occupancy type is defined as the social-use or the utility-class of structures. Examples of occupancy type include classes such as residential, commercial and industrial.

In this chapter, a methodology for inferring structural type and occupancy type of buildings from other signatures and attributes of an urban area such as the ones that can be derived from imagery is formulated.   Since the response variables to be modeled, i.e. structural type and occupancy type, as well as some of the independent variables such irregularity of buildings or roof type of structures are categorical data, the statistical model to be used for inferencing should incorporate a categorical data mining framework.   An overview of categorical data modeling is first presented in this chapter.   The methodology is then applied to different datasets to illustrate the application of statistical pattern recognition techniques in structural attribute modeling.

5.2   Methodology

In order to perform an inclusive vulnerability assessment of an urban area, subjected to different hazard scenarios (natural or man-made), a comprehensive inventory of structures at risk is

needed. Attributes included in such building inventories usually consist of a mixture of classes. There are attributes with a well-defined measurement scale such as height, square footage, perimeter and age of structures that are categorized as *quantitative variables*. There are also attributes such as structural type or occupancy type of buildings which do not have any natural measurement scale and are defined based on a set of levels or classes. These types of variables are known as *qualitative* or *categorical variables*. The input variables to a statistical model, i.e. observations, are known as *explanatory variables*, *independent variables* or *predictors*. These measurements are regarded as non-random measurements. The output(s) of statistical models are referred to as *response variables* or *dependent variables*. These are the outcome of models for a given set of observations (response variables) and are regarded as random variables which are free to vary in response to explanatory variables.

In order to infer the structural- and occupancy-type of buildings from geometric and spatial attributes of the built-environment, a statistical framework which incorporates both quantitative and qualitative variables should be utilized. In this report, application of *multinomial logistic regression models* in inferring categorical attributes of urban areas is investigated. Models developed in this report are then used to establish a set of inference rules using training datasets.

In *multinomial logistic regression models*, probability of a response variable, from the ith observation, falling into the kth category given a set of explanatory variables can be expressed by a multinomial probability distribution as shown below:

$$P(y_i = k \mid x_i) = \pi_k(x_i) = \pi_{ik}$$
$$i = 1 : N \ \ and \ \ k = 1 : K - 1 \tag{5-1}$$

where (x_i , y_i) is the ith observation such that $x_i = (x_{i1}, x_{i2}, \ldots, x_{ip})$ is a vector of p explanatory variables and y_i is the corresponding response variable. π_{ik} is the probability of ith response variable falling in the kth category.

It can be seen that for the ith observation, the response variable with K categories can be treated as a multinomial variable with probabilities $\{\pi_{i1}, \pi_{i2}, \ldots, \pi_{iK}\}$ and the constraint that $\sum_{k=1}^{K} \pi_{ik} = 1$. To impose the constraint that fitted probabilities on the K categories should sum to one, one of the categories should arbitrary be selected as the *base category* or the *control group*. This

category can be the first, the last or any other. Choosing the last category as the baseline category, the *log-odds* or "logarithm of the ratio between logit model of the kth category and the baseline category" for p explanatory variables can be expressed as shown in Equation 5-2.

$$\ln(\frac{\pi_{ik}}{\pi_{iK}}) = \sum_j \beta_{jk} x_{ij} = \alpha_k + \beta_{1k} x_{i1} + ... + \beta_{pk} x_{ip} \tag{5-2}$$

where α_k and β_{jk}'s are the logistic regression coefficients of the log-odds of the kth category relative to the base category.

Using Equation 5-2, probability of ith observation falling in the kth category can then be expressed as below:

$$\pi_{ik} = \frac{\exp(\sum_j \beta_{jk} x_{ij})}{1 + \sum_{k=1}^{K-1} \exp(\sum_j \beta_{jk} x_{ij})} \ ; \ i = 1 : N , j = i : p \tag{5-3}$$

and therefore $\pi_{iK} = 1 - \sum_{k=1}^{K-1} \pi_{ik}$ (5-4)

where π_{ik} is the probability of ith observation falling in the kth category.

Parameter estimation for log-odds of explanatory variables is done by maximizing the expectation of log-likelihood of each variable. For each log-odds, estimated parameters ($\hat{\beta}$) as well as their standard error ($\sigma_{\hat{\beta}}$) can be calculated. The significance of each parameter in the model can be assessed using the *Wlad statistics*. The *Z-value* of Wald statistics for each parameter can be calculated by computing the ratio of estimated parameters and their standard error term as shown in Equation 5-5.

$$Z = \frac{\hat{\beta}}{\sigma_{\hat{\beta}}} \sim N(0,1) \tag{5-5}$$

where Z is the Wald statistics of the estimated parameter $\hat{\beta}$. The standard error of parameter $\hat{\beta}$ is shown by $\sigma_{\hat{\beta}}$.

The computed *Z-value* has a normal distribution and can be used to judge the significance of the coefficient. It can be shown that for large sample sizes, Z^2 has a chi-square distribution with one degree of freedom. To judge the overall suitability and parsimony of a model, the *Akaike Information Criterion* (*AIC*) is used. In the context of logistic models presented in this report, the *AIC* can be defined as the sum of residual deviance of the model and the number of regression coefficients as shown in Equation 5-6.

$$AIC = -2L(\hat{\boldsymbol{\beta}}) + 2n \qquad\qquad (5\text{-}6)$$

where $L(\hat{\boldsymbol{\beta}})$ is the maximum log-likelihood of the fitted model and *n* denotes total number of variables in the model.

Smaller values of *AIC* indicate a better fit to the data. *AIC* can also be used as a comparison tool when it comes to model selection.

5.3   Datasets and Model Development

In this section, application of multinomial logistic regression model -explained in earlier parts of this report- are discussed. Two sets of data from southern California, USA are collected and used in this study. The first set of data, also referred to as *dataset A* in this report, is the aggregated tax assessor database of five counties in southern California originally developed for *EPEDAT,* (1994). This database contains structural and occupancy attributes of buildings as well as height, total square footage and year of construction of structures at the "census tract" level. The database contains total of 38,135 buildings from 1,570 census tracts from counties of Los Angeles, Orange, Riverside, San Bernardino and Ventura as well as aggregated inventory data of the city of Los Angeles, which was originally excluded from the Los Angeles county dataset. The second set of data used in this report, also referred to as *dataset B*, is the detailed inventory data of eighteen census tracts within the Orange county. The inventory database of Orange county is collected at the building level with attributes extracted from tax assessor database of the county as well as from remotely sensed imagery. In this dataset, structural type, occupancy type and year of construction of buildings are extracted from tax assessor databases while height, square footage, configuration in plan view as well as rooftop type of 1,947 buildings, are extracted from optical imagery.

In order to identify all the possible models that can be created using *dataset A*, the most primitive combination of attributes in this dataset, also known as the *baseline model*, should first be identified. Additional explanatory variables then will be added to the baseline model one at a time. The most basic model to be considered using *dataset A* is the one associated with only two explanatory variables; i.e. the height and square footage of buildings. This choice of variables is mainly because of the fact that height and footprint area of structures are the only two common attributes between *dataset A* and the ones that can directly be extracted from remotely sensed data when reconstructing 3-D city models. If additional information such as rooftop type, cladding, age of the buildings and etc. is available from auxiliary sources, it can be added to the model in the later stages. Finally, if either structural type or occupancy type of a building is known it is reasonable to include that attribute in the model in order to predict the other one. Therefore, for each of the response variables, i.e. structural type and occupancy type, three models can be created. Table 5-1 summarizes different models which can be created using *dataset A*, starting with a baseline model in each case. Supplementary explanatory variables are then added to the baseline model one at a time.

Table 5-1 Summary of Models Created from *Dataset A*

Model ID	Response Variable	Explanatory Variable Included in the Model			
		Variable #1	Variable #2	Variable #3	Variable #4
Model I[*]	General Str. Type	Height (ft)	Ave. Area (ft^2)	-	-
Model II	General Str. Type	Height (ft)	Ave. Area (ft^2)	General Occ. Type	-
Model III	General Str. Type	Height (ft)	Ave. Area (ft^2)	General Occ. Type	Age
Model IV[*]	General Occ. Type	Height (ft)	Ave. Area (ft^2)	-	-
Model V	General Occ. Type	Height (ft)	Ave. Area (ft^2)	General Str. Type	-
Model VI	General Occ. Type	Height (ft)	Ave. Area (ft^2)	General Str. Type	Age

[*] Baseline model

In case of *dataset B*, both tax assessor files and remotely sensed imagery are used to compile the dataset, therefore this dataset has larger number of attributes associated with each building compare to *dataset A*. There are seven attributes associated with each observation. These are height, square footage, irregularity, rooftop type, year of construction, structural type and occupancy type. Following the argument made for *dataset A* regarding creating a baseline model upon the most primitive attributes which can directly be extracted from remotely sensed data and then adding more attributes to the model, it is reasonable to include the following attributes in

the prime model of *dataset B*: height, square footage, irregularity and rooftop type. Depending on the availability of ancillary data, year of construction or age of buildings, occupancy type or structural type can be included in the model in the later steps. Table 5-2 summarizes different models which can be created using *dataset B*

Table 5-2 Summary of Models Created from *Dataset B*

Model ID	Response Variable	Explanatory Variable Included in the Model					
		Variable #1	Variable #2	Variable #3	Variable #4	Variable #5	Variable #6
Model I[*]	Str. Type	Height (ft)	Area (ft^2)	Configuration	-	-	-
Model II	Str. Type	Height (ft)	Area (ft^2)	Configuration	Roof	-	-
Model III	Str. Type	Height (ft)	Area (ft^2)	Configuration	Roof	Occ. Type	-
Model IV	Str. Type	Height (ft)	Area (ft^2)	Configuration	Roof	Occ. Type	Age
Model V[*]	Occ. Type	Height (ft)	Area (ft^2)	Configuration	-	-	-
Model VI	Occ. Type	Height (ft)	Area (ft^2)	Configuration	Roof	-	-
Model VII	Occ. Type	Height (ft)	Area (ft^2)	Configuration	Roof	Str. Type	-
Model VIII	Occ. Type	Height (ft)	Area (ft^2)	Configuration	Roof	Str. Type	Age

[*] Baseline Model

Datasets *A* and *B* are used to compute the parameters of multinomial logistic models, fitted to each set of variables defined in Tables 5-1 and 5-2. In order to calculate the overall classification error of a multinomial logistic model, the corresponding classification table for the response variable using prediction rules defined by the model should be calculated. The diagonal elements of this table represent the number of correctly classified observations. Classification error can then be calculated by computing the ratio between sum of the diagonal elements of the table and total number of elements in the table as shown in Equation 10.

$$\varepsilon = 1 - \frac{sum[diag(T)]}{sum[T]} \tag{5-7}$$

where ε is the classification error or misclassification rate, in table *T* and *diag(.)* refers to the diagonal elements of the table.

Examples of classification tables for *Model I* through *Model III* of *dataset A* (in Table 5-1) are shown in Tables 5-3 through 5-5, respectively. A summary of the *AIC*, the degrees of freedom *df*, for estimating parameters of each model and the overall classification error of each of the models is presented in Tables 5-6 and 5-7, respectively.

Table 5-3 Classification Table for Structural Classes Using *Mode I* of Table 5-1

		Predicted Structural Classes					
		C	C/S	RM	S	URM	W
Observed Structural Classes	C	**1590**	0	0	128	0	7575
	C/S	45	**0**	0	1	0	440
	RM	349	0	**0**	13	0	2842
	S	542	0	0	**149**	0	437
	URM	325	0	0	5	**0**	3151
	W	685	0	0	6	0	**16505**

Table 5-4 Classification Table for Structural Classes Using *Mode II* of Table 5-1

		Predicted Structural Classes					
		C	C/S	RM	S	URM	W
Observed Structural Classes	C	**3917**	0	33	145	0	5198
	C/S	151	**0**	0	0	0	335
	RM	380	0	**48**	38	0	2738
	S	490	0	42	**186**	0	410
	URM	869	0	16	6	**0**	2590
	W	1333	0	49	41	0	**15773**

Table 5-5 Classification Table for Structural Classes Using *Mode III* of Table 5-1

		Predicted Structural Classes					
		C	C/S	RM	S	URM	W
Observed Structural Classes	C	**6652**	0	60	164	12	2405
	C/S	401	**0**	7	0	0	78
	RM	715	0	**142**	0	0	2347
	S	704	0	0	**424**	0	0
	URM	1710	0	43	0	**0**	1728
	W	2484	0	122	0	0	**14590**

Table 5-6 Summary of *AIC,* Degrees of Freedom (*df*) and the Overall Classification Error of Models in Table 5-1 Used in Building the Multinomial Logistic Regression Models from D*ataset A*

Model ID	Response Variable	Explanatory Variable				AIC	df	Classification Error
		#1	#2	#3	#4			
Model I[*]	Str. Type	Height (ft)	Area (ft^2)	-	-	87,133	20	47.56%
Model II	Str. Type	Height (ft)	Area (ft^2)	Occ. Type	-	77,450	50	42.73%
Model III	Str. Type	Height (ft)	Area (ft^2)	Occ. Type	Age	58,285	60	37.31%
Model IV[*]	Occ. Type	Height (ft)	Area (ft^2)	-	-	91,825	24	51.14%
Model V	Occ. Type	Height (ft)	Area (ft^2)	Str. Type	-	81,894	54	46.44%
Model VI	Occ. Type	Height (ft)	Area (ft^2)	Str. Type	Age	81,608	66	46.69%

[*] Baseline model

Table 5-7 Summary of *AIC*, Degrees of Freedom (*df*) and the Overall Classification Error of Models Used in Building the Multinomial Logistic Regression Models from D*ataset B*

Model ID	Response Variable	Explanatory Variable						*AIC*	*df*	Classification Error
		#1	#2	#3	#4	#5	#6			
Model I*	Str. Type	H	A	Config.	-	-	-	3631	20	30.71%
Model II	Str. Type	H	A	Config.	Roof	-	-	2663	35	21.98%
Model III	Str. Type	H	A	Config.	Roof	Occ.	-	1827	50	17.36%
Model IV	Str. Type	H	A	Config.	Roof	Occ.	Age	1771	55	16.18%
Model V*	Occ. Type	H	A	Config.	-	-	-	3697	12	43.50%
Model VI	Occ. Type	H	A	Config.	Roof	-	-	2984	21	29.74%
Model VII	Occ. Type	H	A	Config.	Roof	Str.	-	2062	36	18.90%
Model VIII	Occ. Type	H	A	Config.	Roof	Str.	Age	2064	39	18.90%

* Baseline model

5.4   Results and Examples

The multinomial logistic model in each case can be used for classification purposes by defining a set of decision rules. For instance, for an input *attribute vector* -consisted of *p* independent values- to the model, i.e. $x = (x_1, x_2,…, x_p)$, probability of the response falling into each of the *K* categories can be computed as $\Pi = \{\pi_1, \pi_2,..., \pi_K\}$ using Equations 5-3 and 5-4. The category corresponding to the highest probability in Π can be selected as the class to which the input attribute vector belongs. Furthermore, a minimum probability threshold can be chosen such that if the highest probability in Π is below that threshold, the classification results in an "unclassified" status. In cases in which the probability difference between two classes is not significant, a tie assignment between class-membership will result and therefore, a set of rules to assign the response variable to the correct class should be defined. It should be noted that in many cases decision rules depend on the nature of the input variables to the mode as well the resulted response variable, and hence they differ from one problem to the other. Therefore, careful consideration should be given while compiling the decision rules for a specific problem.

Table 5-8 shows the result of parameter estimation for *Model I* from *dataset A*. The *base-category* (also known as *control group*) for explanatory variables in this table is the structural class type "*C*", i.e. the concrete class, and is highlighted by an asterisk.

Table 5-8 Log-Odds Parameters of *Model I* from *Dataset A* (Table 5-1)

Log-odds		Intercept	H[*] (High)	H (Medium)	H (Low)	Average Area
C/S	Coefficients	-2.216	-	-0.324	-0.572	-1.3E-05
	Std. Error	5.2E-11	-	5.3E-12	4.3E-11	2.2E-06
RM	Coefficients	-0.574	-	0.337	-0.355	-1.2E-05
	Std. Error	1.7E-11	-	2.7E-12	1.3E-11	8.3E-07
S	Coefficients	-1.154	-	-0.130	-1.502	8.4E-06
	Std. Error	5.3E-12	-	2.2E-12	2.6E-12	4.1E-07
URM	Coefficients	-0.401	-	0.382	-0.388	-1.7E-05
	Std. Error	2.5E-11	-	3.5E-12	2.0E-11	9.7E-07
W	Coefficients	-8.096	-	11.408	9.099	-4.9E-05
	Std. Error	3.6E-11	-	5.9E-12	3.1E-11	8.7E-07

[*] Base-category Variable

In order to assign a class to an independent observation, the probability vector Π should first be computed. The category corresponding to the highest probability in Π is then assigned to the observation. As an example let's assume the structural type of a low-rise building with average square footage of 2,176 ft^2 in southern California is to be predicted. Using the estimated parameters for the corresponding model, i.e. *Model I*, shown in Table 8 and using structural class *C*, i.e. concrete, as the base-category for the response variable, the log-odds ratios can be calculated as shown in Equation 5-8.

$$
\begin{cases}
\ln(\dfrac{\pi_{C/S}}{\pi_C}) = -2.216 - 0.324x_1 - 0.572x_2 - 0.000013x_3 \\[2mm]
\ln(\dfrac{\pi_{RM}}{\pi_C}) = -0.574 + 0.337x_1 - 0.355x_2 - 0.000012x_3 \\[2mm]
\ln(\dfrac{\pi_{S}}{\pi_C}) = -1.154 - 0.130x_1 - 1.502x_2 + 0.0000084x_3 \\[2mm]
\ln(\dfrac{\pi_{URM}}{\pi_C}) = -0.401 + 0.382x_1 - 0.388x_2 - 0.000017x_3 \\[2mm]
\ln(\dfrac{\pi_{W}}{\pi_C}) = -8.906 + 11408x_1 + 9.099x_2 - 0.000049x_3
\end{cases}
\tag{5-8}
$$

where x_1 and x_2 are dichotomous dummy variables corresponding to height of the structure as defined in Table 5-9. x_3, is a quantitative variable corresponding to average square footage of the structure in ft^2.

Table 5-9 Dummy Variables x_1 and x_2 as Indicators of Height in Equation 5-8

Height (High-rise)	0	0
Height (Medium-rise)	1	0
Height (Low-rise)	0	1

Therefore, the marginal mass-probability density of the observation falling into different response categories can be computed, using $x_1 = 0$, $x_2 = 1$ and $x_3 = 2176$, as shown below:

$$
\begin{cases}
\pi_C = \dfrac{1}{1+e^{-2.817401}+e^{-0.9549136}+e^{-2.63715737}+e^{-0.8268078}+e^{+0.8956142}} = 0.2271515 \\[2mm]
\pi_{C/S} = \dfrac{e^{-2.817401}}{1+e^{-2.817401}+e^{-0.9549136}+e^{-2.63715737}+e^{-0.8268078}+e^{+0.8956142}} = 0.01357467 \\[2mm]
\pi_{RM} = \dfrac{e^{-0.9549136}}{1+e^{-2.817401}+e^{-0.9549136}+e^{-2.63715737}+e^{-0.8268078}+e^{+0.8956142}} = 0.0874174 \\[2mm]
\pi_S = \dfrac{e^{-2.63715737}}{1+e^{-2.817401}+e^{-0.9549136}+e^{-2.63715737}+e^{-0.8268078}+e^{+0.8956142}} = 0.01625607 \\[2mm]
\pi_{URM} = \dfrac{e^{-0.8268078}}{1+e^{-2.817401}+e^{-0.9549136}+e^{-2.63715737}+e^{-0.8268078}+e^{+0.8956142}} = 0.09936458 \\[2mm]
\pi_W = \dfrac{e^{+0.8956142}}{1+e^{-2.817401}+e^{-0.9549136}+e^{-2.63715737}+e^{-0.8268078}+e^{+0.8956142}} = 0.5562357
\end{cases}
\tag{5-9}
$$

Hence, the probability vector $\Pi = \{\pi_C, \pi_{C/S}, \pi_{RM}, \pi_S, \pi_{URM}, \pi_W\}$ can be assembled as:

$$\Pi = \{0.2272\ ,\ 0.01357\ ,\ 0.0874\ ,\ 0.0163\ ,\ 0.0994\ ,\ 0.5562\}$$

It can be seen that the last category, i.e. *W*, in the probability vector Π has the highest value and therefore, in absence of any other information such as age or occupancy type, the predicted structural type of a low-rise building with an average square footage of 2,176 ft^2 is *wood frame*. This class prediction is in agreement with one of the observations from the *dataset A.*

5.5 Conclusions

The multinomial logistic models presented in this report provide the means to compute quantitative measures of marginal building class-membership probabilities for categorical attributes associated with structures. Based on the comparison of similar models presented in Tables 6 and 7, it can be seen that the more detailed training database, i.e. *dataset B*, results in models with a better prediction rate. Furthermore, it can be seen that for the multinomial logistic models with similar explanatory variables, inferring the structural type generally results in a

lower prediction error than inferring the occupancy type. Therefore, it can be concluded that in predicting marginal probabilities, use of structural type as the independent variable generally results in a smaller classification error than the occupancy type.

SECTION 6
REFERENCES

Allen, C.T., (1995), Review Article: Interferometric Synthetic Aperture Radar, http://www.ittc.ukans.edu/publications/documents/Allen1995_Allen1995GRSSNpp6.pdf

Ameri, B., (2000), Feature based model verification (FBMV): A new concept for hypothesis validation in building reconstruction, *Proceedings of the XIXth ISPRS Congress, International Archives of Photogrammetry and Remote Sensing* 33(B3): 24-35.

Axelsson, P., (1999), Processing of laser scanner data − algorithms and applications, *ISPRS Journal of Photogrammetry and Remote Sensing*, 54: 138-147.

Baltsavias, E., Pateraki, M. and Zhang, L., (2001), Radiometric and geometric evaluation of IKONOS images for 3D building evaluation*, Proceedings of the ISPRS Workshop on High Resolution Mapping from Space*, Hanover, Germany.

Bolter, R., (2000), Reconstruction of Man-Made Objects from High Resolution SAR Images, *Proceedings of the IEEE Aerospace Conference*, Big Sky, Montana, Paper-No. 6.0305.

Bolter, R. and Leberl, F., (2000a), Phenomenology-Based and Interferometry-Guided Building Reconstruction from Multiple SAR Images. *Proceedings of EUSAR*, Munich, 687-690.

Bolter, R. and Leberl, F., (2000b), Shape-from-Shadow Building Reconstruction from Multiple View SAR Images. In Sablatnig R. (ed) *Applications of 3D-Imaging and Graph-Based Modeling 2000, 24th Workshop of the Austrian Association for Pattern Recognition (ÖAGM/AAPR)*, Österreichische Computer Gesellschaft, Band 142, Villach, Austria, 196-206.

Bolter, R., and Leberl, F., (2000c), Detection and Reconstruction of Buildings from Multiple View Interferometric SAR Data, *Proceedings of IGARSS 2000*, Hawaii, 749-751.

Bolter, R. and Leberl, F., (2000d), Detection and Reconstruction of Human Scale Features from High Resolution Interferometric SAR Data, *Proceedings of the ICPR, Volume 4: Applications, Robotics Systems and Architectures*, Barcelona, Spain, 291-294.

Bolter, R. and Leberl, F., (2000e), Fusion of Multiple View Interferometric and Slant Range SAR Data for Building Reconstruction, *EOS/SPIE Remote Sensing Symposium, Conference on SAR Image Analysis, Modeling, and Techniques III*, SPIE Vol. 4173: 241-250.

Brenner, C., (1999), Intractive modeling tools for 3D building reconstruction, *47th Photogrammetric Week* , Stuttgart, Wichmann, 23-34.

Brenner, C., (2000), Towards fully automatic generation of city models, *IAPRS, ISPRS Congress,* Amsterdam, 33(B3).

Brenner, C. and Haala, N., (1998), Fast Production of Virtual Reality City Models, In Fritsch, D., Englich, M. and Sester, M. (eds), *IAPRS, ISPRS Commission IV Symposium on GIS - Between Visions and Applications, Stuttgart*, 32(4): 77-84.

Brunn, A., Gulch, E., Lang, F. and Forstner, W., (1998), A hybrid concept for 3D building acquisition, *ISPRS Journal of Photogrammetry and Remote Sensing* 53(1):119–128.

Chilton, T.D., Jaafar, J. and Priestnall, G., (1999), The use of laser scanner data for the extraction of building roof detail using standard elevation derived parameters, *International Archives of Photogrammetry and Remote Sensing*, 32(3W14): 137-143.

Collins, R.T., Hanson, A.R., Riseman, E.M. and Schultz, H., (1995), Automatic extraction of buildings and terrain from aerial images, *International Workshop on Automatic Extraction of Man-Made Objects from Aerial and Space Images. Ascona, Switzerland,* 169-178.

Dial, G. and Grodecki, J., (2005), "RPC Replacement Camera Models", *The International Archives Of Photogrammetry, Remote Sensing and Spatial Information Sciences*, Volume 34, Part XXX.

Duda, R.O., Heart P.E., and Strok, D.G., (2000), "*Pattern Classification,*" John Wiley & Sons.

Eidenbenz, C., Kaser, C. and Baltsavias, E., (2000), ATOMI − Automated reconstruction of topographic objects from aerial images using vectorized map information, *International Archives of Photogrammetry and Remote Sensing*, 33(3/1): 462-471.

EPEDAT, 1994, "*Status Report: Early Post-Earthquake Damage Assessment Tool for Southern California,*" Prepared by EQE International. November 1994.

FEMA154, (2002), "*Rapid Visual Screening of Buildings for Potential Seismic Hazards: A Handbook,*" Federal Emergency Management Agency, 2nd edition, March 2002.

Fraser, C.S., Dial, G., and Grodecki, J., (2006), "Sensor orientation via RPC" *ISPRS Journal of Photogrammetry and Remote Sensing*, Vol. 60, Issue 3, pp. 182-194

Fradkin, M., Roux, M., Maître, H. and Leloğlu, U.M., (1999), Surface Reconstruction from Aerial Images in Dense Urban Areas, CVPR'99, *Proceedings of IEEE Conference on Computer Vision and Pattern Recognition*, Fort Collins, Colorado.

Forstner, W., (1999), 3D-city models: automatic and semiautomatic acquisition methods, In Fritsch, D and Spiller, R. (eds.) *Photogrammetric Week '99*, Wichmann, Heidelberg, 291-303.

Gamba, P. and Houshmand, B., (1999), Integration of high resolution multispectral imagery with LIDAR and IfSAR data for urban analysis applications, *International Archives of Photogrammetry and Remote Sensing*, 32(3W14): 111-117.

Gamba, P. and Houshmand, B., (2000), Digital surface models and building extraction: a comparison of IFSAR and LIDAR data, *IEEE Transactions on Geoscience and Remote Sensing,* 38(4): 1959-1968.

Grodecki, J., Dial, G. and Lutes, J., (2004), "Mathematical Model for 3D Feature Extraction from Multiple Satellite Images Described by RPCs," *ASPRS conference proceedings, Denver Colorado.*

Guindon, B., (1997), Computer-based aerial image understanding: A review and assessment of its application to planimetric information extraction from very high resolution satellite images, *Canadian Journal of Remote Sensing*, **23**: 38-47.

Haala, N., (1999), Combining multiple data sources for urban data acquisition, *Proceedings 47th Photogrammetric Week*, Stuttgart, Wichmann, 329-339.

Haala, N. and Brenner, V., (1999a), Automatic classification of urban environments for database revision using LIDAR and color aerial imagery, *International Archives of Photogrammetry and Remote Sensing, ISPRS Meeting WG6, Valladolid*: 32(7-4-3).

Haala, N. and Brenner, C., (1999b), Extraction of buildings and trees in urban environments, *ISPRS Journal of Photogrammetry and Remote Sensing*, 54: 130-137.

Haala, N. and Brenner, V., (1999c), Laser data for virtual landscape generation, *Proceedings of Workshop for Mapping Surface Structure and Topography by Airborne and Spaceborne Lasers*, La Jolla, California.

Hatze, H., (1988), "High-Precision Three-Dimensional Photogrammetric Calibration and Object Space Reconstruction Using a Modified DLT-Approach," *Journal of Biomechanis*, Vol. 21, issue 7, pp. 533-538.

Heuel, S. and Kolbe, T., (2001), Building reconstruction: the dilemma of generic versus specific models, *Künstliche Intelligenz*, 3, arenDTaP Verlag, Bremen.

Huertas, A., Kim, Z. and Nevatia, R., (2000), Multisensor integration for building modeling, *Computer Vision and Pattern Recognition, 2000 Proceedings, IEEE Conference*, Volume 2, page(s) 203-210.

Huertas, A., Lin., C. and Nevatia, R., (1993), Detection of buildings from monocular views of aerial scenes using perceptual grouping and shadows, *ARPA Image Understanding Workshop*, 253-260.

Huyck, C.K., Eguchi, R.T. and Houshmand, B., (2002), Bare-Earth Algorithms for Use with SAR and LIDAR Digital Elevations Models, MCEER-02-0004 *Technical Report*, MCEER: Buffalo, October 16, 2002.

Jaynes, C.O., Hanson, A., Riseman, E. and Schultz, H., (1997,) *Building reconstruction from optical and range images,* IEEE CVPR. San Juan, Puerto Rico.

Kim, T. and Choi, S.D., (1995), A technique for 3D modeling of buildings, http://www.gisdevelopment.net/aars/acrs/1995/ts5/ts5007.shtml

Kim, Z., Huertas, A. and Nevatia, R., (2001), A model-based approach for multi-view complex building description, *Proc. ASCONA*.

Kirscht, M. and Rinke, C., (1997), 3D reconstruction of buildings and vegetation from synthetic aperture radar (SAR) images, http://www.tnt.uni-hannover.de/plain/project/sar/3dmodel/

Leberl, F. and Bolter, R., (2002), Building reconstruction from synthetic aperture radar images and interferometry , In Gruen, A. (ed)., *3rd Int'l Workshop on Automatic Extraction of Man-Made Objects from Aerial and Space Images*, Monte Verita, Ascona, Switzerland, Volume 3, To appear in Birkhäuser Verlag, Basel-Boston-Zürich.

Lee, S.C., Jung, S.K. and Nevatia, R., (2002), Automatic integration of façade textures into 3D building models with a projective geometry based line clustering, *Computer Graphics Forum (Euro Graphics)*, (21)3: 511-519.

Lemmens, M.J.P.M., (2002), Height information from laser – Altimetry for urban areas, http://www.gisdevelopment.net/application/urban/products/urbanp0004.htm

Lin, C. and Nevatia, R., (1995), 3D description of buildings from an oblique view aerial image, *IEEE International Symposium on Computer Vision*, 377-382.

Lin, C. and Nevatia, R., (1998), Building detection and description from a single intensity image, http://iris.usc.edu/Outlines/papers/1998/lin-cviu98.pdf

Maas, H., (1999a), Fast determination of parametric house models from dense airborne laserscanner data, *International Workshop on Mobile Mapping Technology*, *Bangkok*, *International Archives of Photogrammetry and Remote Sensing*, 32(2W1).

Maas, H., (1999b), The potential of height texture measures for the segmentation *of airborne laserscanner data, Proceedings* of the 4th International Airborne Remote Sensing Conference, I: 154-161, Ottawa.

Madhavan, B.B., Tanahashi, H., Wang, C., Yamamoto, K. and Niwa, Y., (2002), Vision based 3D modeling by using airborne laser scanner data for urban GIS, http://www.gisdevelopment.net/application/urban/products/urbanp0007.htm

McIntosh, K., Krupnik, A. and Schenk, T., (1999), Utilizing airborne laser altimetry for the improvement of automatically generated DEMs over urban areas. *International Archives of Photogrammetry and Remote Sensing,* 32(3-W14):89-94.

Miura, H. and Midorikawa, S., (2003), Use of high-resolution satellite image for updating GIS building inventory data, *Proceedings of the Joint US-Japan Cooperative Research in Urban Earthquake Disaster Mitigation*, Long Beach.

Nevatia, R., Lin, C. and Huertas, A., (1997), A system for building detection form aerial images, Ascona Workshop.

Nevatia, R and Price, K., (2002), Automatic and interactive modeling of buildings in urban environments from aerial images, *IEEE ICIP Rochester, NY*, Volume III: 525-528.

Noronha, S. and Nevatia, R., (1998), Recent advances in detection and description of buildings from multiple aerial images, *ACCV98*, II: 259-266.

Noronha, S. and Nevatia, R., (2001), Detection and modeling of buildings from multiple aerial images, *Transactions on Patter Analysis and Machine Intelligence*, 23(5): 501-518.

Pratt, W. K., (2007), "*Digital Image Processing*," John Wiley & Sons, 4th Ed. ISBN: 978-0-471-76777-0.

Quint, F., (1997), Recognition of structured objects in monocular aerial images using context information, In Leberl, S. (ed) *Mapping buildings, roads and other man-made structures from images*, Munich, 213-228.

Remondino, F. and Fraser, C., (2006), "Digital camera calibration methods: considerations and comparisons" *International Archives of Photogrammetry, Remote Sensing and Spatial Information Sciences*, Vol. XXXVI, part 5, pp. 266-272. ISPRS Commission V Symposium, Dresden, Germany.

Riseman, E.M., Hansom, A.R., Collins, R., Draper, B. and Weiss, R., (1995), Progress in computer vision at the University of Massachusetts,
http://www.cs.colostate.edu/~draper/publications/riseman_iuw94.pdf

Rottensteiner, F. and Briese, C., (2002), A New Method for Building Extraction in Urban Areas from High-Resolution LIDAR Data, *Symposium der ISPRS-Comm. III, Graz, International Archives of Photogrammetry and Remote Sensing,* Volume 34(3A): 295–301.

Rottensteiner, F. and Jansa, J., (2002), Automatic Extraction of Buildings from LIDAR Data and Aerial Images, *Proceedings of the ISPRS Commission IV Symposium in Ottawa, International Archives of Photogrammetry and Remote Sensing*, 34(4): 569-574

Sanz, Pedro J., Roque Marín, J.S. Sánchez, (2005), "Including efficient object recognition capabilities in online robots: from a statistical to a Neural-network classifier," *IEEE Transactions on Systems, Man, and Cybernetics*, Part C 35(1): 87-96.

Sarabandi, P., (2007), "*Development of Algorithms for Building Inventory Compilation through Remote Sensing and Statistical Inferencing,*" Ph.D. Dissertation, Department of Civil and Environmental Engineering, Stanford University, Stanford, CA.

Sohn, G. and Dowman, I.J., (2001), Extraction of buildings from high resolution satellite data, *Proceedings of the 3rd International Workshop on Automatic Extraction of Man-Made Objects from Aerial and Space Images*, Ascona, Switzerland.

Stassopoulou, A. and Caelli, Y., (2000), Building detection using Bayesian networks, *International Journal of Pattern Recognition and Artificial Intelligence*, 14(6): 715-733.

Stilla, U. and Jurkiewicz, K., (1999), Automatic reconstruction of roofs from maps and elevation data, *International Archives of Photogrammetry and Remote Sensing*, 32 (7-4-3).

Suveg, I. and Vosselman, G., (2000), 3D reconstruction of building models, *IAPRS*, 32.

Suveg, I. and Vosselman, G., (2001), 3D building reconstruction by map based generation and evaluation of hypotheses, *12th British Machine Vision Conference*, Manchester, England.

Tao, V. and Hu, Y., (2001a), "The Rational Function Model: A Tool for Processing High-Resolution Imagery," *Earth Observation Magazine*, 10(1), pp. 13-16.

Tao, V. and Hu, Y., (2001b), "A comprehensive Study on The Rational Function Model for Photogrammetric Processing," *Photogrammetric Engineering & Remote Sensing*, 67(12), pp. 1347-1357.

Tao, V. and Hu, Y., (2002), "3D Reconstruction Methods Based on the Rational Function Model," *Photogrammetric Engineering & Remote Sensing*, 68(7), pp. 705-714.

Vestri, C. and Devernay, F., (2000), Improving correlation-based DEMs by image warping and façade correlation, *Proceedings of the International Conference on Computer Vision and Pattern Recognition*, Hilton Head Island, South Carolina.

Weidner, U. and Forstner, W., (1995), Towards automatic building extraction from high resolution digital elevation models, *ISPRS Journal of Photogrammetry and Remote Sensing*, 50(4): 38-49.

Xu, F. and Li, S., (1998), Automatic building extraction in urban area by ALMIMS, *International Conference on Spatial Information Science and Technology*, Wuhan, China.

Xu, F. and Li, S., (2001), Automatic building extraction of ALMIMS, *3rd International Symposium on Mobile Mapping Technology*, 3-5 January 2001, Cairo Egypt, Session 7 Paper 4.

Yang, X., (2000), "Accuracy of Rational Function Approximation in Photogrammetry," *Proceeding of ASPRS Annual Conference*, May 22-26, Washington DC, USA.

APPENDIX A

Appendix A – equivalent Convexity Index

Derivation of Slenderness - Equation 4.38

Area and perimeter of the equivalent rectangle shown in the Figure A.1 can be calculated as below:

$$A = \alpha.l^2$$
$$P = 2(\alpha+1).l \qquad\qquad (A\text{-}1)$$
$$\text{where } \alpha > 1$$
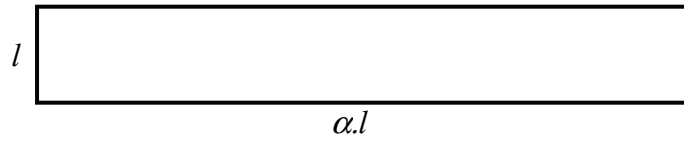
Figure A.1 Equivalent rectangle with α as the ratio between the two sides

Therefore the dimensionless parameter λ can be calculated as expressed by Equation A-2.

$$\lambda = \frac{P^2}{16A} = \frac{4(\alpha+1)^2.l^2}{16.\alpha.l^2} = \frac{(\alpha+1)^2}{4.\alpha} \qquad\qquad (A\text{-}2)$$

The above equation can be rewritten as a quadratic equation of α as shown below:

$$\alpha^2 + 2(1-2\lambda)\alpha + 1 = 0 \qquad\qquad (A\text{-}3)$$

Solving Equation A-3 for α, the two resulting roots are:

$$\alpha_1 = -(1-2\lambda) + \sqrt{(1-2\lambda)^2 - 1} = (2\lambda-1) + 2\sqrt{\lambda(\lambda-1)}$$
$$\alpha_2 = -(1-2\lambda) - \sqrt{(1-2\lambda)^2 - 1} = (2\lambda-1) - 2\sqrt{\lambda(\lambda-1)} \qquad (A\text{-}4)$$

In order for the solution presented by Equation A-4 to have real roots, the discriminant should be positive. Therefore, λ should be such that either $\lambda < 0$ or $\lambda > 1$. As it can be seen from Equation A-2, λ is always a positive value; therefore, the only acceptable range of values for λ is $\lambda > 1$. It can be seen that $\alpha_2 < 1$ for all $\lambda > 1$ which contradicts with the initial assumption that $\alpha > 1$. Hence, the only acceptable solution to Equation A-3 for $\lambda > 1$ and l $\alpha > 1$ is $\alpha = (2\lambda-1) + 2\sqrt{\lambda(\lambda-1)}$. For values of $\lambda < 1$, the slenderness (α) is set to be equal to λ

which corresponds to convex polygons with minimum of $\pi/4$ in case of a circular shape. Therefore, slenderness can be calculated using Equation A-5 as presented below:

$$\alpha = \begin{cases} \lambda & \text{for } \lambda \le 1 \\ 2\lambda - 1 + 2\sqrt{\lambda(\lambda - 1)} & \text{for } \lambda > 1 \end{cases}$$

$$\text{where } \lambda = \frac{P^2}{16A}$$

(A-5)

Derivation of the L-shaped equivalent convexity index - Equation 4.41

Area, perimeter and area of the circumscribed convex polygon of an L-shaped object with slenderness α as the ratio between its sides as shown in the Figure A.2 can be calculated as below:

$$A = (2\alpha - 1).l^2$$
$$P = 4\alpha.l$$
$$A_C = (\frac{\alpha^2 + 2\alpha - 1}{2}).l^2$$

$$\text{where } \alpha > 1$$

(A-6)

Figure A.2 Circumscribed convex polygon for an L-shaped footprint

Therefore, the parameter λ for the L-shaped object shown in Figure A.2 can be calculated as:

$$\lambda = \frac{P^2}{16A} = \frac{\alpha^2}{2\alpha - 1}$$

(A-7)

The equivalent slenderness (α_{eq}) of this shape is then calculated using Equation 3.37 for $\lambda > 1$ as shown below:

$$\alpha_{eq} = 2\lambda - 1 + 2\sqrt{\lambda(\lambda-1)} = 2(\frac{\alpha^2}{2\alpha-1}) - 1 + 2\sqrt{(\frac{\alpha^2}{2\alpha-1})(\frac{\alpha^2}{2\alpha-1}-1)} = 2\alpha - 1 \qquad \text{(A-8)}$$

The equivalent slenderness α_{eq} is the ratio between two sides of an equivalent rectangle which has same slenderness as the L-shaped object in Figure A.2. Convexity index C_I then can be calculated using Equation 3.38 as shown below:

$$C_I = \frac{A_C}{A} = \frac{\alpha^2 + 2\alpha - 1}{2(2\alpha-1)} \qquad \text{(A-9)}$$

The equivalent convexity index for the L-shaped object can be calculated by substituting α_{eq} from Equation A-8 into Equation A-9 as shown below:

$$\alpha = \frac{1}{2}(\alpha_{eq}+1) \Rightarrow C_{eq} = \frac{\frac{1}{4}(\alpha_{eq}+1)^2 + 2(\alpha_{eq}+1) - 1}{2\alpha_{eq}} = \frac{\alpha_{eq}^2 + 6\alpha_{eq} + 1}{8\alpha_{eq}} \qquad \text{(A-10)}$$

Derivation of the L-shaped equivalent convexity index - Equation 4.42

Area, perimeter and area of the circumscribed convex polygon of a U-shaped object with slenderness α as the ratio between its sides as shown in the Figure A.3 can be calculated as below:

$$\begin{aligned} A &= (3\alpha - 2).l^2 \\ P &= 2(3\alpha - 1).l \\ A_C &= \alpha^2.l^2 \\ \text{where } &\alpha > 1 \end{aligned} \qquad \text{(A-11)}$$
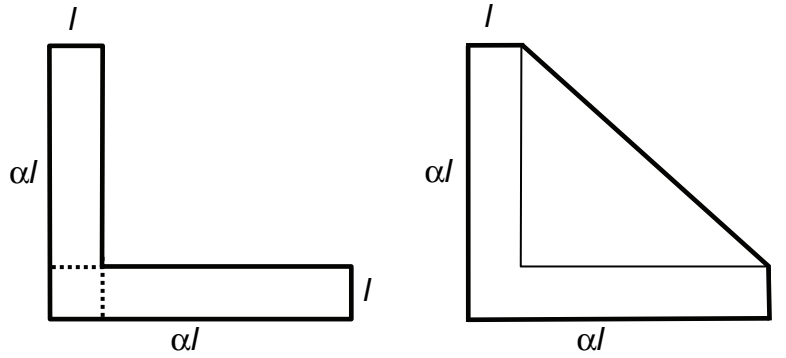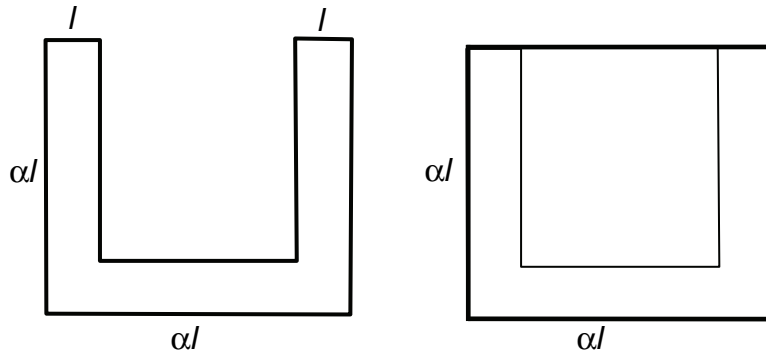

Figure A.3 Circumscribed convex polygon for a U-shaped footprint

Therefore, the parameter λ for the U-shaped object shown in Figure A.3 can be calculated as:

$$\lambda = \frac{P^2}{16A} = \frac{(3\alpha-1)^2}{4(3\alpha-2)} \tag{A-12}$$

The equivalent slenderness (α_{eq}) of this shape is then calculated using Equation 3.37 for $\lambda>1$ as shown below:

$$
\begin{aligned}
\alpha_{eq} &= 2\lambda - 1 + 2\sqrt{\lambda(\lambda-1)} = \frac{(3\alpha-1)^2}{2(3\alpha-2)} - 1 + 2\sqrt{(\frac{(3\alpha-1)^2}{4(3\alpha-2)})(\frac{(3\alpha-1)^2}{4(3\alpha-2)}-1)} \\
&= \frac{(3\alpha-1)^2}{2(3\alpha-2)} - 1 + \frac{1}{2(3\alpha-2)}\sqrt{(3\alpha-1)^2[(3\alpha-1)^2-4(3\alpha-2)]} \\
&= \frac{(3\alpha-1)^2 - 2(3\alpha-2) + \sqrt{(3\alpha-1)^2[(3\alpha-1)^2-4(3\alpha-2)]}}{2(3\alpha-2)} \\
&= \frac{(3\alpha-1)^2 - 2(3\alpha-2) + 3(3\alpha-1)(\alpha-1)}{2(3\alpha-2)} = 3\alpha-2
\end{aligned}
\tag{A-13}
$$

The equivalent slenderness α_{eq} is the ratio between two sides of an equivalent rectangle which has same slenderness as the U-shaped object in Figure A.3. Convexity index C_I then can be calculated using Equation 3.38 as shown below:

$$C_I = \frac{A_C}{A} = \frac{\alpha^2}{3\alpha-2} \tag{A-14}$$

The equivalent convexity index for the U-shaped object can be calculated by substituting α_{eq} from Equation A-13 into Equation A-14 as shown below:

$$\alpha = \frac{1}{3}(\alpha_{eq}+2) \Rightarrow C_{eq} = \frac{(\alpha_{eq}+2)^2}{9\alpha_{eq}} = \frac{\alpha_{eq}^2 + 2\alpha_{eq} + 1}{9\alpha_{eq}} \tag{A-15}$$

MCEER Technical Reports

MCEER publishes technical reports on a variety of subjects written by authors funded through MCEER. These reports are available from both MCEER Publications and the National Technical Information Service (NTIS). Requests for reports should be directed to MCEER Publications, MCEER, University at Buffalo, State University of New York, Red Jacket Quadrangle, Buffalo, New York 14261. Reports can also be requested through NTIS, 5285 Port Royal Road, Springfield, Virginia 22161. NTIS accession numbers are shown in parenthesis, if available.

NCEER-87-0001   "First-Year Program in Research, Education and Technology Transfer," 3/5/87, (PB88-134275, A04, MF-A01).

NCEER-87-0002   "Experimental Evaluation of Instantaneous Optimal Algorithms for Structural Control," by R.C. Lin, T.T. Soong and A.M. Reinhorn, 4/20/87, (PB88-134341, A04, MF-A01).

NCEER-87-0003   "Experimentation Using the Earthquake Simulation Facilities at University at Buffalo," by A.M. Reinhorn and R.L. Ketter, to be published.

NCEER-87-0004   "The System Characteristics and Performance of a Shaking Table," by J.S. Hwang, K.C. Chang and G.C. Lee, 6/1/87, (PB88-134259, A03, MF-A01). This report is available only through NTIS (see address given above).

NCEER-87-0005   "A Finite Element Formulation for Nonlinear Viscoplastic Material Using a Q Model," by O. Gyebi and G. Dasgupta, 11/2/87, (PB88-213764, A08, MF-A01).

NCEER-87-0006   "Symbolic Manipulation Program (SMP) - Algebraic Codes for Two and Three Dimensional Finite Element Formulations," by X. Lee and G. Dasgupta, 11/9/87, (PB88-218522, A05, MF-A01).

NCEER-87-0007   "Instantaneous Optimal Control Laws for Tall Buildings Under Seismic Excitations," by J.N. Yang, A. Akbarpour and P. Ghaemmaghami, 6/10/87, (PB88-134333, A06, MF-A01). This report is only available through NTIS (see address given above).

NCEER-87-0008   "IDARC: Inelastic Damage Analysis of Reinforced Concrete Frame - Shear-Wall Structures," by Y.J. Park, A.M. Reinhorn and S.K. Kunnath, 7/20/87, (PB88-134325, A09, MF-A01). This report is only available through NTIS (see address given above).

NCEER-87-0009   "Liquefaction Potential for New York State: A Preliminary Report on Sites in Manhattan and Buffalo," by M. Budhu, V. Vijayakumar, R.F. Giese and L. Baumgras, 8/31/87, (PB88-163704, A03, MF-A01). This report is available only through NTIS (see address given above).

NCEER-87-0010   "Vertical and Torsional Vibration of Foundations in Inhomogeneous Media," by A.S. Veletsos and K.W. Dotson, 6/1/87, (PB88-134291, A03, MF-A01). This report is only available through NTIS (see address given above).

NCEER-87-0011   "Seismic Probabilistic Risk Assessment and Seismic Margins Studies for Nuclear Power Plants," by Howard H.M. Hwang, 6/15/87, (PB88-134267, A03, MF-A01). This report is only available through NTIS (see address given above).

NCEER-87-0012   "Parametric Studies of Frequency Response of Secondary Systems Under Ground-Acceleration Excitations," by Y. Yong and Y.K. Lin, 6/10/87, (PB88-134309, A03, MF-A01). This report is only available through NTIS (see address given above).

NCEER-87-0013   "Frequency Response of Secondary Systems Under Seismic Excitation," by J.A. HoLung, J. Cai and Y.K. Lin, 7/31/87, (PB88-134317, A05, MF-A01). This report is only available through NTIS (see address given above).

NCEER-87-0014   "Modelling Earthquake Ground Motions in Seismically Active Regions Using Parametric Time Series Methods," by G.W. Ellis and A.S. Cakmak, 8/25/87, (PB88-134283, A08, MF-A01). This report is only available through NTIS (see address given above).

NCEER-87-0015   "Detection and Assessment of Seismic Structural Damage," by E. DiPasquale and A.S. Cakmak, 8/25/87, (PB88-163712, A05, MF-A01). This report is only available through NTIS (see address given above).

NCEER-87-0016   "Pipeline Experiment at Parkfield, California," by J. Isenberg and E. Richardson, 9/15/87, (PB88-163720, A03, MF-A01). This report is available only through NTIS (see address given above).

NCEER-87-0017   "Digital Simulation of Seismic Ground Motion," by M. Shinozuka, G. Deodatis and T. Harada, 8/31/87, (PB88-155197, A04, MF-A01). This report is available only through NTIS (see address given above).

NCEER-87-0018   "Practical Considerations for Structural Control: System Uncertainty, System Time Delay and Truncation of Small Control Forces," J.N. Yang and A. Akbarpour, 8/10/87, (PB88-163738, A08, MF-A01). This report is only available through NTIS (see address given above).

NCEER-87-0019   "Modal Analysis of Nonclassically Damped Structural Systems Using Canonical Transformation," by J.N. Yang, S. Sarkani and F.X. Long, 9/27/87, (PB88-187851, A04, MF-A01).

NCEER-87-0020   "A Nonstationary Solution in Random Vibration Theory," by J.R. Red-Horse and P.D. Spanos, 11/3/87, (PB88-163746, A03, MF-A01).

NCEER-87-0021   "Horizontal Impedances for Radially Inhomogeneous Viscoelastic Soil Layers," by A.S. Veletsos and K.W. Dotson, 10/15/87, (PB88-150859, A04, MF-A01).

NCEER-87-0022   "Seismic Damage Assessment of Reinforced Concrete Members," by Y.S. Chung, C. Meyer and M. Shinozuka, 10/9/87, (PB88-150867, A05, MF-A01). This report is available only through NTIS (see address given above).

NCEER-87-0023   "Active Structural Control in Civil Engineering," by T.T. Soong, 11/11/87, (PB88-187778, A03, MF-A01).

NCEER-87-0024   "Vertical and Torsional Impedances for Radially Inhomogeneous Viscoelastic Soil Layers," by K.W. Dotson and A.S. Veletsos, 12/87, (PB88-187786, A03, MF-A01).

NCEER-87-0025   "Proceedings from the Symposium on Seismic Hazards, Ground Motions, Soil-Liquefaction and Engineering Practice in Eastern North America," October 20-22, 1987, edited by K.H. Jacob, 12/87, (PB88-188115, A23, MF-A01). This report is available only through NTIS (see address given above).

NCEER-87-0026   "Report on the Whittier-Narrows, California, Earthquake of October 1, 1987," by J. Pantelic and A. Reinhorn, 11/87, (PB88-187752, A03, MF-A01). This report is available only through NTIS (see address given above).

NCEER-87-0027   "Design of a Modular Program for Transient Nonlinear Analysis of Large 3-D Building Structures," by S. Srivastav and J.F. Abel, 12/30/87, (PB88-187950, A05, MF-A01). This report is only available through NTIS (see address given above).

NCEER-87-0028   "Second-Year Program in Research, Education and Technology Transfer," 3/8/88, (PB88-219480, A04, MF-A01).

NCEER-88-0001   "Workshop on Seismic Computer Analysis and Design of Buildings With Interactive Graphics," by W. McGuire, J.F. Abel and C.H. Conley, 1/18/88, (PB88-187760, A03, MF-A01). This report is only available through NTIS (see address given above).

NCEER-88-0002   "Optimal Control of Nonlinear Flexible Structures," by J.N. Yang, F.X. Long and D. Wong, 1/22/88, (PB88-213772, A06, MF-A01).

NCEER-88-0003   "Substructuring Techniques in the Time Domain for Primary-Secondary Structural Systems," by G.D. Manolis and G. Juhn, 2/10/88, (PB88-213780, A04, MF-A01).

NCEER-88-0004   "Iterative Seismic Analysis of Primary-Secondary Systems," by A. Singhal, L.D. Lutes and P.D. Spanos, 2/23/88, (PB88-213798, A04, MF-A01).

NCEER-88-0005   "Stochastic Finite Element Expansion for Random Media," by P.D. Spanos and R. Ghanem, 3/14/88, (PB88-213806, A03, MF-A01).

NCEER-88-0006   "Combining Structural Optimization and Structural Control," by F.Y. Cheng and C.P. Pantelides, 1/10/88, (PB88-213814, A05, MF-A01).

NCEER-88-0007   "Seismic Performance Assessment of Code-Designed Structures," by H.H-M. Hwang, J-W. Jaw and H-J. Shau, 3/20/88, (PB88-219423, A04, MF-A01). This report is only available through NTIS (see address given above).

NCEER-88-0008   "Reliability Analysis of Code-Designed Structures Under Natural Hazards," by H.H-M. Hwang, H. Ushiba and M. Shinozuka, 2/29/88, (PB88-229471, A07, MF-A01). This report is only available through NTIS (see address given above).

NCEER-88-0009   "Seismic Fragility Analysis of Shear Wall Structures," by J-W Jaw and H.H-M. Hwang, 4/30/88, (PB89-102867, A04, MF-A01).

NCEER-88-0010   "Base Isolation of a Multi-Story Building Under a Harmonic Ground Motion - A Comparison of Performances of Various Systems," by F-G Fan, G. Ahmadi and I.G. Tadjbakhsh, 5/18/88, (PB89-122238, A06, MF-A01). This report is only available through NTIS (see address given above).

NCEER-88-0011   "Seismic Floor Response Spectra for a Combined System by Green's Functions," by F.M. Lavelle, L.A. Bergman and P.D. Spanos, 5/1/88, (PB89-102875, A03, MF-A01).

NCEER-88-0012   "A New Solution Technique for Randomly Excited Hysteretic Structures," by G.Q. Cai and Y.K. Lin, 5/16/88, (PB89-102883, A03, MF-A01).

NCEER-88-0013   "A Study of Radiation Damping and Soil-Structure Interaction Effects in the Centrifuge," by K. Weissman, supervised by J.H. Prevost, 5/24/88, (PB89-144703, A06, MF-A01).

NCEER-88-0014   "Parameter Identification and Implementation of a Kinematic Plasticity Model for Frictional Soils," by J.H. Prevost and D.V. Griffiths, to be published.

NCEER-88-0015   "Two- and Three- Dimensional Dynamic Finite Element Analyses of the Long Valley Dam," by D.V. Griffiths and J.H. Prevost, 6/17/88, (PB89-144711, A04, MF-A01).

NCEER-88-0016   "Damage Assessment of Reinforced Concrete Structures in Eastern United States," by A.M. Reinhorn, M.J. Seidel, S.K. Kunnath and Y.J. Park, 6/15/88, (PB89-122220, A04, MF-A01). This report is only available through NTIS (see address given above).

NCEER-88-0017   "Dynamic Compliance of Vertically Loaded Strip Foundations in Multilayered Viscoelastic Soils," by S. Ahmad and A.S.M. Israil, 6/17/88, (PB89-102891, A04, MF-A01).

NCEER-88-0018   "An Experimental Study of Seismic Structural Response With Added Viscoelastic Dampers," by R.C. Lin, Z. Liang, T.T. Soong and R.H. Zhang, 6/30/88, (PB89-122212, A05, MF-A01). This report is available only through NTIS (see address given above).

NCEER-88-0019   "Experimental Investigation of Primary - Secondary System Interaction," by G.D. Manolis, G. Juhn and A.M. Reinhorn, 5/27/88, (PB89-122204, A04, MF-A01).

NCEER-88-0020   "A Response Spectrum Approach For Analysis of Nonclassically Damped Structures," by J.N. Yang, S. Sarkani and F.X. Long, 4/22/88, (PB89-102909, A04, MF-A01).

NCEER-88-0021   "Seismic Interaction of Structures and Soils: Stochastic Approach," by A.S. Veletsos and A.M. Prasad, 7/21/88, (PB89-122196, A04, MF-A01). This report is only available through NTIS (see address given above).

NCEER-88-0022   "Identification of the Serviceability Limit State and Detection of Seismic Structural Damage," by E. DiPasquale and A.S. Cakmak, 6/15/88, (PB89-122188, A05, MF-A01). This report is available only through NTIS (see address given above).

NCEER-88-0023   "Multi-Hazard Risk Analysis: Case of a Simple Offshore Structure," by B.K. Bhartia and E.H. Vanmarcke, 7/21/88, (PB89-145213, A05, MF-A01).

NCEER-88-0024   "Automated Seismic Design of Reinforced Concrete Buildings," by Y.S. Chung, C. Meyer and M. Shinozuka, 7/5/88, (PB89-122170, A06, MF-A01). This report is available only through NTIS (see address given above).

NCEER-88-0025   "Experimental Study of Active Control of MDOF Structures Under Seismic Excitations," by L.L. Chung, R.C. Lin, T.T. Soong and A.M. Reinhorn, 7/10/88, (PB89-122600, A04, MF-A01).

NCEER-88-0026   "Earthquake Simulation Tests of a Low-Rise Metal Structure," by J.S. Hwang, K.C. Chang, G.C. Lee and R.L. Ketter, 8/1/88, (PB89-102917, A04, MF-A01).

NCEER-88-0027   "Systems Study of Urban Response and Reconstruction Due to Catastrophic Earthquakes," by F. Kozin and H.K. Zhou, 9/22/88, (PB90-162348, A04, MF-A01).

NCEER-88-0028   "Seismic Fragility Analysis of Plane Frame Structures," by H.H-M. Hwang and Y.K. Low, 7/31/88, (PB89-131445, A06, MF-A01).

NCEER-88-0029   "Response Analysis of Stochastic Structures," by A. Kardara, C. Bucher and M. Shinozuka, 9/22/88, (PB89-174429, A04, MF-A01).

NCEER-88-0030   "Nonnormal Accelerations Due to Yielding in a Primary Structure," by D.C.K. Chen and L.D. Lutes, 9/19/88, (PB89-131437, A04, MF-A01).

NCEER-88-0031   "Design Approaches for Soil-Structure Interaction," by A.S. Veletsos, A.M. Prasad and Y. Tang, 12/30/88, (PB89-174437, A03, MF-A01). This report is available only through NTIS (see address given above).

NCEER-88-0032   "A Re-evaluation of Design Spectra for Seismic Damage Control," by C.J. Turkstra and A.G. Tallin, 11/7/88, (PB89-145221, A05, MF-A01).

NCEER-88-0033   "The Behavior and Design of Noncontact Lap Splices Subjected to Repeated Inelastic Tensile Loading," by V.E. Sagan, P. Gergely and R.N. White, 12/8/88, (PB89-163737, A08, MF-A01).

NCEER-88-0034   "Seismic Response of Pile Foundations," by S.M. Mamoon, P.K. Banerjee and S. Ahmad, 11/1/88, (PB89-145239, A04, MF-A01).

NCEER-88-0035   "Modeling of R/C Building Structures With Flexible Floor Diaphragms (IDARC2)," by A.M. Reinhorn, S.K. Kunnath and N. Panahshahi, 9/7/88, (PB89-207153, A07, MF-A01).

NCEER-88-0036   "Solution of the Dam-Reservoir Interaction Problem Using a Combination of FEM, BEM with Particular Integrals, Modal Analysis, and Substructuring," by C-S. Tsai, G.C. Lee and R.L. Ketter, 12/31/88, (PB89-207146, A04, MF-A01).

NCEER-88-0037   "Optimal Placement of Actuators for Structural Control," by F.Y. Cheng and C.P. Pantelides, 8/15/88, (PB89-162846, A05, MF-A01).

NCEER-88-0038   "Teflon Bearings in Aseismic Base Isolation: Experimental Studies and Mathematical Modeling," by A. Mokha, M.C. Constantinou and A.M. Reinhorn, 12/5/88, (PB89-218457, A10, MF-A01). This report is available only through NTIS (see address given above).

NCEER-88-0039   "Seismic Behavior of Flat Slab High-Rise Buildings in the New York City Area," by P. Weidlinger and M. Ettouney, 10/15/88, (PB90-145681, A04, MF-A01).

NCEER-88-0040   "Evaluation of the Earthquake Resistance of Existing Buildings in New York City," by P. Weidlinger and M. Ettouney, 10/15/88, to be published.

NCEER-88-0041   "Small-Scale Modeling Techniques for Reinforced Concrete Structures Subjected to Seismic Loads," by W. Kim, A. El-Attar and R.N. White, 11/22/88, (PB89-189625, A05, MF-A01).

NCEER-88-0042   "Modeling Strong Ground Motion from Multiple Event Earthquakes," by G.W. Ellis and A.S. Cakmak, 10/15/88, (PB89-174445, A03, MF-A01).

NCEER-88-0043   "Nonstationary Models of Seismic Ground Acceleration," by M. Grigoriu, S.E. Ruiz and E. Rosenblueth, 7/15/88, (PB89-189617, A04, MF-A01).

NCEER-88-0044   "SARCF User's Guide: Seismic Analysis of Reinforced Concrete Frames," by Y.S. Chung, C. Meyer and M. Shinozuka, 11/9/88, (PB89-174452, A08, MF-A01).

NCEER-88-0045   "First Expert Panel Meeting on Disaster Research and Planning," edited by J. Pantelic and J. Stoyle, 9/15/88, (PB89-174460, A05, MF-A01).

NCEER-88-0046   "Preliminary Studies of the Effect of Degrading Infill Walls on the Nonlinear Seismic Response of Steel Frames," by C.Z. Chrysostomou, P. Gergely and J.F. Abel, 12/19/88, (PB89-208383, A05, MF-A01).

NCEER-88-0047   "Reinforced Concrete Frame Component Testing Facility - Design, Construction, Instrumentation and Operation," by S.P. Pessiki, C. Conley, T. Bond, P. Gergely and R.N. White, 12/16/88, (PB89-174478, A04, MF-A01).

NCEER-89-0001   "Effects of Protective Cushion and Soil Compliancy on the Response of Equipment Within a Seismically Excited Building," by J.A. HoLung, 2/16/89, (PB89-207179, A04, MF-A01).

NCEER-89-0002   "Statistical Evaluation of Response Modification Factors for Reinforced Concrete Structures," by H.H-M. Hwang and J-W. Jaw, 2/17/89, (PB89-207187, A05, MF-A01).

NCEER-89-0003   "Hysteretic Columns Under Random Excitation," by G-Q. Cai and Y.K. Lin, 1/9/89, (PB89-196513, A03, MF-A01).

NCEER-89-0004   "Experimental Study of `Elephant Foot Bulge' Instability of Thin-Walled Metal Tanks," by Z-H. Jia and R.L. Ketter, 2/22/89, (PB89-207195, A03, MF-A01).

NCEER-89-0005   "Experiment on Performance of Buried Pipelines Across San Andreas Fault," by J. Isenberg, E. Richardson and T.D. O'Rourke, 3/10/89, (PB89-218440, A04, MF-A01). This report is available only through NTIS (see address given above).

NCEER-89-0006   "A Knowledge-Based Approach to Structural Design of Earthquake-Resistant Buildings," by M. Subramani, P. Gergely, C.H. Conley, J.F. Abel and A.H. Zaghw, 1/15/89, (PB89-218465, A06, MF-A01).

NCEER-89-0007   "Liquefaction Hazards and Their Effects on Buried Pipelines," by T.D. O'Rourke and P.A. Lane, 2/1/89, (PB89-218481, A09, MF-A01).

NCEER-89-0008   "Fundamentals of System Identification in Structural Dynamics," by H. Imai, C-B. Yun, O. Maruyama and M. Shinozuka, 1/26/89, (PB89-207211, A04, MF-A01).

NCEER-89-0009   "Effects of the 1985 Michoacan Earthquake on Water Systems and Other Buried Lifelines in Mexico," by A.G. Ayala and M.J. O'Rourke, 3/8/89, (PB89-207229, A06, MF-A01).

NCEER-89-R010   "NCEER Bibliography of Earthquake Education Materials," by K.E.K. Ross, Second Revision, 9/1/89, (PB90-125352, A05, MF-A01). This report is replaced by NCEER-92-0018.

NCEER-89-0011   "Inelastic Three-Dimensional Response Analysis of Reinforced Concrete Building Structures (IDARC-3D), Part I - Modeling," by S.K. Kunnath and A.M. Reinhorn, 4/17/89, (PB90-114612, A07, MF-A01). This report is available only through NTIS (see address given above).

NCEER-89-0012   "Recommended Modifications to ATC-14," by C.D. Poland and J.O. Malley, 4/12/89, (PB90-108648, A15, MF-A01).

NCEER-89-0013   "Repair and Strengthening of Beam-to-Column Connections Subjected to Earthquake Loading," by M. Corazao and A.J. Durrani, 2/28/89, (PB90-109885, A06, MF-A01).

NCEER-89-0014   "Program EXKAL2 for Identification of Structural Dynamic Systems," by O. Maruyama, C-B. Yun, M. Hoshiya and M. Shinozuka, 5/19/89, (PB90-109877, A09, MF-A01).

NCEER-89-0015   "Response of Frames With Bolted Semi-Rigid Connections, Part I - Experimental Study and Analytical Predictions," by P.J. DiCorso, A.M. Reinhorn, J.R. Dickerson, J.B. Radziminski and W.L. Harper, 6/1/89, to be published.

NCEER-89-0016   "ARMA Monte Carlo Simulation in Probabilistic Structural Analysis," by P.D. Spanos and M.P. Mignolet, 7/10/89, (PB90-109893, A03, MF-A01).

NCEER-89-P017   "Preliminary Proceedings from the Conference on Disaster Preparedness - The Place of Earthquake Education in Our Schools," Edited by K.E.K. Ross, 6/23/89, (PB90-108606, A03, MF-A01).

NCEER-89-0017   "Proceedings from the Conference on Disaster Preparedness - The Place of Earthquake Education in Our Schools," Edited by K.E.K. Ross, 12/31/89, (PB90-207895, A012, MF-A02). This report is available only through NTIS (see address given above).

NCEER-89-0018   "Multidimensional Models of Hysteretic Material Behavior for Vibration Analysis of Shape Memory Energy Absorbing Devices, by E.J. Graesser and F.A. Cozzarelli, 6/7/89, (PB90-164146, A04, MF-A01).

NCEER-89-0019   "Nonlinear Dynamic Analysis of Three-Dimensional Base Isolated Structures (3D-BASIS)," by S. Nagarajaiah, A.M. Reinhorn and M.C. Constantinou, 8/3/89, (PB90-161936, A06, MF-A01). This report has been replaced by NCEER-93-0011.

NCEER-89-0020   "Structural Control Considering Time-Rate of Control Forces and Control Rate Constraints," by F.Y. Cheng and C.P. Pantelides, 8/3/89, (PB90-120445, A04, MF-A01).

NCEER-89-0021   "Subsurface Conditions of Memphis and Shelby County," by K.W. Ng, T-S. Chang and H-H.M. Hwang, 7/26/89, (PB90-120437, A03, MF-A01).

NCEER-89-0022   "Seismic Wave Propagation Effects on Straight Jointed Buried Pipelines," by K. Elhmadi and M.J. O'Rourke, 8/24/89, (PB90-162322, A10, MF-A02).

NCEER-89-0023   "Workshop on Serviceability Analysis of Water Delivery Systems," edited by M. Grigoriu, 3/6/89, (PB90-127424, A03, MF-A01).

NCEER-89-0024   "Shaking Table Study of a 1/5 Scale Steel Frame Composed of Tapered Members," by K.C. Chang, J.S. Hwang and G.C. Lee, 9/18/89, (PB90-160169, A04, MF-A01).

NCEER-89-0025   "DYNA1D: A Computer Program for Nonlinear Seismic Site Response Analysis - Technical Documentation," by Jean H. Prevost, 9/14/89, (PB90-161944, A07, MF-A01). This report is available only through NTIS (see address given above).

NCEER-89-0026   "1:4 Scale Model Studies of Active Tendon Systems and Active Mass Dampers for Aseismic Protection," by A.M. Reinhorn, T.T. Soong, R.C. Lin, Y.P. Yang, Y. Fukao, H. Abe and M. Nakai, 9/15/89, (PB90-173246, A10, MF-A02). This report is available only through NTIS (see address given above).

NCEER-89-0027   "Scattering of Waves by Inclusions in a Nonhomogeneous Elastic Half Space Solved by Boundary Element Methods," by P.K. Hadley, A. Askar and A.S. Cakmak, 6/15/89, (PB90-145699, A07, MF-A01).

NCEER-89-0028   "Statistical Evaluation of Deflection Amplification Factors for Reinforced Concrete Structures," by H.H.M. Hwang, J-W. Jaw and A.L. Ch'ng, 8/31/89, (PB90-164633, A05, MF-A01).

NCEER-89-0029   "Bedrock Accelerations in Memphis Area Due to Large New Madrid Earthquakes," by H.H.M. Hwang, C.H.S. Chen and G. Yu, 11/7/89, (PB90-162330, A04, MF-A01).

NCEER-89-0030   "Seismic Behavior and Response Sensitivity of Secondary Structural Systems," by Y.Q. Chen and T.T. Soong, 10/23/89, (PB90-164658, A08, MF-A01).

NCEER-89-0031   "Random Vibration and Reliability Analysis of Primary-Secondary Structural Systems," by Y. Ibrahim, M. Grigoriu and T.T. Soong, 11/10/89, (PB90-161951, A04, MF-A01).

NCEER-89-0032   "Proceedings from the Second U.S. - Japan Workshop on Liquefaction, Large Ground Deformation and Their Effects on Lifelines, September 26-29, 1989," Edited by T.D. O'Rourke and M. Hamada, 12/1/89, (PB90-209388, A22, MF-A03).

NCEER-89-0033   "Deterministic Model for Seismic Damage Evaluation of Reinforced Concrete Structures," by J.M. Bracci, A.M. Reinhorn, J.B. Mander and S.K. Kunnath, 9/27/89, (PB91-108803, A06, MF-A01).

NCEER-89-0034   "On the Relation Between Local and Global Damage Indices," by E. DiPasquale and A.S. Cakmak, 8/15/89, (PB90-173865, A05, MF-A01).

NCEER-89-0035   "Cyclic Undrained Behavior of Nonplastic and Low Plasticity Silts," by A.J. Walker and H.E. Stewart, 7/26/89, (PB90-183518, A10, MF-A01).

NCEER-89-0036   "Liquefaction Potential of Surficial Deposits in the City of Buffalo, New York," by M. Budhu, R. Giese and L. Baumgrass, 1/17/89, (PB90-208455, A04, MF-A01).

NCEER-89-0037   "A Deterministic Assessment of Effects of Ground Motion Incoherence," by A.S. Veletsos and Y. Tang, 7/15/89, (PB90-164294, A03, MF-A01).

NCEER-89-0038   "Workshop on Ground Motion Parameters for Seismic Hazard Mapping," July 17-18, 1989, edited by R.V. Whitman, 12/1/89, (PB90-173923, A04, MF-A01).

NCEER-89-0039   "Seismic Effects on Elevated Transit Lines of the New York City Transit Authority," by C.J. Costantino, C.A. Miller and E. Heymsfield, 12/26/89, (PB90-207887, A06, MF-A01).

NCEER-89-0040   "Centrifugal Modeling of Dynamic Soil-Structure Interaction," by K. Weissman, Supervised by J.H. Prevost, 5/10/89, (PB90-207879, A07, MF-A01).

NCEER-89-0041   "Linearized Identification of Buildings With Cores for Seismic Vulnerability Assessment," by I-K. Ho and A.E. Aktan, 11/1/89, (PB90-251943, A07, MF-A01).

NCEER-90-0001   "Geotechnical and Lifeline Aspects of the October 17, 1989 Loma Prieta Earthquake in San Francisco," by T.D. O'Rourke, H.E. Stewart, F.T. Blackburn and T.S. Dickerman, 1/90, (PB90-208596, A05, MF-A01).

NCEER-90-0002   "Nonnormal Secondary Response Due to Yielding in a Primary Structure," by D.C.K. Chen and L.D. Lutes, 2/28/90, (PB90-251976, A07, MF-A01).

NCEER-90-0003   "Earthquake Education Materials for Grades K-12," by K.E.K. Ross, 4/16/90, (PB91-251984, A05, MF-A05). This report has been replaced by NCEER-92-0018.

NCEER-90-0004   "Catalog of Strong Motion Stations in Eastern North America," by R.W. Busby, 4/3/90, (PB90-251984, A05, MF-A01).

NCEER-90-0005   "NCEER Strong-Motion Data Base: A User Manual for the GeoBase Release (Version 1.0 for the Sun3)," by P. Friberg and K. Jacob, 3/31/90 (PB90-258062, A04, MF-A01).

NCEER-90-0006   "Seismic Hazard Along a Crude Oil Pipeline in the Event of an 1811-1812 Type New Madrid Earthquake," by H.H.M. Hwang and C-H.S. Chen, 4/16/90, (PB90-258054, A04, MF-A01).

NCEER-90-0007   "Site-Specific Response Spectra for Memphis Sheahan Pumping Station," by H.H.M. Hwang and C.S. Lee, 5/15/90, (PB91-108811, A05, MF-A01).

NCEER-90-0008   "Pilot Study on Seismic Vulnerability of Crude Oil Transmission Systems," by T. Ariman, R. Dobry, M. Grigoriu, F. Kozin, M. O'Rourke, T. O'Rourke and M. Shinozuka, 5/25/90, (PB91-108837, A06, MF-A01).

NCEER-90-0009   "A Program to Generate Site Dependent Time Histories: EQGEN," by G.W. Ellis, M. Srinivasan and A.S. Cakmak, 1/30/90, (PB91-108829, A04, MF-A01).

NCEER-90-0010   "Active Isolation for Seismic Protection of Operating Rooms," by M.E. Talbott, Supervised by M. Shinozuka, 6/8/9, (PB91-110205, A05, MF-A01).

NCEER-90-0011   "Program LINEARID for Identification of Linear Structural Dynamic Systems," by C-B. Yun and M. Shinozuka, 6/25/90, (PB91-110312, A08, MF-A01).

NCEER-90-0012   "Two-Dimensional Two-Phase Elasto-Plastic Seismic Response of Earth Dams," by A.N. Yiagos, Supervised by J.H. Prevost, 6/20/90, (PB91-110197, A13, MF-A02).

NCEER-90-0013   "Secondary Systems in Base-Isolated Structures: Experimental Investigation, Stochastic Response and Stochastic Sensitivity," by G.D. Manolis, G. Juhn, M.C. Constantinou and A.M. Reinhorn, 7/1/90, (PB91-110320, A08, MF-A01).

NCEER-90-0014   "Seismic Behavior of Lightly-Reinforced Concrete Column and Beam-Column Joint Details," by S.P. Pessiki, C.H. Conley, P. Gergely and R.N. White, 8/22/90, (PB91-108795, A11, MF-A02).

NCEER-90-0015   "Two Hybrid Control Systems for Building Structures Under Strong Earthquakes," by J.N. Yang and A. Danielians, 6/29/90, (PB91-125393, A04, MF-A01).

NCEER-90-0016   "Instantaneous Optimal Control with Acceleration and Velocity Feedback," by J.N. Yang and Z. Li, 6/29/90, (PB91-125401, A03, MF-A01).

NCEER-90-0017   "Reconnaissance Report on the Northern Iran Earthquake of June 21, 1990," by M. Mehrain, 10/4/90, (PB91-125377, A03, MF-A01).

NCEER-90-0018   "Evaluation of Liquefaction Potential in Memphis and Shelby County," by T.S. Chang, P.S. Tang, C.S. Lee and H. Hwang, 8/10/90, (PB91-125427, A09, MF-A01).

NCEER-90-0019   "Experimental and Analytical Study of a Combined Sliding Disc Bearing and Helical Steel Spring Isolation System," by M.C. Constantinou, A.S. Mokha and A.M. Reinhorn, 10/4/90, (PB91-125385, A06, MF-A01). This report is available only through NTIS (see address given above).

NCEER-90-0020   "Experimental Study and Analytical Prediction of Earthquake Response of a Sliding Isolation System with a Spherical Surface," by A.S. Mokha, M.C. Constantinou and A.M. Reinhorn, 10/11/90, (PB91-125419, A05, MF-A01).

NCEER-90-0021   "Dynamic Interaction Factors for Floating Pile Groups," by G. Gazetas, K. Fan, A. Kaynia and E. Kausel, 9/10/90, (PB91-170381, A05, MF-A01).

NCEER-90-0022   "Evaluation of Seismic Damage Indices for Reinforced Concrete Structures," by S. Rodriguez-Gomez and A.S. Cakmak, 9/30/90, PB91-171322, A06, MF-A01).

NCEER-90-0023   "Study of Site Response at a Selected Memphis Site," by H. Desai, S. Ahmad, E.S. Gazetas and M.R. Oh, 10/11/90, (PB91-196857, A03, MF-A01).

NCEER-90-0024   "A User's Guide to Strongmo: Version 1.0 of NCEER's Strong-Motion Data Access Tool for PCs and Terminals," by P.A. Friberg and C.A.T. Susch, 11/15/90, (PB91-171272, A03, MF-A01).

NCEER-90-0025   "A Three-Dimensional Analytical Study of Spatial Variability of Seismic Ground Motions," by L-L. Hong and A.H.-S. Ang, 10/30/90, (PB91-170399, A09, MF-A01).

NCEER-90-0026   "MUMOID User's Guide - A Program for the Identification of Modal Parameters," by S. Rodriguez-Gomez and E. DiPasquale, 9/30/90, (PB91-171298, A04, MF-A01).

NCEER-90-0027   "SARCF-II User's Guide - Seismic Analysis of Reinforced Concrete Frames," by S. Rodriguez-Gomez, Y.S. Chung and C. Meyer, 9/30/90, (PB91-171280, A05, MF-A01).

NCEER-90-0028   "Viscous Dampers: Testing, Modeling and Application in Vibration and Seismic Isolation," by N. Makris and M.C. Constantinou, 12/20/90 (PB91-190561, A06, MF-A01).

NCEER-90-0029   "Soil Effects on Earthquake Ground Motions in the Memphis Area," by H. Hwang, C.S. Lee, K.W. Ng and T.S. Chang, 8/2/90, (PB91-190751, A05, MF-A01).

NCEER-91-0001   "Proceedings from the Third Japan-U.S. Workshop on Earthquake Resistant Design of Lifeline Facilities and Countermeasures for Soil Liquefaction, December 17-19, 1990," edited by T.D. O'Rourke and M. Hamada, 2/1/91, (PB91-179259, A99, MF-A04).

NCEER-91-0002   "Physical Space Solutions of Non-Proportionally Damped Systems," by M. Tong, Z. Liang and G.C. Lee, 1/15/91, (PB91-179242, A04, MF-A01).

NCEER-91-0003   "Seismic Response of Single Piles and Pile Groups," by K. Fan and G. Gazetas, 1/10/91, (PB92-174994, A04, MF-A01).

NCEER-91-0004   "Damping of Structures: Part 1 - Theory of Complex Damping," by Z. Liang and G. Lee, 10/10/91, (PB92-197235, A12, MF-A03).

NCEER-91-0005   "3D-BASIS - Nonlinear Dynamic Analysis of Three Dimensional Base Isolated Structures: Part II," by S. Nagarajaiah, A.M. Reinhorn and M.C. Constantinou, 2/28/91, (PB91-190553, A07, MF-A01). This report has been replaced by NCEER-93-0011.

NCEER-91-0006   "A Multidimensional Hysteretic Model for Plasticity Deforming Metals in Energy Absorbing Devices," by E.J. Graesser and F.A. Cozzarelli, 4/9/91, (PB92-108364, A04, MF-A01).

NCEER-91-0007   "A Framework for Customizable Knowledge-Based Expert Systems with an Application to a KBES for Evaluating the Seismic Resistance of Existing Buildings," by E.G. Ibarra-Anaya and S.J. Fenves, 4/9/91, (PB91-210930, A08, MF-A01).

NCEER-91-0008   "Nonlinear Analysis of Steel Frames with Semi-Rigid Connections Using the Capacity Spectrum Method," by G.G. Deierlein, S-H. Hsieh, Y-J. Shen and J.F. Abel, 7/2/91, (PB92-113828, A05, MF-A01).

NCEER-91-0009   "Earthquake Education Materials for Grades K-12," by K.E.K. Ross, 4/30/91, (PB91-212142, A06, MF-A01). This report has been replaced by NCEER-92-0018.

NCEER-91-0010   "Phase Wave Velocities and Displacement Phase Differences in a Harmonically Oscillating Pile," by N. Makris and G. Gazetas, 7/8/91, (PB92-108356, A04, MF-A01).

NCEER-91-0011   "Dynamic Characteristics of a Full-Size Five-Story Steel Structure and a 2/5 Scale Model," by K.C. Chang, G.C. Yao, G.C. Lee, D.S. Hao and Y.C. Yeh," 7/2/91, (PB93-116648, A06, MF-A02).

NCEER-91-0012   "Seismic Response of a 2/5 Scale Steel Structure with Added Viscoelastic Dampers," by K.C. Chang, T.T. Soong, S-T. Oh and M.L. Lai, 5/17/91, (PB92-110816, A05, MF-A01).

NCEER-91-0013   "Earthquake Response of Retaining Walls; Full-Scale Testing and Computational Modeling," by S. Alampalli and A-W.M. Elgamal, 6/20/91, to be published.

NCEER-91-0014   "3D-BASIS-M: Nonlinear Dynamic Analysis of Multiple Building Base Isolated Structures," by P.C. Tsopelas, S. Nagarajaiah, M.C. Constantinou and A.M. Reinhorn, 5/28/91, (PB92-113885, A09, MF-A02).

NCEER-91-0015   "Evaluation of SEAOC Design Requirements for Sliding Isolated Structures," by D. Theodossiou and M.C. Constantinou, 6/10/91, (PB92-114602, A11, MF-A03).

NCEER-91-0016   "Closed-Loop Modal Testing of a 27-Story Reinforced Concrete Flat Plate-Core Building," by H.R. Somaprasad, T. Toksoy, H. Yoshiyuki and A.E. Aktan, 7/15/91, (PB92-129980, A07, MF-A02).

NCEER-91-0017   "Shake Table Test of a 1/6 Scale Two-Story Lightly Reinforced Concrete Building," by A.G. El-Attar, R.N. White and P. Gergely, 2/28/91, (PB92-222447, A06, MF-A02).

NCEER-91-0018   "Shake Table Test of a 1/8 Scale Three-Story Lightly Reinforced Concrete Building," by A.G. El-Attar, R.N. White and P. Gergely, 2/28/91, (PB93-116630, A08, MF-A02).

NCEER-91-0019   "Transfer Functions for Rigid Rectangular Foundations," by A.S. Veletsos, A.M. Prasad and W.H. Wu, 7/31/91, to be published.

NCEER-91-0020   "Hybrid Control of Seismic-Excited Nonlinear and Inelastic Structural Systems," by J.N. Yang, Z. Li and A. Danielians, 8/1/91, (PB92-143171, A06, MF-A02).

NCEER-91-0021   "The NCEER-91 Earthquake Catalog: Improved Intensity-Based Magnitudes and Recurrence Relations for U.S. Earthquakes East of New Madrid," by L. Seeber and J.G. Armbruster, 8/28/91, (PB92-176742, A06, MF-A02).

NCEER-91-0022   "Proceedings from the Implementation of Earthquake Planning and Education in Schools: The Need for Change - The Roles of the Changemakers," by K.E.K. Ross and F. Winslow, 7/23/91, (PB92-129998, A12, MF-A03).

NCEER-91-0023   "A Study of Reliability-Based Criteria for Seismic Design of Reinforced Concrete Frame Buildings," by H.H.M. Hwang and H-M. Hsu, 8/10/91, (PB92-140235, A09, MF-A02).

NCEER-91-0024   "Experimental Verification of a Number of Structural System Identification Algorithms," by R.G. Ghanem, H. Gavin and M. Shinozuka, 9/18/91, (PB92-176577, A18, MF-A04).

NCEER-91-0025   "Probabilistic Evaluation of Liquefaction Potential," by H.H.M. Hwang and C.S. Lee," 11/25/91, (PB92-143429, A05, MF-A01).

NCEER-91-0026   "Instantaneous Optimal Control for Linear, Nonlinear and Hysteretic Structures - Stable Controllers," by J.N. Yang and Z. Li, 11/15/91, (PB92-163807, A04, MF-A01).

NCEER-91-0027   "Experimental and Theoretical Study of a Sliding Isolation System for Bridges," by M.C. Constantinou, A. Kartoum, A.M. Reinhorn and P. Bradford, 11/15/91, (PB92-176973, A10, MF-A03).

NCEER-92-0001   "Case Studies of Liquefaction and Lifeline Performance During Past Earthquakes, Volume 1: Japanese Case Studies," Edited by M. Hamada and T. O'Rourke, 2/17/92, (PB92-197243, A18, MF-A04).

NCEER-92-0002   "Case Studies of Liquefaction and Lifeline Performance During Past Earthquakes, Volume 2: United States Case Studies," Edited by T. O'Rourke and M. Hamada, 2/17/92, (PB92-197250, A20, MF-A04).

NCEER-92-0003   "Issues in Earthquake Education," Edited by K. Ross, 2/3/92, (PB92-222389, A07, MF-A02).

NCEER-92-0004   "Proceedings from the First U.S. - Japan Workshop on Earthquake Protective Systems for Bridges," Edited by I.G. Buckle, 2/4/92, (PB94-142239, A99, MF-A06).

NCEER-92-0005   "Seismic Ground Motion from a Haskell-Type Source in a Multiple-Layered Half-Space," A.P. Theoharis, G. Deodatis and M. Shinozuka, 1/2/92, to be published.

NCEER-92-0006   "Proceedings from the Site Effects Workshop," Edited by R. Whitman, 2/29/92, (PB92-197201, A04, MF-A01).

NCEER-92-0007   "Engineering Evaluation of Permanent Ground Deformations Due to Seismically-Induced Liquefaction," by M.H. Baziar, R. Dobry and A-W.M. Elgamal, 3/24/92, (PB92-222421, A13, MF-A03).

NCEER-92-0008   "A Procedure for the Seismic Evaluation of Buildings in the Central and Eastern United States," by C.D. Poland and J.O. Malley, 4/2/92, (PB92-222439, A20, MF-A04).

NCEER-92-0009   "Experimental and Analytical Study of a Hybrid Isolation System Using Friction Controllable Sliding Bearings," by M.Q. Feng, S. Fujii and M. Shinozuka, 5/15/92, (PB93-150282, A06, MF-A02).

NCEER-92-0010   "Seismic Resistance of Slab-Column Connections in Existing Non-Ductile Flat-Plate Buildings," by A.J. Durrani and Y. Du, 5/18/92, (PB93-116812, A06, MF-A02).

NCEER-92-0011   "The Hysteretic and Dynamic Behavior of Brick Masonry Walls Upgraded by Ferrocement Coatings Under Cyclic Loading and Strong Simulated Ground Motion," by H. Lee and S.P. Prawel, 5/11/92, to be published.

NCEER-92-0012   "Study of Wire Rope Systems for Seismic Protection of Equipment in Buildings," by G.F. Demetriades, M.C. Constantinou and A.M. Reinhorn, 5/20/92, (PB93-116655, A08, MF-A02).

NCEER-92-0013   "Shape Memory Structural Dampers: Material Properties, Design and Seismic Testing," by P.R. Witting and F.A. Cozzarelli, 5/26/92, (PB93-116663, A05, MF-A01).

NCEER-92-0014   "Longitudinal Permanent Ground Deformation Effects on Buried Continuous Pipelines," by M.J. O'Rourke, and C. Nordberg, 6/15/92, (PB93-116671, A08, MF-A02).

NCEER-92-0015   "A Simulation Method for Stationary Gaussian Random Functions Based on the Sampling Theorem," by M. Grigoriu and S. Balopoulou, 6/11/92, (PB93-127496, A05, MF-A01).

NCEER-92-0016   "Gravity-Load-Designed Reinforced Concrete Buildings: Seismic Evaluation of Existing Construction and Detailing Strategies for Improved Seismic Resistance," by G.W. Hoffmann, S.K. Kunnath, A.M. Reinhorn and J.B. Mander, 7/15/92, (PB94-142007, A08, MF-A02).

NCEER-92-0017   "Observations on Water System and Pipeline Performance in the Limón Area of Costa Rica Due to the April 22, 1991 Earthquake," by M. O'Rourke and D. Ballantyne, 6/30/92, (PB93-126811, A06, MF-A02).

NCEER-92-0018   "Fourth Edition of Earthquake Education Materials for Grades K-12," Edited by K.E.K. Ross, 8/10/92, (PB93-114023, A07, MF-A02).

NCEER-92-0019   "Proceedings from the Fourth Japan-U.S. Workshop on Earthquake Resistant Design of Lifeline Facilities and Countermeasures for Soil Liquefaction," Edited by M. Hamada and T.D. O'Rourke, 8/12/92, (PB93-163939, A99, MF-E11).

NCEER-92-0020   "Active Bracing System: A Full Scale Implementation of Active Control," by A.M. Reinhorn, T.T. Soong, R.C. Lin, M.A. Riley, Y.P. Wang, S. Aizawa and M. Higashino, 8/14/92, (PB93-127512, A06, MF-A02).

NCEER-92-0021   "Empirical Analysis of Horizontal Ground Displacement Generated by Liquefaction-Induced Lateral Spreads," by S.F. Bartlett and T.L. Youd, 8/17/92, (PB93-188241, A06, MF-A02).

NCEER-92-0022   "IDARC Version 3.0: Inelastic Damage Analysis of Reinforced Concrete Structures," by S.K. Kunnath, A.M. Reinhorn and R.F. Lobo, 8/31/92, (PB93-227502, A07, MF-A02).

NCEER-92-0023   "A Semi-Empirical Analysis of Strong-Motion Peaks in Terms of Seismic Source, Propagation Path and Local Site Conditions, by M. Kamiyama, M.J. O'Rourke and R. Flores-Berrones, 9/9/92, (PB93-150266, A08, MF-A02).

NCEER-92-0024   "Seismic Behavior of Reinforced Concrete Frame Structures with Nonductile Details, Part I: Summary of Experimental Findings of Full Scale Beam-Column Joint Tests," by A. Beres, R.N. White and P. Gergely, 9/30/92, (PB93-227783, A05, MF-A01).

NCEER-92-0025   "Experimental Results of Repaired and Retrofitted Beam-Column Joint Tests in Lightly Reinforced Concrete Frame Buildings," by A. Beres, S. El-Borgi, R.N. White and P. Gergely, 10/29/92, (PB93-227791, A05, MF-A01).

NCEER-92-0026   "A Generalization of Optimal Control Theory: Linear and Nonlinear Structures," by J.N. Yang, Z. Li and S. Vongchavalitkul, 11/2/92, (PB93-188621, A05, MF-A01).

NCEER-92-0027   "Seismic Resistance of Reinforced Concrete Frame Structures Designed Only for Gravity Loads: Part I - Design and Properties of a One-Third Scale Model Structure," by J.M. Bracci, A.M. Reinhorn and J.B. Mander, 12/1/92, (PB94-104502, A08, MF-A02).

NCEER-92-0028   "Seismic Resistance of Reinforced Concrete Frame Structures Designed Only for Gravity Loads: Part II - Experimental Performance of Subassemblages," by L.E. Aycardi, J.B. Mander and A.M. Reinhorn, 12/1/92, (PB94-104510, A08, MF-A02).

NCEER-92-0029   "Seismic Resistance of Reinforced Concrete Frame Structures Designed Only for Gravity Loads: Part III - Experimental Performance and Analytical Study of a Structural Model," by J.M. Bracci, A.M. Reinhorn and J.B. Mander, 12/1/92, (PB93-227528, A09, MF-A01).

NCEER-92-0030 "Evaluation of Seismic Retrofit of Reinforced Concrete Frame Structures: Part I - Experimental Performance of Retrofitted Subassemblages," by D. Choudhuri, J.B. Mander and A.M. Reinhorn, 12/8/92, (PB93-198307, A07, MF-A02).

NCEER-92-0031 "Evaluation of Seismic Retrofit of Reinforced Concrete Frame Structures: Part II - Experimental Performance and Analytical Study of a Retrofitted Structural Model," by J.M. Bracci, A.M. Reinhorn and J.B. Mander, 12/8/92, (PB93-198315, A09, MF-A03).

NCEER-92-0032 "Experimental and Analytical Investigation of Seismic Response of Structures with Supplemental Fluid Viscous Dampers," by M.C. Constantinou and M.D. Symans, 12/21/92, (PB93-191435, A10, MF-A03). This report is available only through NTIS (see address given above).

NCEER-92-0033 "Reconnaissance Report on the Cairo, Egypt Earthquake of October 12, 1992," by M. Khater, 12/23/92, (PB93-188621, A03, MF-A01).

NCEER-92-0034 "Low-Level Dynamic Characteristics of Four Tall Flat-Plate Buildings in New York City," by H. Gavin, S. Yuan, J. Grossman, E. Pekelis and K. Jacob, 12/28/92, (PB93-188217, A07, MF-A02).

NCEER-93-0001 "An Experimental Study on the Seismic Performance of Brick-Infilled Steel Frames With and Without Retrofit," by J.B. Mander, B. Nair, K. Wojtkowski and J. Ma, 1/29/93, (PB93-227510, A07, MF-A02).

NCEER-93-0002 "Social Accounting for Disaster Preparedness and Recovery Planning," by S. Cole, E. Pantoja and V. Razak, 2/22/93, (PB94-142114, A12, MF-A03).

NCEER-93-0003 "Assessment of 1991 NEHRP Provisions for Nonstructural Components and Recommended Revisions," by T.T. Soong, G. Chen, Z. Wu, R-H. Zhang and M. Grigoriu, 3/1/93, (PB93-188639, A06, MF-A02).

NCEER-93-0004 "Evaluation of Static and Response Spectrum Analysis Procedures of SEAOC/UBC for Seismic Isolated Structures," by C.W. Winters and M.C. Constantinou, 3/23/93, (PB93-198299, A10, MF-A03).

NCEER-93-0005 "Earthquakes in the Northeast - Are We Ignoring the Hazard? A Workshop on Earthquake Science and Safety for Educators," edited by K.E.K. Ross, 4/2/93, (PB94-103066, A09, MF-A02).

NCEER-93-0006 "Inelastic Response of Reinforced Concrete Structures with Viscoelastic Braces," by R.F. Lobo, J.M. Bracci, K.L. Shen, A.M. Reinhorn and T.T. Soong, 4/5/93, (PB93-227486, A05, MF-A02).

NCEER-93-0007 "Seismic Testing of Installation Methods for Computers and Data Processing Equipment," by K. Kosar, T.T. Soong, K.L. Shen, J.A. HoLung and Y.K. Lin, 4/12/93, (PB93-198299, A07, MF-A02).

NCEER-93-0008 "Retrofit of Reinforced Concrete Frames Using Added Dampers," by A. Reinhorn, M. Constantinou and C. Li, to be published.

NCEER-93-0009 "Seismic Behavior and Design Guidelines for Steel Frame Structures with Added Viscoelastic Dampers," by K.C. Chang, M.L. Lai, T.T. Soong, D.S. Hao and Y.C. Yeh, 5/1/93, (PB94-141959, A07, MF-A02).

NCEER-93-0010 "Seismic Performance of Shear-Critical Reinforced Concrete Bridge Piers," by J.B. Mander, S.M. Waheed, M.T.A. Chaudhary and S.S. Chen, 5/12/93, (PB93-227494, A08, MF-A02).

NCEER-93-0011 "3D-BASIS-TABS: Computer Program for Nonlinear Dynamic Analysis of Three Dimensional Base Isolated Structures," by S. Nagarajaiah, C. Li, A.M. Reinhorn and M.C. Constantinou, 8/2/93, (PB94-141819, A09, MF-A02).

NCEER-93-0012 "Effects of Hydrocarbon Spills from an Oil Pipeline Break on Ground Water," by O.J. Helweg and H.H.M. Hwang, 8/3/93, (PB94-141942, A06, MF-A02).

NCEER-93-0013 "Simplified Procedures for Seismic Design of Nonstructural Components and Assessment of Current Code Provisions," by M.P. Singh, L.E. Suarez, E.E. Matheu and G.O. Maldonado, 8/4/93, (PB94-141827, A09, MF-A02).

NCEER-93-0014 "An Energy Approach to Seismic Analysis and Design of Secondary Systems," by G. Chen and T.T. Soong, 8/6/93, (PB94-142767, A11, MF-A03).

NCEER-93-0015   "Proceedings from School Sites: Becoming Prepared for Earthquakes - Commemorating the Third Anniversary of the Loma Prieta Earthquake," Edited by F.E. Winslow and K.E.K. Ross, 8/16/93, (PB94-154275, A16, MF-A02).

NCEER-93-0016   "Reconnaissance Report of Damage to Historic Monuments in Cairo, Egypt Following the October 12, 1992 Dahshur Earthquake," by D. Sykora, D. Look, G. Croci, E. Karaesmen and E. Karaesmen, 8/19/93, (PB94-142221, A08, MF-A02).

NCEER-93-0017   "The Island of Guam Earthquake of August 8, 1993," by S.W. Swan and S.K. Harris, 9/30/93, (PB94-141843, A04, MF-A01).

NCEER-93-0018   "Engineering Aspects of the October 12, 1992 Egyptian Earthquake," by A.W. Elgamal, M. Amer, K. Adalier and A. Abul-Fadl, 10/7/93, (PB94-141983, A05, MF-A01).

NCEER-93-0019   "Development of an Earthquake Motion Simulator and its Application in Dynamic Centrifuge Testing," by I. Krstelj, Supervised by J.H. Prevost, 10/23/93, (PB94-181773, A-10, MF-A03).

NCEER-93-0020   "NCEER-Taisei Corporation Research Program on Sliding Seismic Isolation Systems for Bridges: Experimental and Analytical Study of a Friction Pendulum System (FPS)," by M.C. Constantinou, P. Tsopelas, Y-S. Kim and S. Okamoto, 11/1/93, (PB94-142775, A08, MF-A02).

NCEER-93-0021   "Finite Element Modeling of Elastomeric Seismic Isolation Bearings," by L.J. Billings, Supervised by R. Shepherd, 11/8/93, to be published.

NCEER-93-0022   "Seismic Vulnerability of Equipment in Critical Facilities: Life-Safety and Operational Consequences," by K. Porter, G.S. Johnson, M.M. Zadeh, C. Scawthorn and S. Eder, 11/24/93, (PB94-181765, A16, MF-A03).

NCEER-93-0023   "Hokkaido Nansei-oki, Japan Earthquake of July 12, 1993, by P.I. Yanev and C.R. Scawthorn, 12/23/93, (PB94-181500, A07, MF-A01).

NCEER-94-0001   "An Evaluation of Seismic Serviceability of Water Supply Networks with Application to the San Francisco Auxiliary Water Supply System," by I. Markov, Supervised by M. Grigoriu and T. O'Rourke, 1/21/94, (PB94-204013, A07, MF-A02).

NCEER-94-0002   "NCEER-Taisei Corporation Research Program on Sliding Seismic Isolation Systems for Bridges: Experimental and Analytical Study of Systems Consisting of Sliding Bearings, Rubber Restoring Force Devices and Fluid Dampers," Volumes I and II, by P. Tsopelas, S. Okamoto, M.C. Constantinou, D. Ozaki and S. Fujii, 2/4/94, (PB94-181740, A09, MF-A02 and PB94-181757, A12, MF-A03).

NCEER-94-0003   "A Markov Model for Local and Global Damage Indices in Seismic Analysis," by S. Rahman and M. Grigoriu, 2/18/94, (PB94-206000, A12, MF-A03).

NCEER-94-0004   "Proceedings from the NCEER Workshop on Seismic Response of Masonry Infills," edited by D.P. Abrams, 3/1/94, (PB94-180783, A07, MF-A02).

NCEER-94-0005   "The Northridge, California Earthquake of January 17, 1994: General Reconnaissance Report," edited by J.D. Goltz, 3/11/94, (PB94-193943, A10, MF-A03).

NCEER-94-0006   "Seismic Energy Based Fatigue Damage Analysis of Bridge Columns: Part I - Evaluation of Seismic Capacity," by G.A. Chang and J.B. Mander, 3/14/94, (PB94-219185, A11, MF-A03).

NCEER-94-0007   "Seismic Isolation of Multi-Story Frame Structures Using Spherical Sliding Isolation Systems," by T.M. Al-Hussaini, V.A. Zayas and M.C. Constantinou, 3/17/94, (PB94-193745, A09, MF-A02).

NCEER-94-0008   "The Northridge, California Earthquake of January 17, 1994: Performance of Highway Bridges," edited by I.G. Buckle, 3/24/94, (PB94-193851, A06, MF-A02).

NCEER-94-0009   "Proceedings of the Third U.S.-Japan Workshop on Earthquake Protective Systems for Bridges," edited by I.G. Buckle and I. Friedland, 3/31/94, (PB94-195815, A99, MF-A06).

NCEER-94-0010 "3D-BASIS-ME: Computer Program for Nonlinear Dynamic Analysis of Seismically Isolated Single and Multiple Structures and Liquid Storage Tanks," by P.C. Tsopelas, M.C. Constantinou and A.M. Reinhorn, 4/12/94, (PB94-204922, A09, MF-A02).

NCEER-94-0011 "The Northridge, California Earthquake of January 17, 1994: Performance of Gas Transmission Pipelines," by T.D. O'Rourke and M.C. Palmer, 5/16/94, (PB94-204989, A05, MF-A01).

NCEER-94-0012 "Feasibility Study of Replacement Procedures and Earthquake Performance Related to Gas Transmission Pipelines," by T.D. O'Rourke and M.C. Palmer, 5/25/94, (PB94-206638, A09, MF-A02).

NCEER-94-0013 "Seismic Energy Based Fatigue Damage Analysis of Bridge Columns: Part II - Evaluation of Seismic Demand," by G.A. Chang and J.B. Mander, 6/1/94, (PB95-18106, A08, MF-A02).

NCEER-94-0014 "NCEER-Taisei Corporation Research Program on Sliding Seismic Isolation Systems for Bridges: Experimental and Analytical Study of a System Consisting of Sliding Bearings and Fluid Restoring Force/Damping Devices," by P. Tsopelas and M.C. Constantinou, 6/13/94, (PB94-219144, A10, MF-A03).

NCEER-94-0015 "Generation of Hazard-Consistent Fragility Curves for Seismic Loss Estimation Studies," by H. Hwang and J-R. Huo, 6/14/94, (PB95-181996, A09, MF-A02).

NCEER-94-0016 "Seismic Study of Building Frames with Added Energy-Absorbing Devices," by W.S. Pong, C.S. Tsai and G.C. Lee, 6/20/94, (PB94-219136, A10, A03).

NCEER-94-0017 "Sliding Mode Control for Seismic-Excited Linear and Nonlinear Civil Engineering Structures," by J. Yang, J. Wu, A. Agrawal and Z. Li, 6/21/94, (PB95-138483, A06, MF-A02).

NCEER-94-0018 "3D-BASIS-TABS Version 2.0: Computer Program for Nonlinear Dynamic Analysis of Three Dimensional Base Isolated Structures," by A.M. Reinhorn, S. Nagarajaiah, M.C. Constantinou, P. Tsopelas and R. Li, 6/22/94, (PB95-182176, A08, MF-A02).

NCEER-94-0019 "Proceedings of the International Workshop on Civil Infrastructure Systems: Application of Intelligent Systems and Advanced Materials on Bridge Systems," Edited by G.C. Lee and K.C. Chang, 7/18/94, (PB95-252474, A20, MF-A04).

NCEER-94-0020 "Study of Seismic Isolation Systems for Computer Floors," by V. Lambrou and M.C. Constantinou, 7/19/94, (PB95-138533, A10, MF-A03).

NCEER-94-0021 "Proceedings of the U.S.-Italian Workshop on Guidelines for Seismic Evaluation and Rehabilitation of Unreinforced Masonry Buildings," Edited by D.P. Abrams and G.M. Calvi, 7/20/94, (PB95-138749, A13, MF-A03).

NCEER-94-0022 "NCEER-Taisei Corporation Research Program on Sliding Seismic Isolation Systems for Bridges: Experimental and Analytical Study of a System Consisting of Lubricated PTFE Sliding Bearings and Mild Steel Dampers," by P. Tsopelas and M.C. Constantinou, 7/22/94, (PB95-182184, A08, MF-A02).

NCEER-94-0023 "Development of Reliability-Based Design Criteria for Buildings Under Seismic Load," by Y.K. Wen, H. Hwang and M. Shinozuka, 8/1/94, (PB95-211934, A08, MF-A02).

NCEER-94-0024 "Experimental Verification of Acceleration Feedback Control Strategies for an Active Tendon System," by S.J. Dyke, B.F. Spencer, Jr., P. Quast, M.K. Sain, D.C. Kaspari, Jr. and T.T. Soong, 8/29/94, (PB95-212320, A05, MF-A01).

NCEER-94-0025 "Seismic Retrofitting Manual for Highway Bridges," Edited by I.G. Buckle and I.F. Friedland, published by the Federal Highway Administration (PB95-212676, A15, MF-A03).

NCEER-94-0026 "Proceedings from the Fifth U.S.-Japan Workshop on Earthquake Resistant Design of Lifeline Facilities and Countermeasures Against Soil Liquefaction," Edited by T.D. O'Rourke and M. Hamada, 11/7/94, (PB95-220802, A99, MF-E08).

NCEER-95-0001 "Experimental and Analytical Investigation of Seismic Retrofit of Structures with Supplemental Damping: Part 1 - Fluid Viscous Damping Devices," by A.M. Reinhorn, C. Li and M.C. Constantinou, 1/3/95, (PB95-266599, A09, MF-A02).

NCEER-95-0002 "Experimental and Analytical Study of Low-Cycle Fatigue Behavior of Semi-Rigid Top-And-Seat Angle Connections," by G. Pekcan, J.B. Mander and S.S. Chen, 1/5/95, (PB95-220042, A07, MF-A02).

NCEER-95-0003 "NCEER-ATC Joint Study on Fragility of Buildings," by T. Anagnos, C. Rojahn and A.S. Kiremidjian, 1/20/95, (PB95-220026, A06, MF-A02).

NCEER-95-0004 "Nonlinear Control Algorithms for Peak Response Reduction," by Z. Wu, T.T. Soong, V. Gattulli and R.C. Lin, 2/16/95, (PB95-220349, A05, MF-A01).

NCEER-95-0005 "Pipeline Replacement Feasibility Study: A Methodology for Minimizing Seismic and Corrosion Risks to Underground Natural Gas Pipelines," by R.T. Eguchi, H.A. Seligson and D.G. Honegger, 3/2/95, (PB95-252326, A06, MF-A02).

NCEER-95-0006 "Evaluation of Seismic Performance of an 11-Story Frame Building During the 1994 Northridge Earthquake," by F. Naeim, R. DiSulio, K. Benuska, A. Reinhorn and C. Li, to be published.

NCEER-95-0007 "Prioritization of Bridges for Seismic Retrofitting," by N. Basöz and A.S. Kiremidjian, 4/24/95, (PB95-252300, A08, MF-A02).

NCEER-95-0008 "Method for Developing Motion Damage Relationships for Reinforced Concrete Frames," by A. Singhal and A.S. Kiremidjian, 5/11/95, (PB95-266607, A06, MF-A02).

NCEER-95-0009 "Experimental and Analytical Investigation of Seismic Retrofit of Structures with Supplemental Damping: Part II - Friction Devices," by C. Li and A.M. Reinhorn, 7/6/95, (PB96-128087, A11, MF-A03).

NCEER-95-0010 "Experimental Performance and Analytical Study of a Non-Ductile Reinforced Concrete Frame Structure Retrofitted with Elastomeric Spring Dampers," by G. Pekcan, J.B. Mander and S.S. Chen, 7/14/95, (PB96-137161, A08, MF-A02).

NCEER-95-0011 "Development and Experimental Study of Semi-Active Fluid Damping Devices for Seismic Protection of Structures," by M.D. Symans and M.C. Constantinou, 8/3/95, (PB96-136940, A23, MF-A04).

NCEER-95-0012 "Real-Time Structural Parameter Modification (RSPM): Development of Innervated Structures," by Z. Liang, M. Tong and G.C. Lee, 4/11/95, (PB96-137153, A06, MF-A01).

NCEER-95-0013 "Experimental and Analytical Investigation of Seismic Retrofit of Structures with Supplemental Damping: Part III - Viscous Damping Walls," by A.M. Reinhorn and C. Li, 10/1/95, (PB96-176409, A11, MF-A03).

NCEER-95-0014 "Seismic Fragility Analysis of Equipment and Structures in a Memphis Electric Substation," by J-R. Huo and H.H.M. Hwang, 8/10/95, (PB96-128087, A09, MF-A02).

NCEER-95-0015 "The Hanshin-Awaji Earthquake of January 17, 1995: Performance of Lifelines," Edited by M. Shinozuka, 11/3/95, (PB96-176383, A15, MF-A03).

NCEER-95-0016 "Highway Culvert Performance During Earthquakes," by T.L. Youd and C.J. Beckman, available as NCEER-96-0015.

NCEER-95-0017 "The Hanshin-Awaji Earthquake of January 17, 1995: Performance of Highway Bridges," Edited by I.G. Buckle, 12/1/95, to be published.

NCEER-95-0018 "Modeling of Masonry Infill Panels for Structural Analysis," by A.M. Reinhorn, A. Madan, R.E. Valles, Y. Reichmann and J.B. Mander, 12/8/95, (PB97-110886, MF-A01, A06).

NCEER-95-0019 "Optimal Polynomial Control for Linear and Nonlinear Structures," by A.K. Agrawal and J.N. Yang, 12/11/95, (PB96-168737, A07, MF-A02).

NCEER-95-0020   "Retrofit of Non-Ductile Reinforced Concrete Frames Using Friction Dampers," by R.S. Rao, P. Gergely and R.N. White, 12/22/95, (PB97-133508, A10, MF-A02).

NCEER-95-0021   "Parametric Results for Seismic Response of Pile-Supported Bridge Bents," by G. Mylonakis, A. Nikolaou and G. Gazetas, 12/22/95, (PB97-100242, A12, MF-A03).

NCEER-95-0022   "Kinematic Bending Moments in Seismically Stressed Piles," by A. Nikolaou, G. Mylonakis and G. Gazetas, 12/23/95, (PB97-113914, MF-A03, A13).

NCEER-96-0001   "Dynamic Response of Unreinforced Masonry Buildings with Flexible Diaphragms," by A.C. Costley and D.P. Abrams," 10/10/96, (PB97-133573, MF-A03, A15).

NCEER-96-0002   "State of the Art Review: Foundations and Retaining Structures," by I. Po Lam, to be published.

NCEER-96-0003   "Ductility of Rectangular Reinforced Concrete Bridge Columns with Moderate Confinement," by N. Wehbe, M. Saiidi, D. Sanders and B. Douglas, 11/7/96, (PB97-133557, A06, MF-A02).

NCEER-96-0004   "Proceedings of the Long-Span Bridge Seismic Research Workshop," edited by I.G. Buckle and I.M. Friedland, to be published.

NCEER-96-0005   "Establish Representative Pier Types for Comprehensive Study: Eastern United States," by J. Kulicki and Z. Prucz, 5/28/96, (PB98-119217, A07, MF-A02).

NCEER-96-0006   "Establish Representative Pier Types for Comprehensive Study: Western United States," by R. Imbsen, R.A. Schamber and T.A. Osterkamp, 5/28/96, (PB98-118607, A07, MF-A02).

NCEER-96-0007   "Nonlinear Control Techniques for Dynamical Systems with Uncertain Parameters," by R.G. Ghanem and M.I. Bujakov, 5/27/96, (PB97-100259, A17, MF-A03).

NCEER-96-0008   "Seismic Evaluation of a 30-Year Old Non-Ductile Highway Bridge Pier and Its Retrofit," by J.B. Mander, B. Mahmoodzadegan, S. Bhadra and S.S. Chen, 5/31/96, (PB97-110902, MF-A03, A10).

NCEER-96-0009   "Seismic Performance of a Model Reinforced Concrete Bridge Pier Before and After Retrofit," by J.B. Mander, J.H. Kim and C.A. Ligozio, 5/31/96, (PB97-110910, MF-A02, A10).

NCEER-96-0010   "IDARC2D Version 4.0: A Computer Program for the Inelastic Damage Analysis of Buildings," by R.E. Valles, A.M. Reinhorn, S.K. Kunnath, C. Li and A. Madan, 6/3/96, (PB97-100234, A17, MF-A03).

NCEER-96-0011   "Estimation of the Economic Impact of Multiple Lifeline Disruption: Memphis Light, Gas and Water Division Case Study," by S.E. Chang, H.A. Seligson and R.T. Eguchi, 8/16/96, (PB97-133490, A11, MF-A03).

NCEER-96-0012   "Proceedings from the Sixth Japan-U.S. Workshop on Earthquake Resistant Design of Lifeline Facilities and Countermeasures Against Soil Liquefaction, Edited by M. Hamada and T. O'Rourke, 9/11/96, (PB97-133581, A99, MF-A06).

NCEER-96-0013   "Chemical Hazards, Mitigation and Preparedness in Areas of High Seismic Risk: A Methodology for Estimating the Risk of Post-Earthquake Hazardous Materials Release," by H.A. Seligson, R.T. Eguchi, K.J. Tierney and K. Richmond, 11/7/96, (PB97-133565, MF-A02, A08).

NCEER-96-0014   "Response of Steel Bridge Bearings to Reversed Cyclic Loading," by J.B. Mander, D-K. Kim, S.S. Chen and G.J. Premus, 11/13/96, (PB97-140735, A12, MF-A03).

NCEER-96-0015   "Highway Culvert Performance During Past Earthquakes," by T.L. Youd and C.J. Beckman, 11/25/96, (PB97-133532, A06, MF-A01).

NCEER-97-0001   "Evaluation, Prevention and Mitigation of Pounding Effects in Building Structures," by R.E. Valles and A.M. Reinhorn, 2/20/97, (PB97-159552, A14, MF-A03).

NCEER-97-0002   "Seismic Design Criteria for Bridges and Other Highway Structures," by C. Rojahn, R. Mayes, D.G. Anderson, J. Clark, J.H. Hom, R.V. Nutt and M.J. O'Rourke, 4/30/97, (PB97-194658, A06, MF-A03).

NCEER-97-0003   "Proceedings of the U.S.-Italian Workshop on Seismic Evaluation and Retrofit," Edited by D.P. Abrams and G.M. Calvi, 3/19/97, (PB97-194666, A13, MF-A03).

NCEER-97-0004   "Investigation of Seismic Response of Buildings with Linear and Nonlinear Fluid Viscous Dampers," by A.A. Seleemah and M.C. Constantinou, 5/21/97, (PB98-109002, A15, MF-A03).

NCEER-97-0005   "Proceedings of the Workshop on Earthquake Engineering Frontiers in Transportation Facilities," edited by G.C. Lee and I.M. Friedland, 8/29/97, (PB98-128911, A25, MR-A04).

NCEER-97-0006   "Cumulative Seismic Damage of Reinforced Concrete Bridge Piers," by S.K. Kunnath, A. El-Bahy, A. Taylor and W. Stone, 9/2/97, (PB98-108814, A11, MF-A03).

NCEER-97-0007   "Structural Details to Accommodate Seismic Movements of Highway Bridges and Retaining Walls," by R.A. Imbsen, R.A. Schamber, E. Thorkildsen, A. Kartoum, B.T. Martin, T.N. Rosser and J.M. Kulicki, 9/3/97, (PB98-108996, A09, MF-A02).

NCEER-97-0008   "A Method for Earthquake Motion-Damage Relationships with Application to Reinforced Concrete Frames," by A. Singhal and A.S. Kiremidjian, 9/10/97, (PB98-108988, A13, MF-A03).

NCEER-97-0009   "Seismic Analysis and Design of Bridge Abutments Considering Sliding and Rotation," by K. Fishman and R. Richards, Jr., 9/15/97, (PB98-108897, A06, MF-A02).

NCEER-97-0010   "Proceedings of the FHWA/NCEER Workshop on the National Representation of Seismic Ground Motion for New and Existing Highway Facilities," edited by I.M. Friedland, M.S. Power and R.L. Mayes, 9/22/97, (PB98-128903, A21, MF-A04).

NCEER-97-0011   "Seismic Analysis for Design or Retrofit of Gravity Bridge Abutments," by K.L. Fishman, R. Richards, Jr. and R.C. Divito, 10/2/97, (PB98-128937, A08, MF-A02).

NCEER-97-0012   "Evaluation of Simplified Methods of Analysis for Yielding Structures," by P. Tsopelas, M.C. Constantinou, C.A. Kircher and A.S. Whittaker, 10/31/97, (PB98-128929, A10, MF-A03).

NCEER-97-0013   "Seismic Design of Bridge Columns Based on Control and Repairability of Damage," by C-T. Cheng and J.B. Mander, 12/8/97, (PB98-144249, A11, MF-A03).

NCEER-97-0014   "Seismic Resistance of Bridge Piers Based on Damage Avoidance Design," by J.B. Mander and C-T. Cheng, 12/10/97, (PB98-144223, A09, MF-A02).

NCEER-97-0015   "Seismic Response of Nominally Symmetric Systems with Strength Uncertainty," by S. Balopoulou and M. Grigoriu, 12/23/97, (PB98-153422, A11, MF-A03).

NCEER-97-0016   "Evaluation of Seismic Retrofit Methods for Reinforced Concrete Bridge Columns," by T.J. Wipf, F.W. Klaiber and F.M. Russo, 12/28/97, (PB98-144215, A12, MF-A03).

NCEER-97-0017   "Seismic Fragility of Existing Conventional Reinforced Concrete Highway Bridges," by C.L. Mullen and A.S. Cakmak, 12/30/97, (PB98-153406, A08, MF-A02).

NCEER-97-0018   "Loss Asssessment of Memphis Buildings," edited by D.P. Abrams and M. Shinozuka, 12/31/97, (PB98-144231, A13, MF-A03).

NCEER-97-0019   "Seismic Evaluation of Frames with Infill Walls Using Quasi-static Experiments," by K.M. Mosalam, R.N. White and P. Gergely, 12/31/97, (PB98-153455, A07, MF-A02).

NCEER-97-0020   "Seismic Evaluation of Frames with Infill Walls Using Pseudo-dynamic Experiments," by K.M. Mosalam, R.N. White and P. Gergely, 12/31/97, (PB98-153430, A07, MF-A02).

NCEER-97-0021   "Computational Strategies for Frames with Infill Walls: Discrete and Smeared Crack Analyses and Seismic Fragility," by K.M. Mosalam, R.N. White and P. Gergely, 12/31/97, (PB98-153414, A10, MF-A02).

NCEER-97-0022   "Proceedings of the NCEER Workshop on Evaluation of Liquefaction Resistance of Soils," edited by T.L. Youd and I.M. Idriss, 12/31/97, (PB98-155617, A15, MF-A03).

MCEER-98-0001   "Extraction of Nonlinear Hysteretic Properties of Seismically Isolated Bridges from Quick-Release Field Tests," by Q. Chen, B.M. Douglas, E.M. Maragakis and I.G. Buckle, 5/26/98, (PB99-118838, A06, MF-A01).

MCEER-98-0002   "Methodologies for Evaluating the Importance of Highway Bridges," by A. Thomas, S. Eshenaur and J. Kulicki, 5/29/98, (PB99-118846, A10, MF-A02).

MCEER-98-0003   "Capacity Design of Bridge Piers and the Analysis of Overstrength," by J.B. Mander, A. Dutta and P. Goel, 6/1/98, (PB99-118853, A09, MF-A02).

MCEER-98-0004   "Evaluation of Bridge Damage Data from the Loma Prieta and Northridge, California Earthquakes," by N. Basoz and A. Kiremidjian, 6/2/98, (PB99-118861, A15, MF-A03).

MCEER-98-0005   "Screening Guide for Rapid Assessment of Liquefaction Hazard at Highway Bridge Sites," by T. L. Youd, 6/16/98, (PB99-118879, A06, not available on microfiche).

MCEER-98-0006   "Structural Steel and Steel/Concrete Interface Details for Bridges," by P. Ritchie, N. Kauhl and J. Kulicki, 7/13/98, (PB99-118945, A06, MF-A01).

MCEER-98-0007   "Capacity Design and Fatigue Analysis of Confined Concrete Columns," by A. Dutta and J.B. Mander, 7/14/98, (PB99-118960, A14, MF-A03).

MCEER-98-0008   "Proceedings of the Workshop on Performance Criteria for Telecommunication Services Under Earthquake Conditions," edited by A.J. Schiff, 7/15/98, (PB99-118952, A08, MF-A02).

MCEER-98-0009   "Fatigue Analysis of Unconfined Concrete Columns," by J.B. Mander, A. Dutta and J.H. Kim, 9/12/98, (PB99-123655, A10, MF-A02).

MCEER-98-0010   "Centrifuge Modeling of Cyclic Lateral Response of Pile-Cap Systems and Seat-Type Abutments in Dry Sands," by A.D. Gadre and R. Dobry, 10/2/98, (PB99-123606, A13, MF-A03).

MCEER-98-0011   "IDARC-BRIDGE: A Computational Platform for Seismic Damage Assessment of Bridge Structures," by A.M. Reinhorn, V. Simeonov, G. Mylonakis and Y. Reichman, 10/2/98, (PB99-162919, A15, MF-A03).

MCEER-98-0012   "Experimental Investigation of the Dynamic Response of Two Bridges Before and After Retrofitting with Elastomeric Bearings," by D.A. Wendichansky, S.S. Chen and J.B. Mander, 10/2/98, (PB99-162927, A15, MF-A03).

MCEER-98-0013   "Design Procedures for Hinge Restrainers and Hinge Sear Width for Multiple-Frame Bridges," by R. Des Roches and G.L. Fenves, 11/3/98, (PB99-140477, A13, MF-A03).

MCEER-98-0014   "Response Modification Factors for Seismically Isolated Bridges," by M.C. Constantinou and J.K. Quarshie, 11/3/98, (PB99-140485, A14, MF-A03).

MCEER-98-0015   "Proceedings of the U.S.-Italy Workshop on Seismic Protective Systems for Bridges," edited by I.M. Friedland and M.C. Constantinou, 11/3/98, (PB2000-101711, A22, MF-A04).

MCEER-98-0016   "Appropriate Seismic Reliability for Critical Equipment Systems: Recommendations Based on Regional Analysis of Financial and Life Loss," by K. Porter, C. Scawthorn, C. Taylor and N. Blais, 11/10/98, (PB99-157265, A08, MF-A02).

MCEER-98-0017   "Proceedings of the U.S. Japan Joint Seminar on Civil Infrastructure Systems Research," edited by M. Shinozuka and A. Rose, 11/12/98, (PB99-156713, A16, MF-A03).

MCEER-98-0018   "Modeling of Pile Footings and Drilled Shafts for Seismic Design," by I. PoLam, M. Kapuskar and D. Chaudhuri, 12/21/98, (PB99-157257, A09, MF-A02).

MCEER-99-0001   "Seismic Evaluation of a Masonry Infilled Reinforced Concrete Frame by Pseudodynamic Testing," by S.G. Buonopane and R.N. White, 2/16/99, (PB99-162851, A09, MF-A02).

MCEER-99-0002   "Response History Analysis of Structures with Seismic Isolation and Energy Dissipation Systems: Verification Examples for Program SAP2000," by J. Scheller and M.C. Constantinou, 2/22/99, (PB99-162869, A08, MF-A02).

MCEER-99-0003   "Experimental Study on the Seismic Design and Retrofit of Bridge Columns Including Axial Load Effects," by A. Dutta, T. Kokorina and J.B. Mander, 2/22/99, (PB99-162877, A09, MF-A02).

MCEER-99-0004   "Experimental Study of Bridge Elastomeric and Other Isolation and Energy Dissipation Systems with Emphasis on Uplift Prevention and High Velocity Near-source Seismic Excitation," by A. Kasalanati and M. C. Constantinou, 2/26/99, (PB99-162885, A12, MF-A03).

MCEER-99-0005   "Truss Modeling of Reinforced Concrete Shear-flexure Behavior," by J.H. Kim and J.B. Mander, 3/8/99, (PB99-163693, A12, MF-A03).

MCEER-99-0006   "Experimental Investigation and Computational Modeling of Seismic Response of a 1:4 Scale Model Steel Structure with a Load Balancing Supplemental Damping System," by G. Pekcan, J.B. Mander and S.S. Chen, 4/2/99, (PB99-162893, A11, MF-A03).

MCEER-99-0007   "Effect of Vertical Ground Motions on the Structural Response of Highway Bridges," by M.R. Button, C.J. Cronin and R.L. Mayes, 4/10/99, (PB2000-101411, A10, MF-A03).

MCEER-99-0008   "Seismic Reliability Assessment of Critical Facilities: A Handbook, Supporting Documentation, and Model Code Provisions," by G.S. Johnson, R.E. Sheppard, M.D. Quilici, S.J. Eder and C.R. Scawthorn, 4/12/99, (PB2000-101701, A18, MF-A04).

MCEER-99-0009   "Impact Assessment of Selected MCEER Highway Project Research on the Seismic Design of Highway Structures," by C. Rojahn, R. Mayes, D.G. Anderson, J.H. Clark, D'Appolonia Engineering, S. Gloyd and R.V. Nutt, 4/14/99, (PB99-162901, A10, MF-A02).

MCEER-99-0010   "Site Factors and Site Categories in Seismic Codes," by R. Dobry, R. Ramos and M.S. Power, 7/19/99, (PB2000-101705, A08, MF-A02).

MCEER-99-0011   "Restrainer Design Procedures for Multi-Span Simply-Supported Bridges," by M.J. Randall, M. Saiidi, E. Maragakis and T. Isakovic, 7/20/99, (PB2000-101702, A10, MF-A02).

MCEER-99-0012   "Property Modification Factors for Seismic Isolation Bearings," by M.C. Constantinou, P. Tsopelas, A. Kasalanati and E. Wolff, 7/20/99, (PB2000-103387, A11, MF-A03).

MCEER-99-0013   "Critical Seismic Issues for Existing Steel Bridges," by P. Ritchie, N. Kauhl and J. Kulicki, 7/20/99, (PB2000-101697, A09, MF-A02).

MCEER-99-0014   "Nonstructural Damage Database," by A. Kao, T.T. Soong and A. Vender, 7/24/99, (PB2000-101407, A06, MF-A01).

MCEER-99-0015   "Guide to Remedial Measures for Liquefaction Mitigation at Existing Highway Bridge Sites," by H.G. Cooke and J. K. Mitchell, 7/26/99, (PB2000-101703, A11, MF-A03).

MCEER-99-0016   "Proceedings of the MCEER Workshop on Ground Motion Methodologies for the Eastern United States," edited by N. Abrahamson and A. Becker, 8/11/99, (PB2000-103385, A07, MF-A02).

MCEER-99-0017   "Quindío, Colombia Earthquake of January 25, 1999: Reconnaissance Report," by A.P. Asfura and P.J. Flores, 10/4/99, (PB2000-106893, A06, MF-A01).

MCEER-99-0018   "Hysteretic Models for Cyclic Behavior of Deteriorating Inelastic Structures," by M.V. Sivaselvan and A.M. Reinhorn, 11/5/99, (PB2000-103386, A08, MF-A02).

MCEER-99-0019   "Proceedings of the 7th U.S.- Japan Workshop on Earthquake Resistant Design of Lifeline Facilities and Countermeasures Against Soil Liquefaction," edited by T.D. O'Rourke, J.P. Bardet and M. Hamada, 11/19/99, (PB2000-103354, A99, MF-A06).

MCEER-99-0020   "Development of Measurement Capability for Micro-Vibration Evaluations with Application to Chip Fabrication Facilities," by G.C. Lee, Z. Liang, J.W. Song, J.D. Shen and W.C. Liu, 12/1/99, (PB2000-105993, A08, MF-A02).

MCEER-99-0021   "Design and Retrofit Methodology for Building Structures with Supplemental Energy Dissipating Systems," by G. Pekcan, J.B. Mander and S.S. Chen, 12/31/99, (PB2000-105994, A11, MF-A03).

MCEER-00-0001   "The Marmara, Turkey Earthquake of August 17, 1999: Reconnaissance Report," edited by C. Scawthorn; with major contributions by M. Bruneau, R. Eguchi, T. Holzer, G. Johnson, J. Mander, J. Mitchell, W. Mitchell, A. Papageorgiou, C. Scaethorn, and G. Webb, 3/23/00, (PB2000-106200, A11, MF-A03).

MCEER-00-0002   "Proceedings of the MCEER Workshop for Seismic Hazard Mitigation of Health Care Facilities," edited by G.C. Lee, M. Ettouney, M. Grigoriu, J. Hauer and J. Nigg, 3/29/00, (PB2000-106892, A08, MF-A02).

MCEER-00-0003   "The Chi-Chi, Taiwan Earthquake of September 21, 1999: Reconnaissance Report," edited by G.C. Lee and C.H. Loh, with major contributions by G.C. Lee, M. Bruneau, I.G. Buckle, S.E. Chang, P.J. Flores, T.D. O'Rourke, M. Shinozuka, T.T. Soong, C-H. Loh, K-C. Chang, Z-J. Chen, J-S. Hwang, M-L. Lin, G-Y. Liu, K-C. Tsai, G.C. Yao and C-L. Yen, 4/30/00, (PB2001-100980, A10, MF-A02).

MCEER-00-0004   "Seismic Retrofit of End-Sway Frames of Steel Deck-Truss Bridges with a Supplemental Tendon System: Experimental and Analytical Investigation," by G. Pekcan, J.B. Mander and S.S. Chen, 7/1/00, (PB2001-100982, A10, MF-A02).

MCEER-00-0005   "Sliding Fragility of Unrestrained Equipment in Critical Facilities," by W.H. Chong and T.T. Soong, 7/5/00, (PB2001-100983, A08, MF-A02).

MCEER-00-0006   "Seismic Response of Reinforced Concrete Bridge Pier Walls in the Weak Direction," by N. Abo-Shadi, M. Saiidi and D. Sanders, 7/17/00, (PB2001-100981, A17, MF-A03).

MCEER-00-0007   "Low-Cycle Fatigue Behavior of Longitudinal Reinforcement in Reinforced Concrete Bridge Columns," by J. Brown and S.K. Kunnath, 7/23/00, (PB2001-104392, A08, MF-A02).

MCEER-00-0008   "Soil Structure Interaction of Bridges for Seismic Analysis," I. PoLam and H. Law, 9/25/00, (PB2001-105397, A08, MF-A02).

MCEER-00-0009   "Proceedings of the First MCEER Workshop on Mitigation of Earthquake Disaster by Advanced Technologies (MEDAT-1), edited by M. Shinozuka, D.J. Inman and T.D. O'Rourke, 11/10/00, (PB2001-105399, A14, MF-A03).

MCEER-00-0010   "Development and Evaluation of Simplified Procedures for Analysis and Design of Buildings with Passive Energy Dissipation Systems, Revision 01," by O.M. Ramirez, M.C. Constantinou, C.A. Kircher, A.S. Whittaker, M.W. Johnson, J.D. Gomez and C. Chrysostomou, 11/16/01, (PB2001-105523, A23, MF-A04).

MCEER-00-0011   "Dynamic Soil-Foundation-Structure Interaction Analyses of Large Caissons," by C-Y. Chang, C-M. Mok, Z-L. Wang, R. Settgast, F. Waggoner, M.A. Ketchum, H.M. Gonnermann and C-C. Chin, 12/30/00, (PB2001-104373, A07, MF-A02).

MCEER-00-0012   "Experimental Evaluation of Seismic Performance of Bridge Restrainers," by A.G. Vlassis, E.M. Maragakis and M. Saiid Saiidi, 12/30/00, (PB2001-104354, A09, MF-A02).

MCEER-00-0013   "Effect of Spatial Variation of Ground Motion on Highway Structures," by M. Shinozuka, V. Saxena and G. Deodatis, 12/31/00, (PB2001-108755, A13, MF-A03).

MCEER-00-0014   "A Risk-Based Methodology for Assessing the Seismic Performance of Highway Systems," by S.D. Werner, C.E. Taylor, J.E. Moore, II, J.S. Walton and S. Cho, 12/31/00, (PB2001-108756, A14, MF-A03).

MCEER-01-0001 "Experimental Investigation of P-Delta Effects to Collapse During Earthquakes," by D. Vian and M. Bruneau, 6/25/01, (PB2002-100534, A17, MF-A03).

MCEER-01-0002 "Proceedings of the Second MCEER Workshop on Mitigation of Earthquake Disaster by Advanced Technologies (MEDAT-2)," edited by M. Bruneau and D.J. Inman, 7/23/01, (PB2002-100434, A16, MF-A03).

MCEER-01-0003 "Sensitivity Analysis of Dynamic Systems Subjected to Seismic Loads," by C. Roth and M. Grigoriu, 9/18/01, (PB2003-100884, A12, MF-A03).

MCEER-01-0004 "Overcoming Obstacles to Implementing Earthquake Hazard Mitigation Policies: Stage 1 Report," by D.J. Alesch and W.J. Petak, 12/17/01, (PB2002-107949, A07, MF-A02).

MCEER-01-0005 "Updating Real-Time Earthquake Loss Estimates: Methods, Problems and Insights," by C.E. Taylor, S.E. Chang and R.T. Eguchi, 12/17/01, (PB2002-107948, A05, MF-A01).

MCEER-01-0006 "Experimental Investigation and Retrofit of Steel Pile Foundations and Pile Bents Under Cyclic Lateral Loadings," by A. Shama, J. Mander, B. Blabac and S. Chen, 12/31/01, (PB2002-107950, A13, MF-A03).

MCEER-02-0001 "Assessment of Performance of Bolu Viaduct in the 1999 Duzce Earthquake in Turkey" by P.C. Roussis, M.C. Constantinou, M. Erdik, E. Durukal and M. Dicleli, 5/8/02, (PB2003-100883, A08, MF-A02).

MCEER-02-0002 "Seismic Behavior of Rail Counterweight Systems of Elevators in Buildings," by M.P. Singh, Rildova and L.E. Suarez, 5/27/02. (PB2003-100882, A11, MF-A03).

MCEER-02-0003 "Development of Analysis and Design Procedures for Spread Footings," by G. Mylonakis, G. Gazetas, S. Nikolaou and A. Chauncey, 10/02/02, (PB2004-101636, A13, MF-A03, CD-A13).

MCEER-02-0004 "Bare-Earth Algorithms for Use with SAR and LIDAR Digital Elevation Models," by C.K. Huyck, R.T. Eguchi and B. Houshmand, 10/16/02, (PB2004-101637, A07, CD-A07).

MCEER-02-0005 "Review of Energy Dissipation of Compression Members in Concentrically Braced Frames," by K.Lee and M. Bruneau, 10/18/02, (PB2004-101638, A10, CD-A10).

MCEER-03-0001 "Experimental Investigation of Light-Gauge Steel Plate Shear Walls for the Seismic Retrofit of Buildings" by J. Berman and M. Bruneau, 5/2/03, (PB2004-101622, A10, MF-A03, CD-A10).

MCEER-03-0002 "Statistical Analysis of Fragility Curves," by M. Shinozuka, M.Q. Feng, H. Kim, T. Uzawa and T. Ueda, 6/16/03, (PB2004-101849, A09, CD-A09).

MCEER-03-0003 "Proceedings of the Eighth U.S.-Japan Workshop on Earthquake Resistant Design f Lifeline Facilities and Countermeasures Against Liquefaction," edited by M. Hamada, J.P. Bardet and T.D. O'Rourke, 6/30/03, (PB2004-104386, A99, CD-A99).

MCEER-03-0004 "Proceedings of the PRC-US Workshop on Seismic Analysis and Design of Special Bridges," edited by L.C. Fan and G.C. Lee, 7/15/03, (PB2004-104387, A14, CD-A14).

MCEER-03-0005 "Urban Disaster Recovery: A Framework and Simulation Model," by S.B. Miles and S.E. Chang, 7/25/03, (PB2004-104388, A07, CD-A07).

MCEER-03-0006 "Behavior of Underground Piping Joints Due to Static and Dynamic Loading," by R.D. Meis, M. Maragakis and R. Siddharthan, 11/17/03, (PB2005-102194, A13, MF-A03, CD-A00).

MCEER-04-0001 "Experimental Study of Seismic Isolation Systems with Emphasis on Secondary System Response and Verification of Accuracy of Dynamic Response History Analysis Methods," by E. Wolff and M. Constantinou, 1/16/04 (PB2005-102195, A99, MF-E08, CD-A00).

MCEER-04-0002 "Tension, Compression and Cyclic Testing of Engineered Cementitious Composite Materials," by K. Kesner and S.L. Billington, 3/1/04, (PB2005-102196, A08, CD-A08).

MCEER-04-0003 "Cyclic Testing of Braces Laterally Restrained by Steel Studs to Enhance Performance During Earthquakes," by O.C. Celik, J.W. Berman and M. Bruneau, 3/16/04, (PB2005-102197, A13, MF-A03, CD-A00).

MCEER-04-0004 "Methodologies for Post Earthquake Building Damage Detection Using SAR and Optical Remote Sensing: Application to the August 17, 1999 Marmara, Turkey Earthquake," by C.K. Huyck, B.J. Adams, S. Cho, R.T. Eguchi, B. Mansouri and B. Houshmand, 6/15/04, (PB2005-104888, A10, CD-A00).

MCEER-04-0005 "Nonlinear Structural Analysis Towards Collapse Simulation: A Dynamical Systems Approach," by M.V. Sivaselvan and A.M. Reinhorn, 6/16/04, (PB2005-104889, A11, MF-A03, CD-A00).

MCEER-04-0006 "Proceedings of the Second PRC-US Workshop on Seismic Analysis and Design of Special Bridges," edited by G.C. Lee and L.C. Fan, 6/25/04, (PB2005-104890, A16, CD-A00).

MCEER-04-0007 "Seismic Vulnerability Evaluation of Axially Loaded Steel Built-up Laced Members," by K. Lee and M. Bruneau, 6/30/04, (PB2005-104891, A16, CD-A00).

MCEER-04-0008 "Evaluation of Accuracy of Simplified Methods of Analysis and Design of Buildings with Damping Systems for Near-Fault and for Soft-Soil Seismic Motions," by E.A. Pavlou and M.C. Constantinou, 8/16/04, (PB2005-104892, A08, MF-A02, CD-A00).

MCEER-04-0009 "Assessment of Geotechnical Issues in Acute Care Facilities in California," by M. Lew, T.D. O'Rourke, R. Dobry and M. Koch, 9/15/04, (PB2005-104893, A08, CD-A00).

MCEER-04-0010 "Scissor-Jack-Damper Energy Dissipation System," by A.N. Sigaher-Boyle and M.C. Constantinou, 12/1/04 (PB2005-108221).

MCEER-04-0011 "Seismic Retrofit of Bridge Steel Truss Piers Using a Controlled Rocking Approach," by M. Pollino and M. Bruneau, 12/20/04 (PB2006-105795).

MCEER-05-0001 "Experimental and Analytical Studies of Structures Seismically Isolated with an Uplift-Restraint Isolation System," by P.C. Roussis and M.C. Constantinou, 1/10/05 (PB2005-108222).

MCEER-05-0002 "A Versatile Experimentation Model for Study of Structures Near Collapse Applied to Seismic Evaluation of Irregular Structures," by D. Kusumastuti, A.M. Reinhorn and A. Rutenberg, 3/31/05 (PB2006-101523).

MCEER-05-0003 "Proceedings of the Third PRC-US Workshop on Seismic Analysis and Design of Special Bridges," edited by L.C. Fan and G.C. Lee, 4/20/05, (PB2006-105796).

MCEER-05-0004 "Approaches for the Seismic Retrofit of Braced Steel Bridge Piers and Proof-of-Concept Testing of an Eccentrically Braced Frame with Tubular Link," by J.W. Berman and M. Bruneau, 4/21/05 (PB2006-101524).

MCEER-05-0005 "Simulation of Strong Ground Motions for Seismic Fragility Evaluation of Nonstructural Components in Hospitals," by A. Wanitkorkul and A. Filiatrault, 5/26/05 (PB2006-500027).

MCEER-05-0006 "Seismic Safety in California Hospitals: Assessing an Attempt to Accelerate the Replacement or Seismic Retrofit of Older Hospital Facilities," by D.J. Alesch, L.A. Arendt and W.J. Petak, 6/6/05 (PB2006-105794).

MCEER-05-0007 "Development of Seismic Strengthening and Retrofit Strategies for Critical Facilities Using Engineered Cementitious Composite Materials," by K. Kesner and S.L. Billington, 8/29/05 (PB2006-111701).

MCEER-05-0008 "Experimental and Analytical Studies of Base Isolation Systems for Seismic Protection of Power Transformers," by N. Murota, M.Q. Feng and G-Y. Liu, 9/30/05 (PB2006-111702).

MCEER-05-0009 "3D-BASIS-ME-MB: Computer Program for Nonlinear Dynamic Analysis of Seismically Isolated Structures," by P.C. Tsopelas, P.C. Roussis, M.C. Constantinou, R. Buchanan and A.M. Reinhorn, 10/3/05 (PB2006-111703).

MCEER-05-0010 "Steel Plate Shear Walls for Seismic Design and Retrofit of Building Structures," by D. Vian and M. Bruneau, 12/15/05 (PB2006-111704).

MCEER-05-0011 "The Performance-Based Design Paradigm," by M.J. Astrella and A. Whittaker, 12/15/05 (PB2006-111705).

MCEER-06-0001 "Seismic Fragility of Suspended Ceiling Systems," H. Badillo-Almaraz, A.S. Whittaker, A.M. Reinhorn and G.P. Cimellaro, 2/4/06 (PB2006-111706).

MCEER-06-0002 "Multi-Dimensional Fragility of Structures," by G.P. Cimellaro, A.M. Reinhorn and M. Bruneau, 3/1/06 (PB2007-106974, A09, MF-A02, CD A00).

MCEER-06-0003 "Built-Up Shear Links as Energy Dissipators for Seismic Protection of Bridges," by P. Dusicka, A.M. Itani and I.G. Buckle, 3/15/06 (PB2006-111708).

MCEER-06-0004 "Analytical Investigation of the Structural Fuse Concept," by R.E. Vargas and M. Bruneau, 3/16/06 (PB2006-111709).

MCEER-06-0005 "Experimental Investigation of the Structural Fuse Concept," by R.E. Vargas and M. Bruneau, 3/17/06 (PB2006-111710).

MCEER-06-0006 "Further Development of Tubular Eccentrically Braced Frame Links for the Seismic Retrofit of Braced Steel Truss Bridge Piers," by J.W. Berman and M. Bruneau, 3/27/06 (PB2007-105147).

MCEER-06-0007 "REDARS Validation Report," by S. Cho, C.K. Huyck, S. Ghosh and R.T. Eguchi, 8/8/06 (PB2007-106983).

MCEER-06-0008 "Review of Current NDE Technologies for Post-Earthquake Assessment of Retrofitted Bridge Columns," by J.W. Song, Z. Liang and G.C. Lee, 8/21/06 (PB2007-106984).

MCEER-06-0009 "Liquefaction Remediation in Silty Soils Using Dynamic Compaction and Stone Columns," by S. Thevanayagam, G.R. Martin, R. Nashed, T. Shenthan, T. Kanagalingam and N. Ecemis, 8/28/06 (PB2007-106985).

MCEER-06-0010 "Conceptual Design and Experimental Investigation of Polymer Matrix Composite Infill Panels for Seismic Retrofitting," by W. Jung, M. Chiewanichakorn and A.J. Aref, 9/21/06 (PB2007-106986).

MCEER-06-0011 "A Study of the Coupled Horizontal-Vertical Behavior of Elastomeric and Lead-Rubber Seismic Isolation Bearings," by G.P. Warn and A.S. Whittaker, 9/22/06 (PB2007-108679).

MCEER-06-0012 "Proceedings of the Fourth PRC-US Workshop on Seismic Analysis and Design of Special Bridges: Advancing Bridge Technologies in Research, Design, Construction and Preservation," Edited by L.C. Fan, G.C. Lee and L. Ziang, 10/12/06 (PB2007-109042).

MCEER-06-0013 "Cyclic Response and Low Cycle Fatigue Characteristics of Plate Steels," by P. Dusicka, A.M. Itani and I.G. Buckle, 11/1/06 06 (PB2007-106987).

MCEER-06-0014 "Proceedings of the Second US-Taiwan Bridge Engineering Workshop," edited by W.P. Yen, J. Shen, J-Y. Chen and M. Wang, 11/15/06 (PB2008-500041).

MCEER-06-0015 "User Manual and Technical Documentation for the REDARS™ Import Wizard," by S. Cho, S. Ghosh, C.K. Huyck and S.D. Werner, 11/30/06 (PB2007-114766).

MCEER-06-0016 "Hazard Mitigation Strategy and Monitoring Technologies for Urban and Infrastructure Public Buildings: Proceedings of the China-US Workshops," edited by X.Y. Zhou, A.L. Zhang, G.C. Lee and M. Tong, 12/12/06 (PB2008-500018).

MCEER-07-0001 "Static and Kinetic Coefficients of Friction for Rigid Blocks," by C. Kafali, S. Fathali, M. Grigoriu and A.S. Whittaker, 3/20/07 (PB2007-114767).

MCEER-07-0002 "Hazard Mitigation Investment Decision Making: Organizational Response to Legislative Mandate," by L.A. Arendt, D.J. Alesch and W.J. Petak, 4/9/07 (PB2007-114768).

MCEER-07-0003 "Seismic Behavior of Bidirectional-Resistant Ductile End Diaphragms with Unbonded Braces in Straight or Skewed Steel Bridges," by O. Celik and M. Bruneau, 4/11/07 (PB2008-105141).

MCEER-07-0004   "Modeling Pile Behavior in Large Pile Groups Under Lateral Loading," by A.M. Dodds and G.R. Martin, 4/16/07(PB2008-105142).

MCEER-07-0005   "Experimental Investigation of Blast Performance of Seismically Resistant Concrete-Filled Steel Tube Bridge Piers," by S. Fujikura, M. Bruneau and D. Lopez-Garcia, 4/20/07 (PB2008-105143).

MCEER-07-0006   "Seismic Analysis of Conventional and Isolated Liquefied Natural Gas Tanks Using Mechanical Analogs," by I.P. Christovasilis and A.S. Whittaker, 5/1/07.

MCEER-07-0007   "Experimental Seismic Performance Evaluation of Isolation/Restraint Systems for Mechanical Equipment – Part 1: Heavy Equipment Study," by S. Fathali and A. Filiatrault, 6/6/07 (PB2008-105144).

MCEER-07-0008   "Seismic Vulnerability of Timber Bridges and Timber Substructures," by A.A. Sharma, J.B. Mander, I.M. Friedland and D.R. Allicock, 6/7/07 (PB2008-105145).

MCEER-07-0009   "Experimental and Analytical Study of the XY-Friction Pendulum (XY-FP) Bearing for Bridge Applications," by C.C. Marin-Artieda, A.S. Whittaker and M.C. Constantinou, 6/7/07 (PB2008-105191).

MCEER-07-0010   "Proceedings of the PRC-US Earthquake Engineering Forum for Young Researchers," Edited by G.C. Lee and X.Z. Qi, 6/8/07.

MCEER-07-0011   "Design Recommendations for Perforated Steel Plate Shear Walls," by R. Purba and M. Bruneau, 6/18/07, (PB2008-105192).

MCEER-07-0012   "Performance of Seismic Isolation Hardware Under Service and Seismic Loading," by M.C. Constantinou, A.S. Whittaker, Y. Kalpakidis, D.M. Fenz and G.P. Warn, 8/27/07, (PB2008-105193).

MCEER-07-0013   "Experimental Evaluation of the Seismic Performance of Hospital Piping Subassemblies," by E.R. Goodwin, E. Maragakis and A.M. Itani, 9/4/07, (PB2008-105194).

MCEER-07-0014   "A Simulation Model of Urban Disaster Recovery and Resilience: Implementation for the 1994 Northridge Earthquake," by S. Miles and S.E. Chang, 9/7/07, (PB2008-106426).

MCEER-07-0015   "Statistical and Mechanistic Fragility Analysis of Concrete Bridges," by M. Shinozuka, S. Banerjee and S-H. Kim, 9/10/07, (PB2008-106427).

MCEER-07-0016   "Three-Dimensional Modeling of Inelastic Buckling in Frame Structures," by M. Schachter and AM. Reinhorn, 9/13/07, (PB2008-108125).

MCEER-07-0017   "Modeling of Seismic Wave Scattering on Pile Groups and Caissons," by I. Po Lam, H. Law and C.T. Yang, 9/17/07 (PB2008-108150).

MCEER-07-0018   "Bridge Foundations: Modeling Large Pile Groups and Caissons for Seismic Design," by I. Po Lam, H. Law and G.R. Martin (Coordinating Author), 12/1/07 (PB2008-111190).

MCEER-07-0019   "Principles and Performance of Roller Seismic Isolation Bearings for Highway Bridges," by G.C. Lee, Y.C. Ou, Z. Liang, T.C. Niu and J. Song, 12/10/07.

MCEER-07-0020   "Centrifuge Modeling of Permeability and Pinning Reinforcement Effects on Pile Response to Lateral Spreading," by L.L Gonzalez-Lagos, T. Abdoun and R. Dobry, 12/10/07 (PB2008-111191).

MCEER-07-0021   "Damage to the Highway System from the Pisco, Perú Earthquake of August 15, 2007," by J.S. O'Connor, L. Mesa and M. Nykamp, 12/10/07, (PB2008-108126).

MCEER-07-0022   "Experimental Seismic Performance Evaluation of Isolation/Restraint Systems for Mechanical Equipment – Part 2: Light Equipment Study," by S. Fathali and A. Filiatrault, 12/13/07 (PB2008-111192).

MCEER-07-0023   "Fragility Considerations in Highway Bridge Design," by M. Shinozuka, S. Banerjee and S.H. Kim, 12/14/07 (PB2008-111193).

MCEER-07-0024   "Performance Estimates for Seismically Isolated Bridges," by G.P. Warn and A.S. Whittaker, 12/30/07 (PB2008-112230).

MCEER-08-0001   "Seismic Performance of Steel Girder Bridge Superstructures with Conventional Cross Frames," by L.P. Carden, A.M. Itani and I.G. Buckle, 1/7/08, (PB2008-112231).

MCEER-08-0002   "Seismic Performance of Steel Girder Bridge Superstructures with Ductile End Cross Frames with Seismic Isolators," by L.P. Carden, A.M. Itani and I.G. Buckle, 1/7/08 (PB2008-112232).

MCEER-08-0003   "Analytical and Experimental Investigation of a Controlled Rocking Approach for Seismic Protection of Bridge Steel Truss Piers," by M. Pollino and M. Bruneau, 1/21/08 (PB2008-112233).

MCEER-08-0004   "Linking Lifeline Infrastructure Performance and Community Disaster Resilience: Models and Multi-Stakeholder Processes," by S.E. Chang, C. Pasion, K. Tatebe and R. Ahmad, 3/3/08 (PB2008-112234).

MCEER-08-0005   "Modal Analysis of Generally Damped Linear Structures Subjected to Seismic Excitations," by J. Song, Y-L. Chu, Z. Liang and G.C. Lee, 3/4/08 (PB2009-102311).

MCEER-08-0006   "System Performance Under Multi-Hazard Environments," by C. Kafali and M. Grigoriu, 3/4/08 (PB2008-112235).

MCEER-08-0007   "Mechanical Behavior of Multi-Spherical Sliding Bearings," by D.M. Fenz and M.C. Constantinou, 3/6/08 (PB2008-112236).

MCEER-08-0008   "Post-Earthquake Restoration of the Los Angeles Water Supply System," by T.H.P. Tabucchi and R.A. Davidson, 3/7/08 (PB2008-112237).

MCEER-08-0009   "Fragility Analysis of Water Supply Systems," by A. Jacobson and M. Grigoriu, 3/10/08 (PB2009-105545).

MCEER-08-0010   "Experimental Investigation of Full-Scale Two-Story Steel Plate Shear Walls with Reduced Beam Section Connections," by B. Qu, M. Bruneau, C-H. Lin and K-C. Tsai, 3/17/08.

MCEER-08-0011   "Seismic Evaluation and Rehabilitation of Critical Components of Electrical Power Systems," S. Ersoy, B. Feizi, A. Ashrafi and M. Ala Saadeghvaziri, 3/17/08 (PB2009-105546).

MCEER-08-0012   "Seismic Behavior and Design of Boundary Frame Members of Steel Plate Shear Walls," by B. Qu and M. Bruneau, 4/26/08.

MCEER-08-0013   "Development and Appraisal of a Numerical Cyclic Loading Protocol for Quantifying Building System Performance," by A. Filiatrault, A. Wanitkorkul and M. Constantinou, 4/27/08.

MCEER-08-0014   "Structural and Nonstructural Earthquake Design: The Challenge of Integrating Specialty Areas in Designing Complex, Critical Facilities," by W.J. Petak and D.J. Alesch, 4/30/08.

MCEER-08-0015   "Seismic Performance Evaluation of Water Systems," by Y. Wang and T.D. O'Rourke, 5/5/08.

MCEER-08-0016   "Seismic Response Modeling of Water Supply Systems," by P. Shi and T.D. O'Rourke, 5/5/08.

MCEER-08-0017   "Numerical and Experimental Studies of Self-Centering Post-Tensioned Steel Frames," by D. Wang and A. Filiatrault, 5/12/08.

MCEER-08-0018   "Development, Implementation and Verification of Dynamic Analysis Models for Multi-Spherical Sliding Bearings," by D.M. Fenz and M.C. Constantinou, 8/15/08.

MCEER-08-0019   "Performance Assessment of Conventional and Base Isolated Nuclear Power Plants for Earthquake Blast Loadings," by Y.N. Huang, A.S. Whittaker and N. Luco, 10/28/08.

MCEER-08-0020   "Remote Sensing for Resilient Multi-Hazard Disaster Response – Volume I: Introduction to Damage Assessment Methodologies," by B.J. Adams and R.T. Eguchi, 11/17/08.

MCEER-08-0021   "Remote Sensing for Resilient Multi-Hazard Disaster Response – Volume II: Counting the Number of Collapsed Buildings Using an Object-Oriented Analysis: Case Study of the 2003 Bam Earthquake," by L. Gusella, C.K. Huyck and B.J. Adams, 11/17/08.

MCEER-08-0022   "Remote Sensing for Resilient Multi-Hazard Disaster Response – Volume III: Multi-Sensor Image Fusion Techniques for Robust Neighborhood-Scale Urban Damage Assessment," by B.J. Adams and A. McMillan, 11/17/08.

MCEER-08-0023   "Remote Sensing for Resilient Multi-Hazard Disaster Response – Volume IV: A Study of Multi-Temporal and Multi-Resolution SAR Imagery for Post-Katrina Flood Monitoring in New Orleans," by A. McMillan, J.G. Morley, B.J. Adams and S. Chesworth, 11/17/08.

MCEER-08-0024   "Remote Sensing for Resilient Multi-Hazard Disaster Response – Volume V: Integration of Remote Sensing Imagery and VIEWS^{TM} Field Data for Post-Hurricane Charley Building Damage Assessment," by J.A. Womble, K. Mehta and B.J. Adams, 11/17/08.

MCEER-08-0025   "Building Inventory Compilation for Disaster Management: Application of Remote Sensing and Statistical Modeling," by P. Sarabandi, A.S. Kiremidjian, R.T. Eguchi and B. J. Adams, 11/20/08.